Impact of Dynamical Fermions on QCD Centre Vortices

THE UNIVERSITY of ADELAIDE

James Biddle

Supervisors:

Dr. Waseem Kamleh and Prof. Derek B. Leinweber

Department of Physics

University of Adelaide

This dissertation is submitted for the degree of

Doctor of Philosophy

July 2023

Table of contents

To Kate

Declaration

I certify that this work contains no material which has been accepted for the award of any other degree or diploma in my name, in any university or other tertiary institution and, to the best of my knowledge and belief, contains no material previously published or written by another person, except where due reference has been made in the text. In addition, I certify that no part of this work will, in the future, be used in a submission in my name, for any other degree or diploma in any university or other tertiary institution without the prior approval of the University of Adelaide and where applicable, any partner institution responsible for the joint award of this degree.

I give permission for the digital version of my thesis to be made available on the web, via the University's digital research repository, the Library Search and also through web search engines, unless permission has been granted by the University to restrict access for a period of time.

I acknowledge the support I have received for my research through the provision of an Australian Government Research Training Program Scholarship.

James Biddle
July 2023

Acknowledgements

This thesis is the culmination of many years of work, with many people playing both large and small roles over the course of this journey. The largest role was of course played by my supervisors, Derek and Waseem, whose knowledge, experience, and drafts that dripped red ink have been essential to the success of this research. I cannot thank you enough for all of your support.

My fellow students have been not just an important part of my research, but also of my life over the last 6 years of postgraduate study. Debates, discussions, questions and queries have been par for the course, and have made postgraduate life a rich and vibrant experience.

My family have been a wonderful source of support, with special thanks going to my Mum and Dad for always believing in me and encouraging me to push forward regardless of setbacks. My friends have also been invaluable, both for the encouragement and the great times we've had together over the years. Finally, I thank my amazing partner Kate. I couldn't have done this without you.

Abstract

The origin of quark confinement from the theory of Quantum Chromodynamics (QCD) is a subject of great interest. The centre vortex model has been proposed as a possible explanation for this property, with remarkable success having been demonstrated over the past 40 years. In this work, we push this model in two new directions. The first is an exploration of the geometric structure of centre vortices as they appear in lattice simulations. This allows for a detailed examination of the correlation between centre vortices and topological charge, as well as an exploration of vortex branching and percolation in QCD.

The second direction explored is the transition from pure-gauge theory to full QCD, where gluons transition to dynamical quark-antiquark pairs. The effect of the introduction of dynamical quarks is explored in the context of the static quark potential, gluon propagator and Euclidean correlator. These calculations reveal the remarkable impact of dynamical fermions on the structure of centre vortices, and for the first time finds quantitative agreement between the vortex-only and original gauge fields. These results reveal the important connection between dynamical fermions and centre vortices, further reinforcing the crucial role centre vortices play in generating confinement in QCD.

List of figures

List of tables

Chapter 1

Introduction

Of the four forces of nature, it is the strong force that poses some of the most challenging problems present in modern physics. Despite the development of the theory of quantum chromodynamics (QCD), a full understanding of the emergent properties of the strong force that governs the behaviour of quarks and gluons remains elusive. This is primarily a result of the mathematical intractability of the theory. This arises from the complex self-interactions of gluons resulting in highly non-trivial vacuum structure. This same vacuum structure also gives rise to two of the defining features of QCD: the confinement of quarks and gluons and the dynamical generation of mass.

Confinement is expressed experimentally by the inability to observe quarks in isolation. Instead, quarks are always bound together into hadrons; composite particles that carry net-zero *colour*, the QCD equivalent of electric charge. Dynamical generation of mass results in the mass of these hadrons being greater than the sum of their elementary constituents. A famous consequence of this property is the fact that the sum of the bare masses of the three quarks comprising a proton can only account for approximately 1% of the observed mass of the proton [1]. These two properties are fundamental to the behaviour of quarks and gluons, however their origin within the theoretical understanding of QCD remains an open question to this day.

The most successful theoretical technique used to probe the nature of QCD is known as the *lattice*. Lattice QCD attempts to resolve the mathematical difficulties of QCD by considering a region of spacetime in terms of a discrete grid of points. The lattice provides a nonperturbative regulator for the theory, introducing a maximum momentum governed by the spacing of the lattice. By reducing computations to a finite number of points in a periodic volume, it is possible to gain tangible insight into

the behaviour of QCD. This of course comes at the cost of the introduction of lattice artifacts arising from this discretisation, but one of the most important properties of the lattice QCD method is that it can be systematically improved to reduce the impact of these systematic errors. Thus, it provides the only known first-principles systematically-improvable approach to performing QCD calculations.

With the advent of modern supercomputers, lattice QCD has provided a wealth of insight into the dynamics of QCD. It has also enabled researchers to explore a wide variety of theories that seek to explain the properties of confinement and dynamical generation of mass. One of the most promising theories is known as the *centre vortex* model [2–12]. Centre vortices are remarkably simple structures that can be identified within the ground-state gluon fields. Despite their simplicity, centre vortices are able to reproduce a wide range of properties consistent with both confinement and the dynamical generation of mass [13–20]. Furthermore, removal of centre vortices has shown a corresponding loss of these properties. As such, there is much interest in further elucidating the impact of centre vortices on QCD.

Expanding upon this body of work forms the motivation for this research. In particular, no previous work has explored the impact of dynamical fermions on the centre vortex structure of QCD. Inclusion of dynamical fermions allows us to observe how centre vortices behave in the presence of these new physical degrees of freedom, and provides new insight into the fascinating interplay between QCD and centre vortices. These effects will be studied herein by performing calculations of the static quark potential, gluon propagator and Euclidean correlator, each of which can be used to observe indicators of confinement.

Building on these results, we also employ novel visualisation techniques to explore the geometry of centre vortices. These techniques allow us to search for correlations between centre vortices and other topological objects present in the QCD vacuum. They allow us to quantitatively examine changes in vortex structure induced by the introduction of dynamical fermions. Such explorations have never been done in the QCD gauge group of $SU(3)$, which permits additional complexity in the centre vortex structure. This analysis reveals for the first time the significance of structures known as vortex branching points. These methods provide valuable insight into determining the geometric response of centre vortices to the inclusion of dynamical fermions, and the relationship between this geometry and the presence of confinement. The consequence of this body of research is a greater understanding of the complex interrelationship between QCD ground-state fields, dynamical fermions, and centre vortices.

This thesis is structured as follows: Chapter 2 will introduce the theory of QCD in more detail and outline how calculations are conducted on the lattice. Chapter 3 will introduce the centre vortex model and how centre vortices are identified on the lattice. Chapter 4 reports the results published in Ref. [21], outlining the understanding of the centre-vortex picture in pure Yang-Mills QCD. This chapter also introduces the visualisation techniques that allow for a detailed understanding of the pure-gauge vortex structure. Chapter 5 reports the results published in Ref. [22], beginning the exploration of the impact of dynamical fermions with the calculation of the static quark potential on vortex-modified ensembles. Chapter 6 reports the results published in Ref. [23] and continues the exploration of the impact of dynamical fermions by presenting calculations of the gluon propagator and Euclidean correlator. Chapter 7 reports the results published in Ref. [24], returning to the visualisation techniques of Chapter 4 to observe how vortex structure changes upon the introduction of dynamical fermions. Chapter 8 summarises the findings of this research.

Chapter 2

Lattice QCD

Quantum chromodynamics, like all theories encompassed by the Standard Model, is a gauge field theory, wherein the fermion degrees of freedom transform under the fundamental representation of the group and the force-carrying gauge boson transforms under the adjoint representation. The gauge group of QCD is the non-Abelian group $SU(3)$. The non-Abelian nature gives rise to many of the unique complexities associated with QCD and leads to the necessity for lattice QCD to be able to calculate quantities of interest. In this chapter, we discuss the formulation of continuum QCD, then transition to the lattice. We will also highlight the differences between so-called pure-gauge lattice calculations and those involving dynamical fermions, as comparisons between these two types of lattice calculations will recur throughout this thesis.

2.1 Continuum QCD

Like all gauge field theories, QCD is formulated via a Lagrangian that describes the interactions between a fermion field and a corresponding gauge field. In the case of QCD, the fermion field describes the quarks, and the gauge field describes the gluons. The symmetry group of the Lagrangian is $SU(3)$, which in the fundamental representation is the group of 3×3 unitary matrices with unit determinant. The QCD Lagrangian density is

$$\mathcal{L}(x) = \bar{\psi}(x) \left(i\not{D} - m \right) \psi(x) - \frac{1}{2} \operatorname{Tr} \left(F_{\mu\nu}(x) \, F^{\mu\nu}(x) \right) . \tag{2.1}$$

It is worth expanding upon the implications of each term in the Lagrangian. $\psi(x)$ is the quark field triplet in colour space, with $\bar{\psi}$ the corresponding antiquark field. $\not{D}$ is the covariant derivative

$$\gamma^\mu D_\mu = \gamma^\mu \left(\partial_\mu + igA_\mu\right) , \tag{2.2}$$

with A_μ being the gluon field, γ^μ the gamma matrices, and g the gauge coupling. We adopt the Dirac gamma matrix convention described in Appendix A.1. Hence, the first term of Eq. (2.1) gives rise to quark-gluon interactions. The second term in Eq. (2.1) describes gluon-gluon interactions through the field strength tensor

$$F_{\mu\nu} = \partial_\mu A_\nu - \partial_\nu A_\mu + ig\left[A_\mu,\, A_\nu\right] . \tag{2.3}$$

It is the 3-point and 4-point gluon interactions arising from the last term in Eq. (2.3) that are responsible for the highly nontrivial QCD ground-state fields, as gluons are permitted to not only interact with quarks but also with themselves.

These two terms of the Lagrangian are referred to as the fermionic ($\mathcal{L}_F$) and gluonic ($\mathcal{L}_G$) terms respectively, such that

$$\mathcal{L}_F(x) = \bar{\psi}(x)\left(i\not{D} - m\right)\psi(x) \tag{2.4}$$

$$\mathcal{L}_G(x) = -\frac{1}{2}\,\mathrm{Tr}\left(F_{\mu\nu}(x)\,F^{\mu\nu}(x)\right) \tag{2.5}$$

Under a local gauge transformation, $\Omega(x)$, the QCD fields transform like

$$\psi(x) \to \Omega(x)\,\psi(x)\,, \tag{2.6}$$

$$\bar{\psi}(x) \to \bar{\psi}(x)\,\Omega^\dagger(x)\,, \tag{2.7}$$

$$A_\mu(x) \to \Omega(x)\,A_\mu(x)\,\Omega^\dagger + \frac{i}{g}\left(\partial_\mu\Omega(x)\right)\,\Omega^\dagger(x)\,. \tag{2.8}$$

The result of these transformation properties is that the QCD Lagrangian is locally gauge invariant.

The action corresponding to the Lagrangian is obtained by integrating over all spacetime, such that

$$\mathcal{S} = \int d^4x\,\mathcal{L}(x) \tag{2.9}$$

The gluon and fermion actions, $\mathcal{S}_G$ and $\mathcal{S}_F$, are obtained by integrating the corresponding components of the Lagrangian. Expectation values of operators are calculated via

path-integral expressions of the form

$$\left\langle O[\psi,\, \bar{\psi},\, A_\mu] \right\rangle = \frac{1}{\mathcal{Z}} \int \mathcal{D}[\psi,\, \bar{\psi}]\, \mathcal{D}[A_\mu]\, O[\psi,\, \bar{\psi},\, A_\mu]\, e^{i\, \mathcal{S}[\psi,\, \bar{\psi},\, A_\mu]}\,, \tag{2.10}$$

where Z is the generating functional

$$\mathcal{Z} = \int \mathcal{D}[\psi,\, \bar{\psi}]\, \mathcal{D}[A_\mu]\, e^{i\, \mathcal{S}[\psi,\, \bar{\psi},\, A_\mu]}\,. \tag{2.11}$$

It is the goal of QCD to evaluate expressions of the form given in Eq. (2.10). In practice, this is impossible to perform analytically at low energies. Thus it is essential to seek an alternative approach.

There are a number of interesting properties that can be observed in Eq. (2.10). First is the close similarity that this expression bears to the evaluation of expectation values in statistical mechanics. In statistical mechanics, the partition function acts as a probability normalisation, whilst a term like $e^{-\beta\, H}$ weights each state. A crucial difference is the presence of the factor of i in the exponential, which defies interpretation as a probability weight. To account for this, it is possible to formulate the theory in Euclidean space via

$$t \to -it\,, \qquad A^0 \to iA^0\,. \tag{2.12}$$

This has the effect of taking

$$i\mathcal{S} \to -\mathcal{S}\,, \tag{2.13}$$

which results in operator expectation values taking the form

$$\left\langle O[\psi,\, \bar{\psi},\, A_\mu] \right\rangle = \frac{1}{\mathcal{Z}} \int \mathcal{D}[\psi,\, \bar{\psi}]\, \mathcal{D}[A_\mu]\, O[\psi,\, \bar{\psi},\, A_\mu]\, e^{-\,\mathcal{S}[\psi,\, \bar{\psi},\, A_\mu]}\,. \tag{2.14}$$

Eq. (2.14) motivates lattice QCD. To evaluate an operator, one needs to integrate over all possible quark, antiquark and gluon fields, with each field weighted by $\exp(-\mathcal{S})$. In general, this integral remains impossible to compute exactly. However, it highlights the fact that if one can effectively sample the relevant QCD fields according to the probability distribution given by the action, then it would be possible to estimate the operator expectation values. This is precisely the aim of lattice QCD.

2.2 Lattice QCD

Lattice QCD seeks to calculate operators of the form presented in Eq. (2.14) by discretising spacetime into a hypercubic grid. This is done by considering a finite set of points in each of the three spatial and one temporal directions, with the spacing between each point denoted as the lattice spacing, a. This results in a total lattice volume of $V = (N_s\, a)^3 \times N_t\, a$, where N_s and N_t are the number of points in the spatial and temporal directions respectively. For the purposes of this work, periodic boundary conditions are also imposed upon the lattice.

We will now discuss the formulation of gluon and fermion fields on the lattice. An immediate effect of discretisation is that derivatives and integrals now become finite differences and sums, such that for a test function $f(x)$, we have

$$\partial_\mu f(x) \to \frac{f(x+\hat{\mu}) - f(x-\hat{\mu})}{2a}, \tag{2.15}$$

$$\int d^4x\, f(x) \to a^4 \sum_{x\in\Lambda} f(x)\,, \tag{2.16}$$

where Λ simply refers to the set of all points in the lattice, and $\hat{\mu}$ is the unit vector in the μ direction multiplied by the lattice spacing. For example, $\mathcal{S}_F$ in the absence of gauge fields would, under this prescription, read

$$\mathcal{S}_F = a^4 \sum_{x\in\Lambda} \bar{\psi}(x) \left(\sum_{\mu=1}^{4} \gamma_\mu \frac{\psi(x+\hat{\mu}) - \psi(x-\hat{\mu})}{2a} + m\psi(x) \right). \tag{2.17}$$

However, reintroducing the gauge fields requires some care. The expression in Eq. (2.17) is not gauge invariant, and in fact each term now has reference to points separated by a finite distance. An important part of local gauge invariance is that the gauge fields account for the change in the underlying gauge of the fermion fields over infinitesimal separations. This situation changes on the lattice, as we now want to account for the change in gauge over finite separations. To do this, the gauge fields are reintroduced in the form of gauge links, $U_\mu(x)$.

The gauge links are introduced to resolve the fact that terms such as $\bar{\psi}(x)\,\psi(x+\hat{\mu})$ present in Eq. (2.17) are not gauge invariant under transformations of the form presented in Eqs. (2.6) and (2.7). The gauge links $U_\mu(x)$ have the transformation property,

$$U_\mu(x) \to \Omega(x)\, U_\mu(x)\, \Omega(x+\hat{\mu}) \tag{2.18}$$

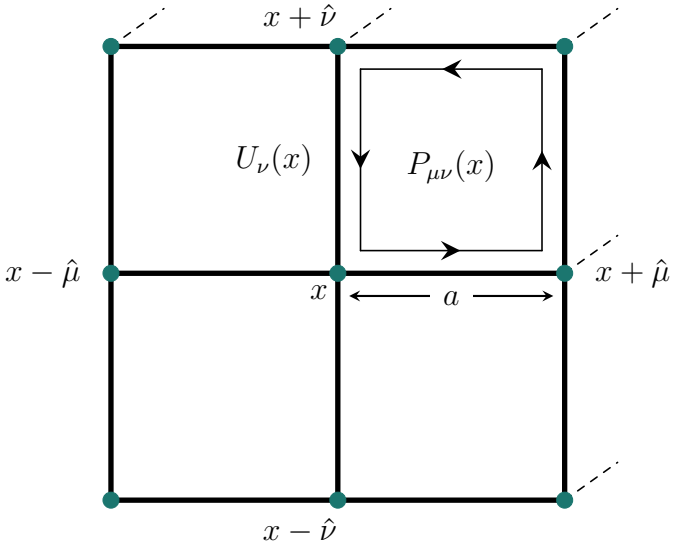

Fig. 2.1 An example of a 2D lattice with lattice spacing a. From site x we define $x + a\hat{\mu}$ to refer to the next lattice site in the $\hat{\mu}$ direction. The gauge links $U_\mu(x)$ are defined on the links between sites. The plaquette $P_{\mu\nu}(x)$ is the product of the four gauge links around a 1×1 loop.

Given this transformation property, it is easy to see why $U_\mu(x)$ are referred to as links. They exist as a link between the lattice sites x and $x + \hat{\mu}$. Indeed, on the lattice they are typically visualised as connections between neighbouring sites, as seen in Fig. 2.1. The gauge links are connected to the continuum gluon fields by the expression,

$$U_\mu(x) = \mathcal{P} \exp\left(-iag \int_0^1 d\lambda \, A_\mu(x + \lambda\hat{\mu})\right) , \tag{2.19}$$

where $\mathcal{P}$ denotes a path-ordered integral. This is often approximated on the lattice by using a midpoint estimation of the integral in Eq. (2.19) such that,

$$U_\mu(x) = \exp\left(-iagA_\mu\left(x + \frac{\hat{\mu}}{2}\right)\right) . \tag{2.20}$$

Based on Eq. (2.19), we note that we can also express the reverse link from $x + \hat{\mu}$ to x as $U_\mu^\dagger(x)$. The introduction of the gauge links allows us to write a gauge-invariant $\mathcal{S}_F$ as,

$$\mathcal{S}_F = a^4 \sum_{x\in\Lambda} \bar{\psi}(x) \left(\sum_{\mu=1}^{4} \gamma_\mu \frac{U_\mu(x)\,\psi(x+\hat{\mu}) - U_\mu(x-\hat{\mu})^\dagger\,\psi(x-\hat{\mu})}{2a} + m\psi(x)\right) . \tag{2.21}$$

Eq. (2.21) can also be rewritten as a matrix expression

$$\mathcal{S}_F = a^4 \sum_{x,y} \bar{\psi}(x)\, D(x|y)\, \psi(y)\,, \tag{2.22}$$

where $D(x|y)$ is known as the position-space Dirac operator,

$$D(x|y) = \sum_{\mu=1}^{4} \gamma_\mu \frac{U_\mu(x)\,\delta_{x+\hat{\mu},y} - U_\mu^\dagger(x-\hat{\mu})\,\delta_{x-\hat{\mu},y}}{2a} + m\,\delta_{x,y}\,. \tag{2.23}$$

The inverse of the Dirac operator, $D^{-1}(x|y)$, is the quark propagator and is also essential for the calculation of lattice n-point functions.

The form of the Dirac operator given in Eq. (2.23) appears at first glance to be a sufficient discretisation of the continuum fermion action. However, there is an unintentional consequence of this discretisation process that is best revealed by taking the Dirac operator to momentum space. After a Fourier transform, the momentum-space Dirac operator is given by,

$$\widetilde{D}(p) = m + \frac{i}{a}\sum_{\mu} \gamma_\mu \sin(p_\mu a)\,. \tag{2.24}$$

The problem arises when one considers massless fermions by setting $m = 0$. In this case, we find that the the inverse Dirac operator in momentum space yields,

$$\widetilde{D}^{-1}(p) = \frac{-ia^{-1}\sum_\mu \gamma_\mu \sin(p_\mu\, a)}{a^{-2}\sum_\mu \sin^2(p_\mu\, a)}\,. \tag{2.25}$$

The continuum form of Eq. (2.25) has a single pole at $p^2 = 0$, indicating the presence of a single massless fermion. However, noting that $p_\mu \in \left(\frac{-\pi}{a}, \frac{\pi}{a}\right]$, it is clear that the lattice form of the propagator has 15 additional poles, one for each combination of p_μ where the components are either $\frac{\pi}{a}$ or 0. This is the famous problem of fermion doubling [25]. These so-called doublers appear purely as a result of lattice discretisation, and are completely unphysical. The problem is manifest in Eq. (2.21) for $m = 0$ as the derivative form splits the lattice into odd and even sites in each direction.

To remove the doublers, an additional term first proposed by Wilson is introduced to Eq. (2.24) such that it now has the form,

$$\widetilde{D}(p) = m + \frac{i}{a}\sum_{\mu} \gamma_\mu \sin(p_\mu a) + \frac{1}{a}\sum_{\mu}(1 - \cos(p_\mu a))\,. \tag{2.26}$$

Now when p_μ has l components that equal π/a, this new term contributes a factor of $2l/a$ to the mass of the doubler, suppressing the doublers in the limit as $a \to 0$. The position-space Dirac operator corresponding to Eq. (2.26) is

$$D_{\text{Wilson}}(x|y) = \left(m + \frac{4}{a}\right)\delta_{x,y} - \sum_{\mu=1}^{4} \frac{(1-\gamma_\mu)\,U_\mu(x)\,\delta_{x+\hat{\mu},y} + (1+\gamma_\mu)\,U_\mu^\dagger(x-\hat{\mu})\,\delta_{x-\hat{\mu},y}}{2a}\,. \tag{2.27}$$

This expression is frequently rewritten in terms of the *hopping* parameter $\kappa = 1/(2(a\,m+4))$, such that,

$$D_{\text{Wilson}}(x|y) = \delta_{x,y} - \kappa \sum_{\mu=1}^{4} \frac{(1-\gamma_\mu)\,U_\mu(x)\,\delta_{x+\hat{\mu},y} + (1+\gamma_\mu)\,U_\mu^\dagger(x-\hat{\mu})\,\delta_{x-\hat{\mu},y}}{2a}\,. \tag{2.28}$$

Note that in Eq. (2.28) we have absorbed an overall factor of $C = m + 4/a$ into the definition of the quark fields by taking $\psi \to \sqrt{C}\,\psi$ and $\bar{\psi} \to \sqrt{C}\,\bar{\psi}$. As we shall later see, it is the hopping parameter that is set to determine the mass of the bare quarks in the lattice generation procedure. The Wilson Dirac operator is the basis of the lattice form of the fermion action used in this work. So far we have considered only a single flavour of quark, however the extension to multiple flavours is straightforward. We simply introduce fermion fields, ψ_f, and corresponding masses, m_f, for each of the N_f flavours and sum over them, such that the fermion action reads

$$\mathcal{S}_F = a^4 \sum_{f}^{N_f} \sum_{x,y} \bar{\psi}_f(x)\,D_f(x|y)\,\psi_f(y)\,. \tag{2.29}$$

It is worth noting that the Wilson Dirac operator is not the only method by which the Dirac operator may be discretised. Alternative fermion formulations such as staggered [26], overlap [27] and domain-wall [28] fermions have been devised.

Analysis of $\mathcal{S}_G$ proceeds in a similar manner. First we wish define $F_{\mu\nu}$ in terms of the gauge links. To do this, it is necessary to introduce the concept of a Wilson loop on the lattice. Wilson loops are the simplest gluonic gauge-invariant quantity that can be constructed on the lattice. They are formed by taking the trace of the product of gauge links around a closed path $\mathcal{C}$, such that

$$W(\mathcal{C}) = \text{Tr}\left(\prod_{x\in\mathcal{C}} U_\mu(x)\right)\,. \tag{2.30}$$

The 1×1 Wilson loop is given by the trace of the *plaquette*,

$$P_{\mu\nu}(x) = U_\mu(x)\, U_\nu(x+\hat{\mu})\, U_\mu^\dagger(x+\hat{\nu})\, U_\nu^\dagger(x)\,. \tag{2.31}$$

An example plaquette is shown in Fig. 2.1. The relevance of the plaquette can be seen upon taking its Taylor expansion,

$$P_{\mu\nu} = I - ia^2 g\, F_{\mu\nu} - \frac{a^4 g^2}{2}\, F_{\mu\nu}^2 + \mathcal{O}(a^6)\,. \tag{2.32}$$

Utilising this expansion to $\mathcal{O}(a^2)$, we determine that,

$$\frac{a^4}{2}\,\mathrm{Tr}\,(F_{\mu\nu}\, F^{\mu\nu}) = \sum_{\mu,\,\nu} \frac{1}{g^2}\,\mathrm{Tr}\left(I - \frac{1}{2}\left(P_{\mu\nu} + P_{\mu\nu}^\dagger\right)\right)\,. \tag{2.33}$$

Eq. (2.33) is thus sufficient to define a lattice gauge action accurate to $\mathcal{O}(a^2)$, known as the Wilson gauge action,

$$\mathcal{S}_{\text{Wilson}} = \beta \sum_x \sum_{\mu<\nu} \frac{1}{3}\,\mathrm{Tr}\left(I - \frac{1}{2}\left(P_{\mu\nu} + P_{\mu\nu}^\dagger\right)\right)\,, \tag{2.34}$$

where $\beta = 2\,N_c/g^2$ is the lattice coupling constant, and N_c is the number of colours. A factor of 2 is encountered in restricting $\mu < \nu$. This brings us to the point where we have defined the simplest useful forms of the lattice fermion and gluon actions.

2.3 Systematic Improvement

The lattice forms of S_F (Eq. (2.29)) and S_G (Eq. (2.34)) we have arrived at serve as a launching point for further improvement. Although the actions introduced so far have the correct continuum limit as $a \to 0$, any lattice calculation will necessarily be impacted by finite-spacing errors. It is therefore desirable to modify the action to eliminate errors at higher orders of the lattice spacing. This is achieved by the process first introduced by Symanzik [29–31] and involves introducing terms of increasingly higher order in the lattice spacing. These terms are selected such that they cancel the errors introduced by the existing terms to a desired order.

In this work, we employ the improved Wilson fermion action implemented through the introduction of the term

$$-\kappa_f \, c_{SW} \sum_x \sum_{\mu\nu} \frac{i}{2} \, \bar{\psi}_f \, \sigma_{\mu\nu} \, F_{\mu\nu}(x) \, \psi_f(x) \,, \tag{2.35}$$

to Eq. (2.28), where κ_f is the hopping parameter for a quark with flavour f and c_{SW} is a coefficient that may be determined by a variety of methods to best make contact with physical results. At tree level, $c_{SW} = 1$. For our purposes, we use the coefficient as determined in Ref. [32] via renormalisation group arguments, $c_{SW} = 1.715$. Rather than being determined by a single plaquette, as was done in Eq. (2.32), $F_{\mu\nu}$ is constructed from the four plaquettes around the point x as shown in Fig. 2.2, such that

$$F_{\mu\nu} = \frac{1}{4} \sum_{i=1}^{4} \frac{1}{2i} \left(P^{(i)}_{\mu\nu}(x) - P^{(i)\dagger}_{\mu\nu}(x) \right) \,, \tag{2.36}$$

The shape of this combination of links leads to this definition of $F_{\mu\nu}$ often being referred to as the 'clover' definition. Hence the full fermion action is

$$\begin{aligned} \mathcal{S}_{\text{improved}} = \sum_f^{N_f} \sum_x \Bigg[& \bar{\psi}_f(x) \, \psi_f(x) - \kappa_f \, c_{\text{SW}} \sum_{\mu,\nu} \frac{i}{2} \, \bar{\psi}_f(x) \, \sigma_{\mu\nu} \, F_{\mu\nu}(x) \, \psi_f(x) \\ & - \kappa_f \sum_\mu \Big\{ \bar{\psi}_f(x) \, (1 - \gamma_\mu) \, U_\mu(x) \psi_f(x + \hat{\mu}) \\ & + \bar{\psi}_f(x) \, (1 + \gamma_\mu) \, U(x - \hat{\mu})^\dagger \psi_f(x - \hat{\mu}) \Big\} \Bigg] \,. \end{aligned} \tag{2.37}$$

This improved action serves to remove $\mathcal{O}(a)$ errors from the fermion action introduced by the Wilson term and is used for the generation of all dynamical ensembles utilised in this work. While the quark mass also encounters $\mathcal{O}(a)$ improvement, we refer to the pion mass, m_π, as a measure of the quark mass considered in the simulation.

Turning to the gluon action, we make use of two improved actions in this work. The first, used in Chapter 4, is known as the Lüscher-Weisz action [33], and is given by,

$$\begin{aligned} \mathcal{S}_{LW} = \sum_x \frac{\beta}{3} \Bigg[& \frac{5}{3} \sum_{\mu<\nu} \text{Tr} \left(I - \frac{1}{2} \left(P_{\mu\nu} + P^\dagger_{\mu\nu} \right) \right) \\ & - \frac{1}{12 \, u_0^2} \sum_{\text{rectangles}} \text{Tr} \left(I - \frac{1}{2} \left(R_{\mu\nu} + R^\dagger_{\mu\nu} \right) \right) \Bigg] \,, \end{aligned} \tag{2.38}$$

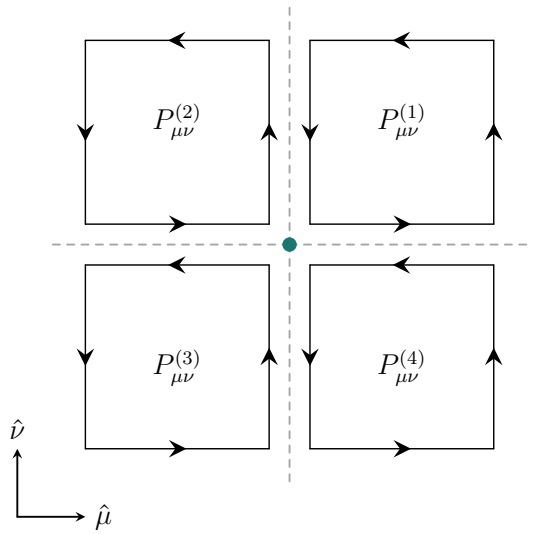

Fig. 2.2 The four plaquettes that compose the clover combination.

where $R_{\mu\nu}$ is the 1×2 rectangular Wilson loop, the sum over rectangles include two orientations and $\mu < \nu$, and u_0 is the tadpole improvement factor [34]

$$u_0 = \left(\frac{1}{3}\operatorname{Re}\operatorname{Tr}(P_{\mu\nu})\right)^{\frac{1}{4}} . \tag{2.39}$$

Tadpole improvement is an alternative method used to determine improvement coefficients such that $\mathcal{O}(a^2)$ errors are suppressed, leading to better contact with continuum physics.

The second of the gauge actions employed in this work is the Iwasaki gauge action [35],

$$\begin{aligned}\mathcal{S}_I =& \frac{\beta}{6}\Bigg[c_0 \sum_{\mu<\nu} \operatorname{Tr}\left(I - \frac{1}{2}\left(P_{\mu\nu} + P^{\dagger}_{\mu\nu}\right)\right) \\ &+ c_1 \sum_{\text{rectangles}} \operatorname{Tr}\left(I - \frac{1}{2}\left(R_{\mu\nu} + R^{\dagger}_{\mu\nu}\right)\right)\Bigg] ,\end{aligned} \tag{2.40}$$

where $c_1 = -0.331$ and $c_0 = 1 - 8\,c_1 = 3.648$ are numerical coefficients calculated via renormalisation group arguments. Both of these gluon actions aim to eliminate errors at $\mathcal{O}(a^2)$.

2.4 Gauge Field Generation

Once a gluon and fermion action have been selected, one can then generate lattice configurations by producing gauge links $U_\mu(x)$ that are drawn from the probability distribution, $\exp(-\mathcal{S})$. This sampling can be performed via a number of Monte-Carlo techniques. If $\mathcal{S}_F$ is omitted from the action, one can generate so-called 'pure gauge' or 'pure Yang-Mills' configurations. Even in pure gauge, it is not trivial to sample the desired $SU(3)$ probability distribution. However, it is simple to directly sample the same distribution for $SU(2)$, which is the motivation behind the famous Cabbibo-Marinari heatbath method [36]. This method samples the three $SU(2)$ subgroups that compose $SU(3)$ and uses the resultant $SU(2)$ links to construct a thermalised $SU(3)$ ensemble.

The addition of dynamical fermions adds significant complexity to the lattice generation process. To understand why, it is necessary to briefly diverge and discuss how integration over the fermionic degrees of freedom is performed. Recall that the goal of the lattice is to evaluate operator expectation values, $\langle O \rangle$, of the form given in Eq. (2.14). These expectation values can be divided into a gluonic and fermionic expectation value, such that

$$\langle O \rangle = \langle \langle O \rangle_F \rangle_G \,, \tag{2.41}$$

where

$$\langle O \rangle_F = \frac{1}{Z_f[U]} \int \mathcal{D}[\psi,\, \bar{\psi}]\, e^{-S_F[\psi, \bar{\psi}, U]}\, O[\psi,\, \bar{\psi},\, U] \,, \tag{2.42}$$

is the fermionic expectation value and

$$\langle O' \rangle_G = \frac{1}{Z} \int \mathcal{D}[U]\, e^{-S_G[U]}\, Z_F[U]\, O'[U] \,, \tag{2.43}$$

is the gluonic expectation value. For the purposes of this discussion, the focus will be on the fermionic expectation value, Eq. (2.42). The fermionic partition function,

$$Z_F[U] = \int \mathcal{D}[\psi,\, \bar{\psi}] e^{-S_F[\psi, \bar{\psi}, U]} \,, \tag{2.44}$$

that appears in the integrand of Eq. (2.43) will play a crucial role in the difficulty of including dynamical fermions in lattice simulations, as we shall soon see.

To integrate over fermionic variables, one must account for fermi statistics. Fermi statistics appear as an antisymmetry between fermionic degrees of freedom, such that

$$\psi\,\psi' = -\psi'\,\psi\,, \quad \bar{\psi}\,\psi' = -\psi'\,\bar{\psi}\,, \quad \bar{\psi}\,\bar{\psi}' = -\bar{\psi}'\,\bar{\psi}\,, \tag{2.45}$$

where the primed variables indicate different quantum numbers in the fermion field. To encode this property, fermionic degrees of freedom are considered to be anticommuting *Grassmann numbers* [37].

To familiarise ourselves with some of the properties of Grassmann numbers, consider N Grassmann numbers, η_i, $i = 1, \ldots, N$, that obey

$$\eta_i\,\eta_j = -\eta_j\,\eta_i\,, \tag{2.46}$$

for all i, $j \in 1, \ldots, N$. This naturally implies that $\eta_i^2 = 0$. Thus, any power series of Grassmann numbers must have only a finite number of terms as one cannot have terms containing the same Grassmann number. For example, if $N = 2$, the highest order polynomial one can have is

$$f(\eta_1,\,\eta_2) = a_0 + a_1\,\eta_1 + a_2\,\eta_2 + a_{12}\eta_1\,\eta_2\,, \tag{2.47}$$

where the a_i and a_{12} are complex Grassmann coefficients. Integrals over Grassmann numbers also satisfy the normalisation conditions

$$\int \prod_{i=1}^{N} d\eta_i\,\eta_1\,\eta_2 \ldots \eta_N = 1\,, \tag{2.48}$$

and

$$\int \prod_{i=1}^{N} d\eta_i\,1 = 0\,. \tag{2.49}$$

As we have already seen in Eq. (2.29), it is possible to write the fermion action in a matrix bilinear form. We are therefore motivated to consider integrals of the form

$$Z_F = \int \prod_{i=1}^{N} d\eta_i\,d\bar{\eta}_i\,\exp\left(\sum_{i,j=1}^{N} \bar{\eta}_i\,M_{ij}\,\eta_j\right)\,, \tag{2.50}$$

where the $\bar{\eta}_i$ are another set of N Grassmann numbers. To solve this integral, we observe that $\eta_i' = M_{ij}\,\eta_j$ is a linear change of integration variables. Such a change of integration variables introduces a factor of $\det[M]$ (see Appendix A.2 for a derivation),

which allows us to rewrite Eq. (2.50) as

$$Z_F = \det[M] \prod_{i=1}^{N} \int d\eta_i' \, d\bar{\eta}_i \exp \bar{\eta}_i \, \eta_i' \tag{2.51}$$

$$= \det[M] \prod_{i=1}^{N} \int d\eta_i' \, d\bar{\eta}_i \, (1 + \bar{\eta}_i \eta_i') \tag{2.52}$$

$$= \det[M] \,, \tag{2.53}$$

where in the second line we expanded the exponential as a power series and made use of Eq. (2.46) to limit the polynomial to first order. In the final line we made use of Eq. (2.48) and Eq. (2.49) to resolve the integral.

Another valuable result that can be derived from Eq. (2.51) is known as Wick's theorem, which states that an expectation value over Grassmann numbers can be exactly solved as

$$\langle \eta_{i_1} \bar{\eta}_{j_1} \dots \eta_{i_N} \bar{\eta}_{j_N} \rangle_F = (-1)^n \sum_{P(1,2,\dots,N)} \operatorname{sign}(P) \, (M^{-1})_{i_1 j_{P_1}} \dots (M^{-1})_{i_N j_{P_N}} \,, \tag{2.54}$$

where the sum runs over permutation of $1, \dots, N$ and $\operatorname{sign}(P)$ is the sign of the permutation.

The significance of the combination of Eq. (2.51) and Eq. (2.54) is immediately apparent. It is clear that the fermion generating functional $Z_F[U]$ is actually the determinant of the Dirac operator $D(x|y)$, and that Fermion expectation values can be explicitly calculated from the inverse of the Dirac operator. Ignoring for the moment the computational complexity of such a calculation, this means that in the process of generating lattice ensembles one only needs to be concerned with sampling the gluon fields, as the fermionic degrees of freedom can be integrated out. Thus, the probability distribution one is attempting to sample when accounting for N_f flavours of dynamical fermions simply reads

$$\frac{1}{Z} \, e^{-\mathcal{S}_G[U]} \prod_{f=1}^{N_f} \det[D_f] \,. \tag{2.55}$$

The simplicity of Eq. (2.55) belies the increased complexity required to sample from this distribution. The sources of this complexity are twofold. Firstly is the fact that computing an $N \times N$ matrix determinant is of $\mathcal{O}(N!)$ complexity. Recalling that N is governed by the lattice volume, this is prohibitively expensive even for moderate lattice sizes. To ameliorate this issue, an analogy is drawn between Grassmann integration

and integrals over complex bosonic fields, ϕ. These fields are known as *pseudofermion* fields. The analogy arises from the fact that the Gaussian integral over Grassmann fields, ψ and $\bar{\psi}$, given in Eq. (2.50), can be related to the integral over bosonic fields, ϕ, such that

$$\int \mathcal{D}[\psi, \bar{\psi}]\, e^{-\bar{\psi}\, D\, \psi} = \det[D] = \int \mathcal{D}[\phi,\, \phi^\dagger]\, e^{-\phi^\dagger\, D^{-1}\, \phi}\,, \tag{2.56}$$

where the bilinear indices are implied and we adopt the simplified notation $D[\psi, \bar{\psi}] = \prod_{i=1}^{N} d\psi_i\, d\bar{\psi}_i$ and $D[\phi, \phi^\dagger] = \pi^{-N} \prod_{i=1}^{N} d\phi_i\, d\phi_i^\dagger$. Thus the full effective action is written as

$$\mathcal{S}_{\text{eff}}[U,\, \phi,\, \phi^\dagger] = \mathcal{S}_G[U] + \phi^\dagger\, D^{-1}\, \phi\,. \tag{2.57}$$

With respect to this action, the partition function becomes

$$\mathcal{Z} = \int \mathcal{D}[U,\, \phi,\, \phi^\dagger]\, e^{-\mathcal{S}_{\text{eff}}[U,\, \phi,\, \phi^\dagger]}\,. \tag{2.58}$$

We therefore seek to sample both the gauge and pseudofermion fields to generate gauge field samples from the distribution $P(U) = \exp\left(-\mathcal{S}_{\text{eff}}\right)$. It must be emphasised that because the pseudofermion fields may always be integrated out to a function of the gauge fields, the objective of the sampling procedure is still to obtain only the gauge fields, with the understanding that an integral over gauge fields distributed according to $P(U)$ will implicitly contain the integral over the pseudofermion fields as well.

The second issue with sampling the fermionic contribution arises from the highly non-local nature of the fermion determinant. The general method that we wish to employ is as follows:

1. Propose a random gauge field, U_μ with action $\mathcal{S}$.
2. Update one or multiple gauge links in a micro-reversible manner to obtain a new gauge field, U'_μ. This updated field has action S'.
3. Accept the new configuration with probability $\min\left(1,\, \exp\left(-\frac{S'}{\mathcal{S}}\right)\right)$.

In pure gauge theory, determining the acceptance probability is computationally cheap, as the ratio of the new action to the old only depends on the local neighbourhood of the updated link(s). The introduction of the fermion determinant removes this locality, an hence requires a resampling of the pseudofermion fields for every update step. Despite the computational improvement brought about through the use of pseudofermions, this is still an expensive proposition. To resolve this, one may try updating many links at a time to reduce the number of samples. However, this leads to larger changes in the

action at each update step, resulting in a lowered acceptance probability and hence more iterations. Thus one finds themselves in a bind. Either option will require a large number of expensive calculations with the whole process scaling with the square of the lattice volume.

To resolve this computational inefficiency, the hybrid Monte Carlo (HMC) method [38, 39] was devised. The key idea is that one wishes to perform larger changes to the gauge field but retain a reasonable acceptance probability by following a physically motivated update trajectory. This is done by introducing ficticious momenta $P \in SU(3)$ which are conjugate to the gauge field U, then evolving P and U along the trajectory defined to preserve the fictitious Hamiltonian,

$$H[U, P] = \frac{1}{2}P^2 + \mathcal{S}[U]\,. \tag{2.59}$$

Hamilton's equations for this system are

$$\frac{\partial P}{\partial \tau} = -\frac{\partial \mathcal{S}}{\partial U}\,, \tag{2.60}$$

$$\frac{\partial U}{\partial \tau} = P\,, \tag{2.61}$$

where τ is the computer-time evolution of the system. These equations are known as the molecular dynamics equations due to their origins in describing the evolution of a classical system. If U were to be evolved exactly along this path, the new configuration would always be accepted, although in reality numerical errors will result in deviations from this exact trajectory.

The general steps for a HMC update algorithm are as follows:

1. Sample pseudofermion fields ϕ distributed according to the distribution $P(\phi) = \exp\left(-\phi^\dagger\, D^{-1}\, \phi\right)$.

2. For a given initial gauge field, U, sample conjugate momenta, P, according to the distribution $\exp\left(-\operatorname{Tr}[P^2]\right)$.

3. Evolve U and P according to the molecular dynamics equations to obtain U' and P'.

4. Accept/reject U' with probability $\min\left(1, \exp\left(-\mathcal{S}'_{\text{eff}}/\mathcal{S}_{\text{eff}}\right)\right)$. Note that in calculating $\mathcal{S}'_{\text{eff}}$, ϕ is reused from step 1.

Table 2.1 A summary of the lattice ensembles used in this work [38]. The dynamical ensembles both use the improved fermion action described in Eq. (2.37) and have a heavy strange quark mass given by $\kappa_s = 0.13640$.

Type	$N_s^3 \times N_t$	$\mathcal{S}_G$	$a\,(\mathrm{fm})$	β	$\kappa_{\mathrm{u,d}}$	$m_\pi\,(\mathrm{MeV})$	N_{config}
Pure gauge	$20^3 \times 40$	$\mathcal{S}_{LW}$	0.125	4.52	–	–	100
Pure gauge	$32^3 \times 64$	$\mathcal{S}_I$	0.100	2.58	–	–	200
Dynamical	$32^3 \times 64$	$\mathcal{S}_I$	0.102	1.90	0.13700	701	200
Dynamical	$32^3 \times 64$	$\mathcal{S}_I$	0.093	1.90	0.13781	156	200

This process results in gauge fields U that are sampled according to the effective action, and thus incorporate the effect of dynamical fermions on the gauge fields.

For this work, we make use of four lattice ensembles. Two are pure gauge and two are $(2+1)$ flavour ensembles generated with the full QCD action from the PACS-CS collaboration [38]. These dynamical ensembles used the improved fermion action given in Eq. (2.37) and the improved gluon action given in Eq. (2.40). The parameters for the lattice ensembles used in this work are summarised in Table. 2.1.

Once one has generated lattice configurations, it is then possible to analyse the resultant ensemble to extract a wide range of QCD properties by evaluating operators via the method outlined in Eq. (2.10). This is the foundation of all lattice analyses, and brings us to a position where we can introduce the core concept underlying the majority of this work; the centre vortex model of QCD.

Chapter 3

Centre Vortices on the Lattice

An essential feature of Quantum Chromodynamics is the fact that it admits a highly non-trivial vacuum structure. The consequences of this property are far-reaching and lead to the distinctive properties of QCD mentioned in Chapter 1: confinement and dynamical chiral symmetry breaking (χ_{SB}) resulting in the dynamical generation of mass. Determining the origin of these properties is a topic of great interest, as it is currently unknown how the QCD Lagrangian shown in Eq. (2.1) gives rise to this behaviour.

The topology of the QCD vacuum is thought to capture the origin of both confinement and $D\chi_{\mathrm{SB}}$. Many theories have emerged over the years to explain this relationship between vacuum structure and the properties of QCD, resulting in a range of topological theories, including Abelian monopoles [40–48], instantons [49–60] and, most significantly to this work, centre vortices [2–20, 54, 61–74].

Abelian monopoles are the oldest topological explanation for confinement [40, 44]. The theory arises from an analogy to type II superconductors, in which magnetic flux is confined into tubes of quantised flux amongst a medium of electrically charged bosons. Abelian monopole theory postulates that confinement of quarks arises in a similar manner, except with the magnetic and electric charge roles reversed [65]. The magnetic monopoles are the medium, and the confinement of electrically charged particles, the quarks, is the result. This role-reversal of electric and magnetic charges is why this mechanism of confinement is known as *dual*-superconductivity [40, 44], brought about via the presence of Abelian magnetic monopoles. Despite the appealing analogy to superconductivity, this theory has fallen out of favour due to the incorrect scaling behaviour of the static quark potential found in lattice studies [75, 76].

Instantons are regions of non-trivial topological charge density that have shown promise in explaining the dynamical generation of mass due to their association with zero-modes of the Dirac operator [77]. The relationship between centre vortices and instantons will be explored in Section 4.3.

Of these theories, centre vortices have emerged as the leading and most fundamental explanation for the unique properties of QCD [5–12, 14–20, 61–69, 72, 74]. Lattice calculations have demonstrated that centre vortices are connected to both confinement [13–17] and $D\chi_{\mathrm{SB}}$ [18–20]. However, as shall be discussed in greater detail later in this chapter, there remain persistent quantitative discrepancies between the centre vortex model and QCD predictions. Explanation of this tension presents an open question, and motivates much of the work developed here.

This chapter will first present a description of centre vortices and briefly motivate how they can give rise to confinement through a simple example. We will then describe how centre vortices are identified on the lattice, as well as some of the properties they possess. With this understanding developed, we will review the literature regarding centre vortices and their phenomenology prior to the undertaking of this original research. Finally, we shall describe a number of lattice smoothing algorithms that are used throughout this work. This will build the necessary foundation to understand the new results presented in the following chapters.

3.1 What are Centre Vortices?

Centre vortices were originally theorised as a method by which quarks are confined [2, 3]. The general postulate is that the QCD vacuum is dominated by regions of randomly distributed quantised flux that is sufficient to result in confinement of quarks [78, 79]. Centre vortices in four dimensions are 4D volumes of the $SU(N)$ gauge field that carry charge corresponding to the centre of the group, Z_N. Z_N is the group of elements that commute with all elements of $SU(N)$, and is given by,

$$\mathbb{Z}_N = \left\{ \exp\left(\frac{2\pi i\, m}{N}\right) I \,|\, m = 0, 1, \ldots, N-1 \right\}. \tag{3.1}$$

Hence for $SU(N)$ there are $N-1$ non-trivial centre elements. In the case of QCD, we are of course considering $SU(3)$, and hence frequently refer to Z_3, where

$$\mathbb{Z}_3 = \left\{ \exp\left(\frac{2\pi i\, m}{3}\right) I \,|\, m = -1, 0, +1 \right\}. \tag{3.2}$$

In 3D, these centre vortices appear as tubes of finite radius carrying this chromomagnetic centre charge. Due to the Bianchi identity,

$$\epsilon_{\mu\nu\rho\sigma}\, \partial_\nu\, F_{\rho\sigma} = 0\,, \tag{3.3}$$

these centre vortex tubes are required to be closed to ensure conservation of chromomagnetic flux [12].

We do not identify the so-called extended *thick* vortices. Instead, picturing the tubes of centre flux as a rotating vortex, we identify structures analogous to the axis of this tube, known as a thin vortex. Hence, on the lattice, we refer to the identified vortices as *thin* or projected P-vortices. These thin vortices appear as lines rather than tubes in three dimensions, or as 2D sheets in four dimensions. Moreover, it has been shown that thin vortices identified on the lattice are correlated with the location of physical thick vortices [10, 80]. For the remainder of this work we will focus on the properties of thin centre vortices.

The ability of centre vortices to give rise to confinement is the result of their interaction with Wilson loops (see Eq. 2.30). A centre vortex that intersects a Wilson loop results in the Wilson loop acquiring the vortex's centre phase, z, such that

$$W(C) \to z\, W(C)\,. \tag{3.4}$$

A visualisation of a centre vortex piercing a Wilson loop in 3D is shown in Fig. 3.1. The simple property presented in Eq. (3.4) leads to the remarkable predictions of the centre vortex model. To illustrate this, it is necessary to first detail the connection between Wilson loops and the calculation of the static quark potential.

The static quark potential is the potential energy between two infinitely heavy, stationary quarks as a function of their separation, r. This can be calculated on the lattice by considering the expectation value of a Wilson loop of spatial extent r and temporal extent t,

$$\langle W(r,\, t)\rangle = \sum_\alpha \lambda^\alpha(r)\, \exp\left(-V^\alpha(r)\, t\right)\,. \tag{3.5}$$

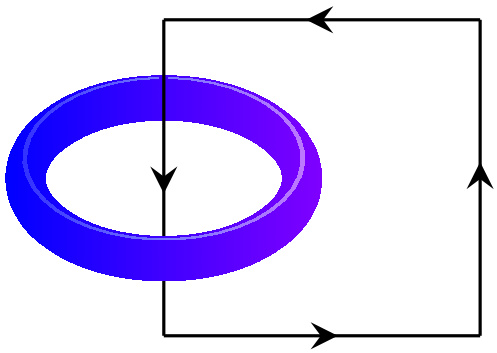

Fig. 3.1 A Wilson loop (solid black line) pierced by a thick centre vortex (blue torus) in 3D.

Here, $V^\alpha(r)$ are the static quark potential eigenstates and the $\lambda^\alpha(r)$ are the couplings to these states. As the temporal extent grows, it is clear that the higher-energy states will decay until only the ground state potential V^0 remains. Greater detail of the calculation of the static quark potential will be provided in Chapter 5.

The confinement of quarks can be studied by considering the long-range behaviour of the static quark potential. For particles with perturbative gluon exchange, this potential is Coulomb-like, decaying to a constant value at large r. However, if quarks are confined, the potential is expected to become linear in the pure-gauge theory as the separation of the quarks increases. If this occurs, the slope of this linear region is known as the string tension, σ.

To understand the relationship between centre vortices and confinement, we consider the situation in which centre vortices are randomly distributed throughout the vacuum, a property hereafter referred to as *vortex percolation*. Consider a two-dimensional plane of area L^2, with $2N$ vortices piercing the plane. Assuming an even distribution of vortices, the total vortex density is $\rho = 2N/L^2$. As there are two $SU(3)$ vortex types, corresponding to the two non-trivial phases, $z = \exp(\pm 2\pi i/3)$, we assume that there is an equal distribution of vortex phases, i.e. there are N vortices of each type. The probability of finding n vortices of a given phase in some region of the plane $A \subset L^2$ is equal to,

$$P_N(n) = \binom{N}{n} \left(\frac{A}{L^2}\right)^n \left(1 - \frac{A}{L^2}\right)^{N-n} . \tag{3.6}$$

The expectation value of the Wilson loop around the perimeter of A can therefore be written as,

$$\langle W(\partial A)\rangle = \sum_{m,n=0}^{N} \left(\exp\left(\frac{2\pi i}{3}\right)\right)^{n} P_N(n) \left(\exp\left(-\frac{2\pi i}{3}\right)\right)^{m} P_N(m)\,. \tag{3.7}$$

As the vortex phases are uncorrelated, we may separate the sum to write,

$$\langle W(\partial A)\rangle = \sum_{n=0}^{N} \left(\exp\left(\frac{2\pi i}{3}\right)\right)^{n} P_N(n) \sum_{m=0}^{N} \left(\exp\left(\frac{2\pi i}{3}\right)\right)^{m} P_N(m)\,. \tag{3.8}$$

Consider the first sum in Eq. (3.8),

$$\begin{aligned}\sum_{n=0}^{N} \left(\exp\left(\frac{2\pi i}{3}\right)\right)^{n} P_N(n) &= \left(1-\frac{A}{L^2}\right)^{N} \sum_{n=0}^{N} \binom{N}{n} \left(\exp\left(\frac{2\pi i}{3}\right) \frac{A}{L^2}\left(1-\frac{A}{L^2}\right)^{-1}\right)^{n} \\ &= \left(1+\left(\exp\left(\frac{2\pi i}{3}\right)-1\right)\frac{A}{L^2}\right)^{N}, \end{aligned} \tag{3.9}$$

where we have made use of the binomial series to evaluate the sum. The second term in Eq. (3.8) may be calculated similarly. Hence the total expectation value is,

$$\begin{aligned}\langle W(\partial A)\rangle &= \left(1+\left(\exp\left(\frac{2\pi i}{3}\right)-1\right)\frac{A}{L^2}\right)^{N} \left(1+\left(\exp\left(\frac{-2\pi i}{3}\right)-1\right)\frac{A}{L^2}\right)^{N} \\ &= \left(1-3\frac{A}{L^2}+3\left(\frac{A}{L^2}\right)^{2}\right)^{N} \\ &= \left(\left(\frac{A}{L^2}\right)^{3}+\left(1-\frac{A}{L^2}\right)^{3}\right)^{N}. \end{aligned} \tag{3.10}$$

Rewriting Eq. (3.10) in terms of the vortex density $\rho = 2N/L^2$, we have,

$$\langle W(\partial A)\rangle = \left(\left(\frac{A\rho}{2N}\right)^{3}+\left(1-\frac{A\rho}{2N}\right)^{3}\right)^{N}. \tag{3.11}$$

Now we take the limit as $N, L^2 \to \infty$ whilst keeping ρ constant to arrive at,

$$\lim_{N,L^2\to\infty} \langle W(\partial A)\rangle = \exp\left(-\frac{3}{2}\rho A\right). \tag{3.12}$$

Letting $A = r\times t$ be the area of the Wilson loop as in Eq. (3.5), we see that $V^0(r) = \frac{3}{2}\,\rho\, r$, so the static quark potential rises linearly with string tension $\sigma = \frac{3}{2}\,\rho$, exactly as it should in a confining theory. Eq. (3.12) demonstrates an *area law* behaviour of the

Wilson loop; this is often taken as a requirement for confinement [7, 81]. We see then that we have, from a set of simple assumptions, constructed a model that exhibits confinement.

An interesting corollary of this result arises if the vortices are instead not permitted to percolate [63], meaning that there is a correlation between the location of vortices of opposite sign. This can be viewed as imposing the condition that the maximum vortex size is limited to some finite separation, d. In this case, the vortex phases will cancel out everywhere except for the area of width d around the perimeter of A. Thus the Wilson loop instead has expectation value,

$$\langle W(r,\, t)\rangle = \exp\left(-\frac{3}{2}\,\rho_V\, 2(r+t)\, d\right)\,. \tag{3.13}$$

Clearly $V^0(r)$ is no longer linear, and instead Eq. (3.13) goes like the perimeter of the Wilson loop, instead of the area. Hence an upper bound on the size of vortices results in a loss of confinement. This result has lead to the percolation of vortices being viewed as an *order parameter* for confinement. Indeed, it has been shown in $SU(2)$ lattice studies that as the temperature increases and the theory tends towards the high-temperature deconfining phase, vortices indeed cease to percolate [8, 63].

These simple calculations motivate the significant power of the centre vortex theory. To be able to reproduce confining behaviour from a group containing only three elements (in the case of QCD) is a remarkable property. Of course the static quark potential is far from the full picture of QCD, and the vortices considered so far have not arisen from the QCD Lagrangian. What we wish to do now is discuss how we can identify the centre vortices present in lattice gauge field configurations generated according to the methods outlined in Chapter 2. From there, we may begin to explore their ability to explain the key properties of QCD.

3.2 Identifying Centre Vortices

To identity thin centre vortices on the lattice, we wish to bring every gauge link as close as possible to an element of $\mathbb{Z}_3$. This is done by transforming each gauge field configuration to maximal centre gauge (MCG). To do this, we find the gauge

transformation $\Omega(x)$ that serves to maximise the functional [13, 17],

$$R = \frac{1}{V\, N_{\text{dim}}\, n_c^2} \sum_{x,\mu} \left| \operatorname{Tr} U_\mu^\Omega(x) \right|^2 . \tag{3.14}$$

After fixing to maximal centre gauge, the nearest centre element is defined by finding the minimum difference in phase between $\operatorname{Tr} U_\mu(x)$ and one of the elements of $\mathbb{Z}_3$. $U_\mu(x)$ is then mapped to this nearest centre element to obtain the vortex-only configurations, $Z_\mu(x)$. As each link is now an element of $\mathbb{Z}_3$, the plaquettes also belong to the centre group. Vortices are located in this projected configuration by identifying non-trivial plaquettes, as a non-trivial flux indicates that this plaquette is pierced by a vortex due to the relation described in Eq. (3.4).

This definition of centre vortices allows us to write the plaquettes on the vortex-only ensembles as [12, 67]

$$P_{\mu\nu}(x) = \exp\left(\frac{\pi i}{3}\, \epsilon_{\mu\nu\kappa\lambda}\, m_{\kappa\lambda}(\bar{x}) \right) , \tag{3.15}$$

where $m_{\kappa\lambda}(\bar{x}) \in \{-1, 0, 1\}$ defines the directed vortex charge orthogonal to the plaquette and based at the dual-lattice site $\bar{x} = x + \frac{a}{2}(\hat{\mu} + \hat{\nu} - \hat{\kappa} - \hat{\lambda})$. Note also that $m_{\kappa\lambda}(\bar{x})$ is antisymmetric under index permutation. This definition of the plaquette provides us with a natural method of considering vortex lines present on 3D spatial slices of the lattice, as will be essential for the analysis of vortex structure presented in Chapters 4 and 7. This is done by simply fixing the value of λ to the desired time-oriented dimension, which results in,

$$P_{ij}(x) = \exp\left(\frac{2\pi i}{3}\, \epsilon_{ijk\lambda}\, m_{k\lambda}(\bar{x}) \right) , \tag{3.16}$$

where i, j, k denote the three spatial coordinates and there is no sum over λ. In this interpretation, i and j then denote the plane in which the spatial plaquette is calculated, whilst $\hat{k}$ is the direction of the vortex line orthogonal to this plane.

Eq. (3.15) also allows us to make connection with the conservation of vortex flux required by the Bianchi identity, Eq. (3.3). Firstly, recall the relationship between the field strength tensor and the plaquette presented in Eq. (2.32). Rearranging this expression to $\mathcal{O}(a^2)$ we find

$$iga^2 F_{\mu\nu}(x) = 1 - P_{\mu\nu}(x) . \tag{3.17}$$

Substituting Eq. (3.17) into Eq. (3.3) and making use of the vortex plaquette definition Eq. (3.15) we find that

$$\epsilon_{\mu\nu\kappa\lambda}\,\epsilon_{\mu\nu\sigma\tau}\,\bar{\partial}_\kappa\, m_{\sigma\tau}(\bar{x}) = 0, \tag{3.18}$$

where $\bar{\partial}_\kappa = \frac{\partial}{\partial \bar{x}_\kappa}$. Recalling $m_{\kappa\lambda}$ is antisymmetric and

$$\epsilon_{\mu\nu\kappa\lambda}\,\epsilon_{\mu\nu\sigma\tau} = 2\left(\delta_{\kappa\sigma}\delta_{\lambda\tau} - \delta_{\kappa\tau}\delta_{\lambda\sigma}\right), \tag{3.19}$$

one finds

$$\bar{\partial}_\kappa\, m_{\kappa\lambda}(\bar{x}) = 0. \tag{3.20}$$

To see how Eq. (3.20) requires that the vortex flux through a given three-dimensional cube be conserved, consider the example of setting $\lambda = 4$. Then

$$\bar{\partial}_k\, m_{k4}(\bar{x}) = \vec{\nabla}\cdot\vec{m}(\bar{x}) = 0\,, \tag{3.21}$$

with $m_{\kappa 4} = m_k = [\vec{m}]_k$ being the spatially-oriented vortex flux piercing the spatial plaquette $P_{\mu\nu}(x)$. Recalling the divergence theorem,

$$\int_V d^3r\,\vec{\nabla}\cdot\vec{m}(\vec{r}) = \int_{\partial V} d\vec{S}\cdot\vec{m}(\vec{r}) = 0, \tag{3.22}$$

and $m_k = \pm 1$, centre-vortex flux entering a face of a spatial cube V has to leave by another face.

Once centre projection has been performed, we may subsequently define the vortex removed configurations as $R_\mu(x) = Z_\mu^\dagger(x)\,U_\mu(x)$. $R_\mu(x)$ should then capture the physics remaining after vortex removal. The result of this method of vortex identification is that we produce the two *vortex-modified* ensembles, $Z_\mu(x)$ and $R_\mu(x)$. Hence for the remainder of this work we will consider sets of three ensembles, known as the

- Original, untouched (UT) fields, $U_\mu(x)$,
- Vortex-only (VO) fields, $Z_\mu(x)$, and
- Vortex-removed (VR) fields, $R_\mu(x)$.

3.2.1 Parallel MCG Fixing

Given the size of the larger lattices used in this work, it is necessary to implement a parallel version of the MCG algorithm, which proceeds as follows. To construct

the maximal centre gauge transformation $\Omega(x)$, it is sufficient to consider the nearest-neighbour contributions from $U_\mu(x)$ and $U_\mu(x-\hat{\mu})\ \forall\,\mu\ \in\{1,2,3,4\}$. For each x, one then seeks to maximise the local functional [82]

$$R(x) = \sum_\mu \left|\mathrm{Tr}\,\Omega(x)\,U_\mu(x)\right|^2 + \sum_\mu \left|\mathrm{Tr}\,U_\mu(x-\hat{\mu})\,\Omega(x)^\dagger\right|^2 \tag{3.23}$$

This is achieved by considering each of the three $SU(2)$ subgroups of $SU(3)$. $\Omega(x)_{\mathrm{SU(2)}}$ is then expressed as a linear combination of the $SU(2)$ generators $\vec{\sigma}$ such that

$$\Omega_{\mathrm{SU(2)}}(x) = g_4 I - i\vec{g}\cdot\vec{\sigma}. \tag{3.24}$$

This reduces Eq. (3.23) to a quadratic in $(g_4,\,\vec{g})$ subject to a unitarity constraint that can then be minimised via standard Lagrangian multiplier techniques. Once each $SU(2)$ of the three subgroups is iterated over once and $\Omega(x)$ has been constructed, it is then applied to the nearest-neighbour gauge links. The process is repeated for all other values of x and then iterated until a plateau in R is reached.

As $\Omega(x)$ depends only on its nearest-neighbours, we mask the algorithm to ensure that at any one time we consider only even or odd values of x, where even or odd is defined by whether $\sum_{\mu=1}^{4} x_\mu$ is even or odd. We then distribute regular chunks of the lattice across processors with one shadowed plane in the directions along which the lattice has been subdivided. Once an even or odd sweep has been completed, the updated links are copied to adjacent processors so that they are available for the alternate sweep. A diagram illustratingthis updating scheme, for two processors distributed along one dimension is shown in Fig. 3.2.

The processor boundary is shown with the vertical dashed line. Gauge links are shown with solid black arrows and shadowed gauge links are shown with black dashed arrows. Shown is the update process starting with the even sites (blue circles) followed by the odd sites (red circles):

1. The gauge links adjacent to the even sites are updated with the gauge transformation $\Omega(x)$.

2. The updated links along the boundary are copied to the relevant shadowed locations.

3. The gauge links adjacent to the odd sites are updated.

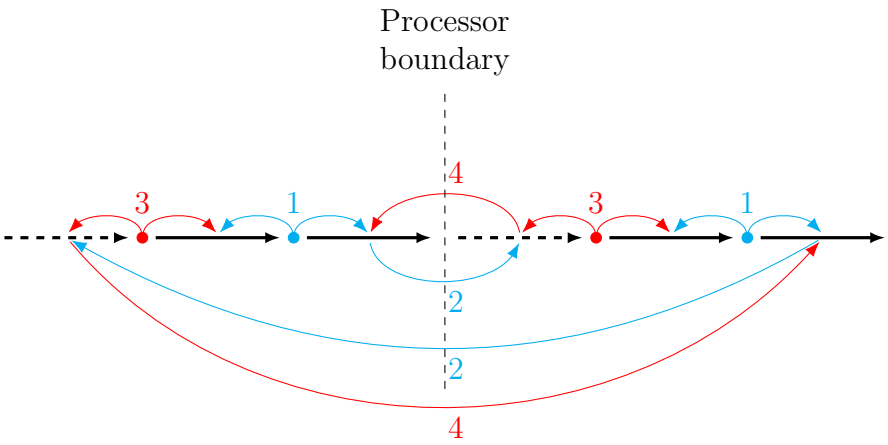

Fig. 3.2 MCG updating scheme for two processors. The update process is described in the text.

4. The updated shadowed links are copied to the relevant locations.

This method of parallel implementation requires a slightly greater number of overall sweeps than the serial implementation, as each update does not have the fully propagated information that would be carried by a serial process starting from one corner of the lattice. However, it has a number of advantages. Most apparent is the real-time reduction in calculation time, as the parallel implementation scales very well thanks to minimal cross-processor memory requirements. Additionally, there is no directionality in this implementation as each site only sees its neighbours during each sweep. This suppresses any inconsistency arising from choice of start point or order of iteration. Given that each site is only affected by its nearest neighbours, this implementation also has the desirable property of being agnostic to the number of processors used in the calculation.

3.3 Properties of Centre Vortices

With the procedure for identifying centre vortices on the lattice established, we now wish to discuss some of the important properties of vortices and how they are examined on the lattice. We will then present a review of the evidence for the centre vortex picture of confinement prior to the undertaking of this work.

Table 3.1 A summary of the possible number of centre vortices piercing a 3D cube centred on $\tilde{x}$ and the interpretation of such points.

$n_{\text{cube}}(x \,\vert\, \hat{\mu})$	Interpretation
0	No vortices present.
1	Terminating vortex, forbidden by conservation of centre charge.
2	Vortex line flowing through the cube.
3	Simple three-way branching point.
4	Vortex self-intersection.
5	Complex five-way branching point.
6	Vortex self-intersection or double branching.

3.3.1 Vortex Branching

An important feature of $SU(3)$ vortices is the presence of vortex branching. Due to the periodicity of the centre phase $z = \exp(2\pi i/3)$, three centre vortices entering or emerging from a 3D cube conserve vortex flux as described by Eq. (3.22). The presence of vortex branching has significant ramifications for the vortex structure of the vacuum, and they provide an additional order parameter for confinement [67]. They will also be shown to have interesting correlations to other topological structures on the lattice in Chapter 4.

It is important to highlight that there is some ambiguity in the nature of vortex branching points [67]. Consider three $m = +1$ vortices emerging from an elementary cube centred on the dual lattice site,

$$\vec{x}' = \vec{x} + \frac{a}{2}(\hat{\imath} + \hat{\jmath} + \hat{k})\,. \tag{3.25}$$

Here $i\,, j\,, k$ are the three spatial coordinates after one dimension has been selected for the time dimension. Again due to the periodicity of the elements of $\mathbb{Z}_3$, this monopole is indistiguishable from the case of a single $m = -1 = +2$ vortex entering the cube and branching to two $m = +1$ vortices, as shown in Fig. 3.3. This issue is related to an overall orientation ambiguity present in the analysis of centre vortex structure. For the purposes of our work, we consider only the former case of $m = -1$, 0, $+1$ and thus three vortices of identical sign emerging from or converging within an elementary cube. In this case, $\vec{m}(\vec{r})$ indicates the directed flow of $m = +1$ centre charge.

Vortex flux through an elementary cube may also entail additional vortices piercing an elementary cube. To fully account for all possible cases, we define $n_{\text{cube}}(x \,|\, \hat{\mu})$. μ denotes the direction along which the lattice has been sliced and hence identifies the remaining three coordinates, $\vec{x}'$, that describe the location within the 3D slice. $n_{\text{cube}}(x \,|\, \hat{\mu})$ therefore counts the number of vortices piercing the elementary cube centred at $\vec{x}'$ when the lattice has been sliced along the μ direction. The interpretation of each value of $n_{\text{cube}}(x \,|\, \hat{\mu})$ is summarised in Table 3.1. Despite the fact that it is possible for points with $n_{\text{cube}}(x \,|\, \hat{\mu}) = 6$ to be triple intersection points rather than double branching points, for the purposes of this work we consider all points with $n_{\text{cube}}(x \,|\, \hat{\mu}) = 3, 5, 6$ to be branching points. The ambiguity around $n_{\text{cube}}(x \,|\, \hat{\mu}) = 6$ is insignificant, as we shall see that cubes pierced by six vortices occur very infrequently.

3.3.2 Vortex and Branching Point Density

We briefly mentioned the notion of vortex density, ρ_V, when presenting the motivation for the vortex model in Section 3.1. It is worth now returning to this quantity with our understanding of vortices on the lattice further developed. The lattice vortex density is an area density, i.e. it is given by the average density of vortices piercing each 2D plane in the lattice. Fortunately, as we average over planes and the area of each plane, each term acquires a factor of the total lattice volume, V. Thus we shall see that we can write the area density in a very compact form. First we define the indicator function,

$$v_{\mu\nu}(x) = \begin{cases} 1, & P_{\mu\nu}(x) = \exp\left(\frac{\pm 2\pi i}{3}\right) I \\ 0, & P_{\mu\nu}(x) = I\,. \end{cases} \tag{3.26}$$

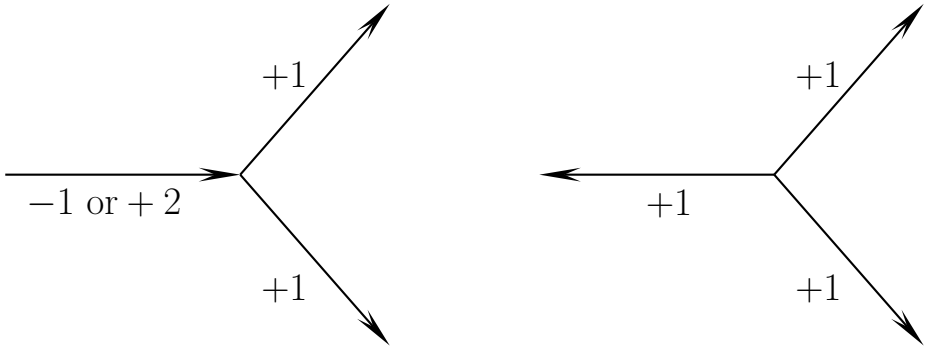

Fig. 3.3 A vortex branching point with centre charge $+2$ or -1 flowing into a vertex (left) is equivalent to a branching point with charge $+1$ flowing out of the vertex (right). The arrows indicate the direction of flow for the labelled charge.

Hence, in lattice units, the vortex density P_V is given by,

$$P_v = \frac{1}{6\,V} \sum_{\substack{\mu\,,\nu \\ \mu<\nu}} \sum_{x} v_{\mu\nu}(x)\,. \tag{3.27}$$

The physical density is then given by,

$$\rho_v = \frac{P_V}{a^2}\,. \tag{3.28}$$

The calculation of the branching point density, ρ_b, proceeds similarly. The branching point density is given by the average volume density of branching points on a 3D slice. Hence we similarly define an indicator function

$$b(x\,|\,\hat{\mu}) = \begin{cases} 1, & n_{\text{cube}}(x\,|\,\hat{\mu}) = 3, 5, 6 \\ 0, & \text{otherwise}\,. \end{cases} \tag{3.29}$$

The branching point density in lattice units is then given by,

$$P_b = \frac{1}{4\,V} \sum_{\mu} \sum_{x} b(x\,|\,\hat{\mu})\,. \tag{3.30}$$

This results in a physical density of,

$$\rho_b = \frac{P_b}{a^3}\,. \tag{3.31}$$

Finally, we also wish to define the naive branching rate, λ_{naive}, which is a simple estimator of the probability that a given vortex line branches as it propagates through space-time [13, 67]. We dub it as naive in anticipation of a more detailed calculation that will be presented in Chapter 7. In physical units, the branching rate is a probability per unit length as it associated with the branching of a vortex line. We first define the indicator,

$$c(x\,|\,\hat{\mu}) = \begin{cases} 1, & n_{\text{cube}}(x\,|\,\hat{\mu}) \neq 0 \\ 0, & \text{otherwise}\,. \end{cases} \tag{3.32}$$

The branching rate is then given by the ratio of the number of elementary cubes containing branching points to the number of elementary cubes pierced by a vortex, i.e.

$$q_{\text{naive}} = \frac{\sum_{\mu} \sum_{x} b(x\,|\,\hat{\mu})}{\sum_{\mu} \sum_{x} c(x\,|\,\hat{\mu})}\,. \tag{3.33}$$

The physical rate is then given by,

$$\lambda_{\text{näive}} = \frac{q_{\text{naive}}}{a} \,. \tag{3.34}$$

These densities have been shown to scale appropriately as the physical limit is approached [13, 67]. Thus, they provide suitable measures to assist in quantifying the vortex structure of the lattice.

3.3.3 Results from Centre Vortices

With our understanding of how centre vortices are identified on the lattice, it is now worthwhile discussing the current lattice results that motivate the significance of the centre vortex picture. The study of centre vortex degrees of freedom extends back to the early days of lattice QCD. To lessen the computational cost, the gauge group was $SU(2)$ for the earliest centre vortex studies. In pure gauge $SU(2)$, the vortex picture is very clear. $SU(2)$ centre vortices alone can fully account for the string tension [83, 84], and the vortex density scales as a physical quantity [85, 86]. Furthermore, vortex removal has been shown to completely remove the string tension [68, 84], remove the infrared enhancement of the gluon propagator [68] and restore chiral symmetry [84, 87]. This provides strong evidence that centre vortices are essential for the emergence of both confinement and $D\chi_{\text{SB}}$ in $SU(2)$ gauge theory.

Motivated by these powerful results, new lattice studies were performed in pure Yang-Mills $SU(3)$ theory. In $SU(3)$, the results are less clear-cut than their $SU(2)$ counterparts. Vortex removal remains a potent indicator of the importance of centre vortices, with removal of vortices still resulting in complete loss of the string tension [20] and degeneracy in the low-lying hadron spectrum [20]. Both these results indicate that centre vortices play a central role in QCD. However, the infrared gluon and quark propagators still retain infrared strength after vortex removal [15, 18], despite significant suppression. There also remains residual dynamical generation of mass in the vortex-removed hadron spectrum [20].

The vortex-only fields provide a similar picture. Agreement between the original and vortex-only results from the infrared gluon propagator, quark propagator, hadron spectrum and string tension can only be achieved after the application of gauge field smoothing [15, 17, 18, 20] (see the next section for a discussion of smoothing). However, the vortex-only results consistently exhibit the same qualitative properties as the original fields, displaying both confinement and $D\chi_{\text{SB}}$, albeit to a lesser extent than

the original gauge fields. A specific example of this is the well-known result that the vortex-only string tension is only $\sim 62\%$ that of the original string tension in $SU(3)$ [13, 16, 17]. The remarkable ability of the centre vortex model to qualitatively capture the salient properties of QCD motivates further investigation. Additionally, understanding why the quantitative agreement that is found so readily in $SU(2)$ is absent in $SU(3)$ remains an open question.

These existing results provide the driving force behind this research. Much as the transition from $SU(2)$ to $SU(3)$ was a natural progession, so to is the transition from pure gauge to full QCD that is undertaken in this work. Inclusion of dynamical fermions in the lattice simulation provides a new setting with which to explore the behaviour of centre vortices. This in turn provides greater context on their role in QCD.

3.4 Smoothing

With this understanding of centre vortices developed, we will now make a slight deviation and discuss smoothing, a common lattice technique utilised when analysing topological objects. The topological charge field on the lattice is highly susceptible to short-range fluctuations, making it necessary to employ algorithms that attempt to smooth these fluctuations without damaging the underlying structure. In this work we employ a variety of smoothing algorithms as each has their own strengths and weaknesses. Here we shall detail the motivation and procedures underpinning these techniques, especially in the context of their application to vortex-only configurations.

3.4.1 Cooling

Cooling is performed by replacing each link by a new link that serves to minimise the local gluon action. To do this, we define the *staples* around a link as the plaquette with the link under consideration removed, as shown in Fig. 3.4. For each link, $U_\mu(x)$, the staples, Σ_μ, are defined as

$$\begin{aligned}\Sigma_\mu(x) = \sum_{\nu\neq\mu} & U_\nu(x)\, U_\mu(x+\hat{\nu})\, U_\nu^\dagger(x+\hat{\mu}) \\ & + U_\nu^\dagger(x-\hat{\nu})\, U_\mu(x-\hat{\nu})\, U_\nu(x-\hat{\nu}+\hat{\mu})\,. \end{aligned} \tag{3.35}$$

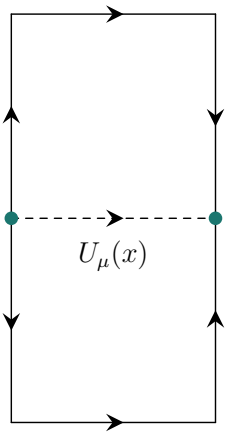

Fig. 3.4 A single term of the staple expression given in Eq. (3.35).

Given this construction, the Wilson action (Eq. (2.34)) may be rewritten as

$$\mathcal{S}_{\text{Wilson}} = \beta \sum_x \left(6 - \operatorname{Re}\operatorname{Tr} \Sigma_\mu(x)\, U_\mu^\dagger(x)\right). \tag{3.36}$$

Minimising the local action corresponds to finding a new $U'_\mu(x)$ that maximises $\operatorname{Re}\operatorname{Tr} \Sigma_\mu(x)\, U'^\dagger_\mu(x) \forall x$. This is performed by identifying three $SU(2)$ matrices, a_i, corresponding to the three subgroups of $SU(3)$, such that $U'_\mu(x) = a_3\, a_2\, a_1\, U_\mu(x)$ [88]. Explicit forms of these matrices are given in Ref. [89].

Cooling may also be improved by inclusion of larger staples to improve preservation of topological objects. It has been shown that $\mathcal{O}(a^4)$ improved three-loop improved cooling is suitable for this purpose [90]. We therefore utilise this algorithm to cool the configurations used in this work.

Whilst effective, cooling presents with a number of difficulties. First and foremost is the computational inefficiency. As cooling seeks to locally minimise the action, all links contained in the staples must be held constant for a given sweep. When the staples are expanded to include larger loop sizes, as is necessary to preserve topological objects, the number of links that must be held constant at each step increases, which reduces the capacity for parallel optimisation.

Cooling is also non-analytic, meaning that there is no set of parameters that smoothly map from $U_\mu(x)$ to $U'_\mu(x)$. This is not an issue for this work, however it can make cooling unsuitable for studies of certain observables that require a smoothness condition to be satisfied. Finally, and perhaps most relevant for this work, is the fact that cooling is susceptible to introducing floating-point errors when performed on vortex-only configurations, as the $SU(2)$ subgroups can have a vanishing determinant

that results in an undefined a_i matrix [89]. For these reasons, we turn our attention to smoothing methods that do not suffer from these issues.

3.4.2 APE Smearing

Instead of locally minimising the action, APE smearing [91, 92] seeks to replace each link with an average over its neighbours. This is done by first defining,

$$V_\mu(x) = (1-\alpha)\, U_\mu(x) + \alpha\, \Sigma_\mu(x)\,, \tag{3.37}$$

where α is the smearing parameter dictating the weighting between the link in question and its neighbours. $V_\mu(x)$ can be calculated for all links in the lattice simultaneously, thus allowing for a far greater degree of parallelisation than cooling. However, $V_\mu(x)$ is not necessarily in $SU(3)$. Hence it is necessary to project it back into $SU(3)$ via a projection operator $\mathcal{P}$ such that the new link $U'_\mu(x)$ is given by

$$U'_\mu(x) = \mathcal{P}[V_\mu(x)]\,. \tag{3.38}$$

Originally this projection was performed by iteratively maximising $\operatorname{Re}\operatorname{Tr} U'_\mu(x)\, V^\dagger_\mu(x)$ to select a new link, $U'_\mu(x)$. This is performed in a similar manner to the minimisation of the local action described in the previous section. In fact, if $\alpha = 1$ and the staples are blocked such that they are not updated simultaneously with $U_\mu(x)$, then we recover the cooling algorithm. This projection method shall be referred to as Max Re Tr reunitarisation.

We also consider employing an analytic projection method known as *unit circle projection* [93]. This is performed by first defining,

$$W_\mu(x) = V_\mu(x) \frac{1}{\sqrt{V^\dagger_\mu(x)\, V_\mu(x)}}\,. \tag{3.39}$$

This step ensures that the eigenvalues of $W_\mu(x)$ lie on the unit circle. The determinant is then fixed to obtain the new link,

$$U'_\mu(x) = \frac{1}{\sqrt[3]{\det W_\mu(x)}} W_\mu(x)\,. \tag{3.40}$$

The cube root has three possible solutions, so to remove ambiguity the solution satisfying $\arg \sqrt[3]{\det W_\mu(x)} \in (-\pi/3,\, \pi/3)$ is chosen. Unit circle projection is differentiable in the

matrix sense with respect to the initial link, $U_\mu(x)$, and is therefore suitable for use in situations where smoothness is an essential requirement.

Although analyticity is a desirable property for some use-cases, it presents a problem when considering the smoothing of vortex-only configurations. Recall that vortex-only configurations, $Z_\mu(x)$, are gauge-equivalent to $\mathbb{Z}_3$, meaning that there is a gauge transformation $\Omega(x)$ such that $\Omega(x)\, Z_\mu(x)\, \Omega^\dagger(x+\hat{\mu}) \in \mathbb{Z}_3$. Unit circle projection is gauge equivariant, meaning that if $U_\mu(x) \to U'_\mu(x)$, then $\Omega(x)\, U_\mu(x)\, \Omega^\dagger(x+\hat{\mu}) \to \Omega(x)\, U'_\mu(x)\, \Omega^\dagger(x+\hat{\mu})$. This means that for the purposes of unit circle projection, we need only consider $Z_\mu \in \mathbb{Z}_3$. In this case, unit circle projection results in APE smearing either not affecting a link, or switching its phase to one of the two other elements of $\mathbb{Z}_3$. This results in a spoiling of the vortex structure and thus renders APE smearing with unit circle projection inappropriate for use on vortex-only ensembles.

3.4.3 Stout-Link Smearing

The final smoothing technique used in this work is known as stout-link smearing [94]. Stout-link smearing seeks to remove the need for an $SU(3)$ projection operation by explicitly constructing an $SU(3)$ transformation from the staples that can then be applied to the original link. This is done by first defining,

$$T_\mu(x) = \Sigma_\mu(x)\, U_\mu^\dagger(x)\,. \tag{3.41}$$

$T_\mu(x)$ is then used to construct the traceless, Hermitian matrix,

$$Q_\mu(x) = \frac{i}{2}\left(T_\mu(x) - T_\mu^\dagger(x)\right) - \frac{1}{6}\operatorname{Tr}\left(T_\mu(x) - T_\mu^\dagger(x)\right)\,. \tag{3.42}$$

By construction, $Q_\mu(x) \in \mathfrak{su}(3)$, the Lie algebra of $SU(3)$ (see Appendix A.1) and hence may be exponentiated to obtain an element of $SU(3)$. Thus, the smeared link is defined as,

$$U'_\mu(x) = \exp(i\rho\, Q_\mu(x))\, U_\mu(x)\,, \tag{3.43}$$

where ρ is the smearing fraction parameter used to tune the stout-link smearing algorithm. We set $\rho = 0.06$ based on the results of Ref. [95].

It should be immediately noticed that stout-link smearing is completely unsuitable for use on VO configurations. Much like APE smearing, stout-link smearing is gauge equivariant, and thus we may treat the VO configurations as though every link belongs

to $\mathbb{Z}_3$. Thus, for these configurations $Q_\mu = 0$ and the smearing has no effect for any value of ρ.

Stout-link smearing may however be over-improved to provide excellent preservation of topological objects on the original configurations. Over-improved stout-link (OISL) smearing is performed by expanding the staples, $\Sigma_\mu(x)$, to include 2×1 rectangular terms (for an explicit description of these terms see Ref. [89]). Much like the Wilson action could be recovered from the staples as was shown in Eq. (3.36), the introduction of the rectangular terms allows for reconstruction of the Lüscher-Weisz action (Eq. (2.38)). A new parameter ϵ is introduced such that the action reconstructed from the staples interpolates between the Wilson and Lüscher-Weisz action. This allows for explicit tuning of the errors in the action to best preserve topological objects, as was done in Ref. [95]. This work found that a value of $\epsilon = -0.25$ optimally preserves lattice topology, and we therefore use this value herein.

3.4.4 Centrifuge Preconditioning

So far the general trend is that applying smoothing to vortex-only configurations is a tall order. The only method discussed so far that does not explicitly fail is APE smearing with non-analytic Max Re Tr reuniterisation. However, even this method has strict constraints on the smearing fraction, α, that require it to be greater than 1/3. If $\alpha < 1/3$, the APE smearing algorithm does not alter the vortex-only ensemble [89]. Even above this value, a large fraction of the links will not be affected. All these issues stem from the fact that VO ensembles are gauge-equivalent to ensembles that are proportional to the identity. It is therefore desirable to attempt to shift the vortex-only ensembles away from $\mathbb{Z}_3$ in a way that does not disrupt the structure of the vortex vacuum. This is the goal of *centrifuge preconditioning* [89].

The centrifuge smearing algorithm begins by considering the VO configurations in MCG, such that the links all belong to $\mathbb{Z}_3$. This means that the links may be written as

$$Z_\mu(x) = \begin{bmatrix} e^{i\lambda^1_\mu(x)} & 0 & 0 \\ 0 & e^{i\lambda^2_\mu(x)} & 0 \\ 0 & 0 & e^{i\lambda^3_\mu(x)} \end{bmatrix}, \tag{3.44}$$

where initially the $\lambda^i_\mu(x) = \lambda_\mu(x)$ are all equal for a given x. Using this notation, the 1×1 staple has phase $\sigma_\mu(x)$ given by,

$$\sigma_\mu(x) = \frac{1}{6} \sum_{\nu \neq \mu} \lambda_\nu(x) + \lambda_\mu(x + \hat{\nu}) - \lambda_\nu(x + \hat{\mu}) \\ -\lambda_\nu(x - \hat{\nu}) + \lambda_\mu(x - \hat{\nu}) + \lambda_\nu(x - \hat{\nu} + \hat{\mu}) \,. \tag{3.45}$$

A pair of indices, $(j, k) \in \{(1, 2), (2, 3), (3, 1)\}$, is then randomly selected. The phases of the original matrix phases are then updated to the new values given by,

$$\lambda'^j_\mu(x) = (1 - \omega)\, \lambda_\mu(x) + \omega\, \sigma_\mu(x) \tag{3.46}$$

$$\lambda'^k_\mu(x) = (1 - \omega)\, \lambda_\mu(x) - \omega\, \sigma_\mu(x) \,, \tag{3.47}$$

where ω is the centrifugal rotation angle. This procedure leaves the sum of the three phases invariant, and for sufficiently small ω the phase of the trace remains close to that of the original VO configuration. Thus we choose $\omega = 0.02$ as to introduce a slight perturbation away from $\mathbb{Z}_3$.

This allows us to finally apply smearing to vortex-only ensembles. First we precondition the ensemble with centrifuge precoditioning before applying APE smearing with Max Re Tr reuniterisation at $\alpha = 0.7$. This method, which is used wherever relevant in this work, ensures both an effective application of smearing and avoids any numerical singularities.

3.5 Summary

In this chapter we have described the core theory driving this research: the centre vortex model of QCD. We first presented a simple motivation for the vortex model in the context of the static quark potential, which is found to be confining when one considers an arrangement of randomly distributed percolating vortices. With this understanding developed, we described the process with which thin centre vortices are identified on the lattice. This is achieved through a transformation to maximal centre gauge followed by the process of centre projection. These centre projected vortices were connected to 3D slices of the lattice by defining the plaquette as in Eq. (3.15). This connection will prove essential for building our understanding of centre vortex structure in the coming chapters. We then presented the existing understanding

of centre vortices, highlighting their remarkable ability to reproduce the qualitative features of QCD, both in relation to confinement and $D\chi_{\mathrm{SB}}$.

Finally, we outlined the various lattice smoothing methods employed throughout this work, as they are utilised for a variety of purposes. Specifically, we described the issues associated with smoothing vortex-only configurations, and how these issues may be ameliorated by the use of centrifuge preconditioning followed by APE smearing with Max Re Tr projection. We also highlighted the importance of choosing the smoothing link combination appropriately such that topological objects are preserved. This now places us in a position to present the first set of results from this research, centering around novel visualisations of centre vortices in $SU(3)$ gauge theory and their relationship to topological charge density.

Chapter 4

The Pure Gauge Picture

This chapter is based on the paper "Visualisation of Centre Vortex Structure", Biddle, Kamleh, and Leinweber [21].

In the previous chapter we observed how the structure of centre vortices plays a significant role in their ability to generate confinement. The fact that one of the defining features of the vortex model is tied so intimately to the geometry of vortices in the vacuum indicates that visualising these structures may provide valuable insight [96, 97]. To this end, we construct visualisations of centre vortices and topological charge density on the lattice. We then use these visualisations to investigate the dynamics of the vortex model in an interactive and novel manner.

We begin this chapter in Sec. 4.1, where we describe in detail our convention for plotting vortices in three dimensional space, and present the first visualisations of centre vortices on the lattice. As projected centre vortices are inherently two dimensional objects embedded in four dimensions, we describe the technique used to capture the behaviour of vortices in the fourth dimension in Sec. 4.2. In Sec. 4.3 we present visualisations of topological charge density alongside centre vortices. In Secs. 4.3.2 and 4.3.3 we describe the relationship between topological charge and two types of vortex structures, namely singular points and branching points. Finally, in Sec. 4.3.4 we investigate the correlation these structures have with topological charge density obtained from smoothed lattice configurations. This investigation lays the groundwork for the development of further visualisation techniques, and emphasises the importance of centre-vortex geometry in a full understanding of the QCD vacuum.

A number of the visualisations presented in this chapter have interactive versions that can be found in the supplementary material of Ref. [21]. Details for interacting

with these models can also be found in this paper. Interactive models that can be found in this material will be marked as **Interactive** in the figure caption.

4.1 Spatially-Oriented Vortices

4.1.1 Visualisation Conventions

For this chapter we will utilise the $20^3 \times 40$ pure gauge lattices described in Table 2.1. As the lattice is a four-dimensional hypercube, we visualise the centre vortices on a set of 3D slices. The choice of dimension to take slices along is irrelevant at low temperature in Euclidean space where our lattice calculations take place, so to maximise the volume of each slice we introduce a coordinate system with the z axis along the long dimension, and take slices along the t axis. This results in $N_t = 20$ slices each with dimensions $N_x \times N_y \times N_z = 20 \times 20 \times 40$. Within each slice we can visualise all vortices associated with an x–y, x–z or y–z spatial plaquette by calculating $P_{x\,y}(\mathbf{x})$, $P_{y\,z}(\mathbf{x})$ and $P_{z\,x}(\mathbf{x})$ for all $\mathbf{x}$ in the slice. These vortices will be referred to as the 'spatially-oriented' vortices, as they are fixed in time.

We can connect this to the form of vortex-only plaquette presented in Eq. (3.15). Setting $\lambda = 4$ which thereby restricts the remaining indices to take values $i, j, k \in \{1, 2, 3\}$, we have

$$P_{ij} = \exp\left(\frac{\pi i}{3}\,\epsilon_{ijk}\,m_k(\bar{x})\right) . \tag{4.1}$$

We interpret Eq. (4.1) for nontrivial values of m_k to indicate a vortex penetrating the plaquette lying in the $\hat{\imath}$–$\hat{\jmath}$ plane in the $\pm\hat{k}$ direction. We render vortices according to the value their centre charge. For a charge $m_k = +1$ vortex, a blue jet is plotted piercing the centre of the plaquette, and for a charge $m_k = -1$ vortex, a red jet is plotted. The direction of the jet is set according to the right-hand rule of the epsilon tensor, such that

- $P_{x\,y} = \pm 1 \implies \pm\hat{z}$ direction.
- $P_{y\,z} = \pm 1 \implies \pm\hat{x}$ direction.
- $P_{z\,x} = \pm 1 \implies \pm\hat{y}$ direction,

An example of this plotting convention is shown in Fig. 4.1. As the jet direction $\pm\hat{k}$ is aligned with the sign of the centre charge $m_k = \pm 1$ the vortex lines show the oriented flow of positive unit centre charge ($m = +1$).

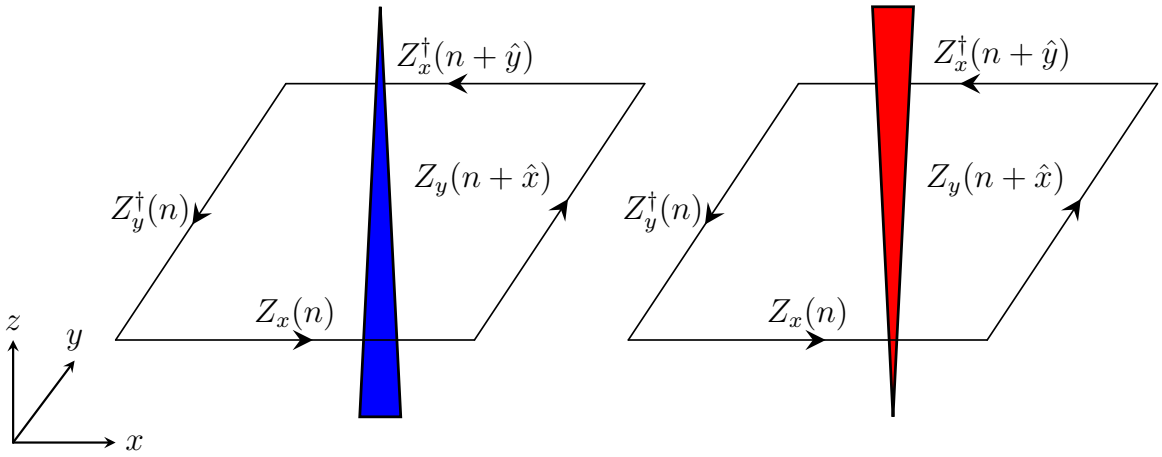

Fig. 4.1 An example of the plotting convention for vortices located within a 3D time slice. **Left:** A $+1$ vortex in the $+\hat{z}$ direction. **Right:** A -1 vortex in the $-\hat{z}$ direction.

Projected centre vortices are surfaces in four dimensional space-time, analogous to the centre line of a vortex in fluid dynamics that maps out a surface as it moves through time. Note that, as is conventional, herein "time" simply refers to the fourth spatial dimension on the Euclidean lattice. Similarly, "time evolution" refers to change with respect to the fourth spatial dimension, that is, variation in Euclidean time (not real time). In this way, the visualisations presented here can be simply thought of as a way to interpret the four-dimensional geometry. As the surface cuts through the three-dimensional spatial volume of our visualisation, a P-vortex line is rendered mapping the flow of centre charge.

The spatially-oriented vortices for the 3D slices with $t = 1, 2$ are illustrated in Figs. 4.2, 4.3. At first glance the vortex structure appears highly complex, and it is difficult to identify the significant features. As such, we make use of the 3D models to hone in and isolate the important features present in these slices. We present some of these features in Fig. 4.4. We observe that the vortices do indeed form closed lines (as required by the Bianchi identity), highlighted in the middle panel of Fig. 4.4. We also see that the vortex loops tend to be large. This agrees with the determination made of $SU(2)$ vortices in Refs. [8, 63]. We find for this ensemble that the physical vortex density is $\rho_V = 2.060(7)$ fm^{-2}, as determined by Eq. (3.28).

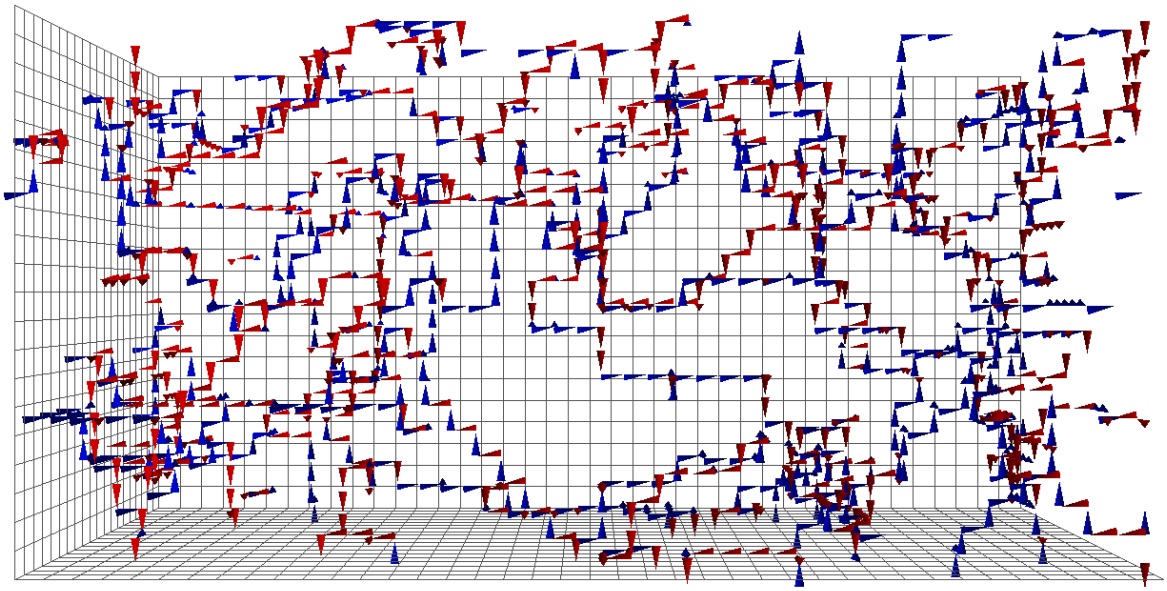

Fig. 4.2 The $t = 1$ slice with all spatially-oriented vortices plotted. The flow of $m = +1$ centre charge is illustrated by the jets as described in the text. (**Interactive**)

4.1.2 Branching/Monopole Points

The presence of branching points is of particular interest, as previous studies have primarily focussed on $SU(2)$ theory which is free from these structures. In $SU(3)$ it is possible to conserve centre flux at the intersection of 3, 5 or 6 vortex lines within a 3D slice, as discussed in Section 3.3.1. An example of a branching point in our visualisations is shown in the right panel of Fig. 4.4. In Fig. 4.5 we identify all points with $n_{\text{cube}}(x \,|\, \hat{\mu}) > 2$ present in the $t = 1$ time slice and display them as coloured spheres.

As described in Section 3.3.1, we define $n_{\text{cube}}(x \,|\, \hat{\mu})$ to count the number of vortices piercing an elementary cube when the lattice is sliced along the $\hat{\mu}$ direction. The distribution of $n_{\text{cube}}(x \,|\, \hat{\mu})$ over our ensemble is shown in Fig. 4.6. As required, we observe that $n_{\text{cube}}(x \,|\, \hat{\mu}) = 1$ points are not present. We also see that larger values of $n_{\text{cube}}(x \,|\, \hat{\mu})$ become increasingly uncommon, with $n_{\text{cube}}(x \,|\, \hat{\mu}) = 6$ points making up just a tiny fraction of overall branching points. Thus, despite there being an ambiguity around their assignment as branching points, the choise to include or exclude them makes little difference. The fact that branching points are only well defined on 3D slices can be understood by considering the implication of a branching into the fourth

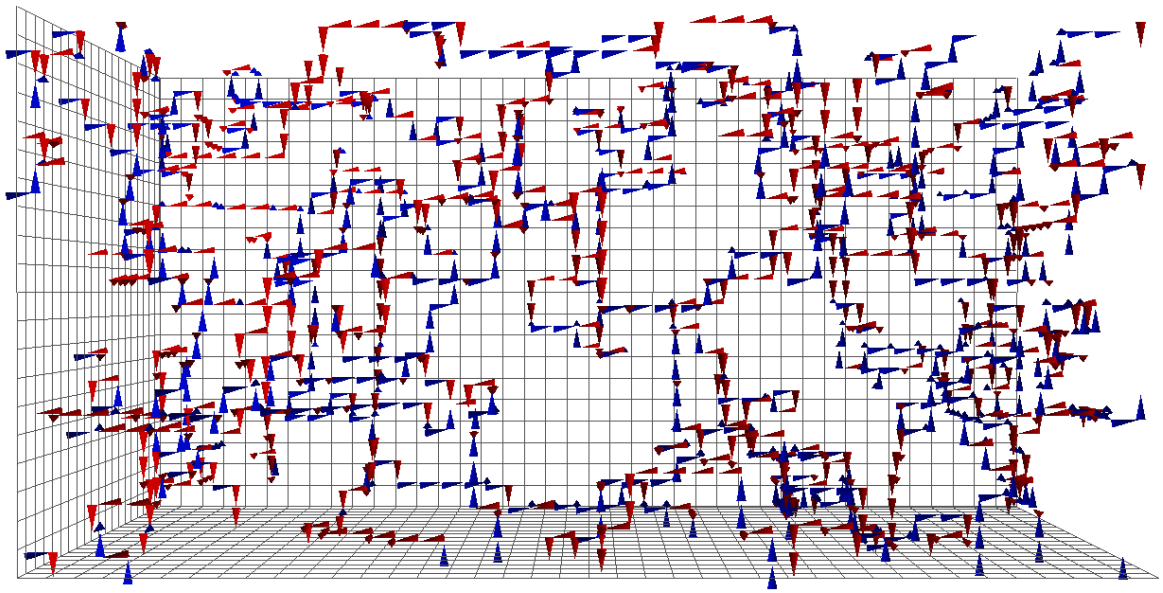

Fig. 4.3 The $t = 2$ slice with all spatially-oriented vortices plotted. Only a small subset of jets are stationary between $t = 1$ and $t = 2$. Symbols are as in Fig. 4.2. (**Interactive**)

dimension. In this case one would observe two vortex jets emerging from or converging into a 3D cube. However, this situation does not occur in our visualisations as is required for conservation of flux lines.

It is clear from our visualisations and the data in Fig. 4.6 that branching points occur frequently in the confining phase, with an average of 109.8(6) branching points per 3D slice. This corresponds to a physical density of $\rho_{\mathrm{BP}} = 3.51(2)\,\mathrm{fm}^{-3}$, as calculated via Eq. 3.31. Work presented in Refs. [13, 67] confirms that indeed the branching point density possesses the correct scaling behaviour over different values of β governing the lattice spacing such that ρ_{BP} may be considered a physical quantity. Further discussion of branching points and their relationship with topological charge is presented in Sec. 4.3.3.

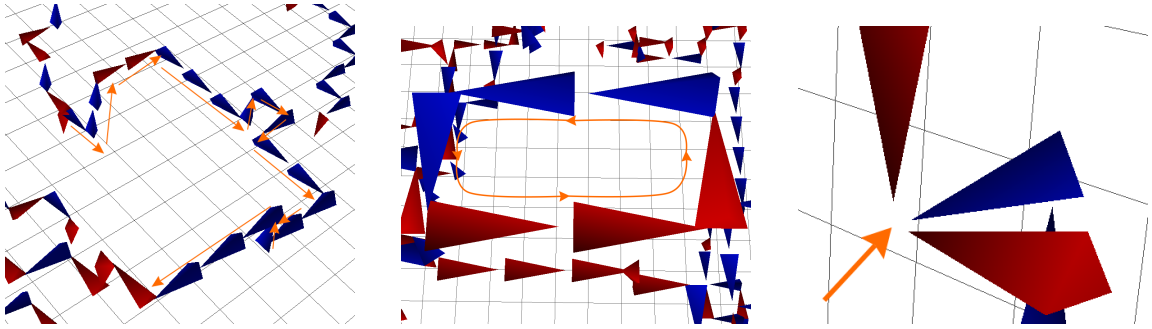

Fig. 4.4 **Left:** Vortices form directed continuous lines, highlighted with orange arrows in this diagram. Note that because of the lattice periodicity, these lines may wrap around to the opposite edge of the lattice. **Middle:** Vortices must form closed loops to conserve the vortex flux. **Right:** $SU(3)$ vortices are capable of forming monopoles or branching points where three or five vortices emerge or converge at a single point.

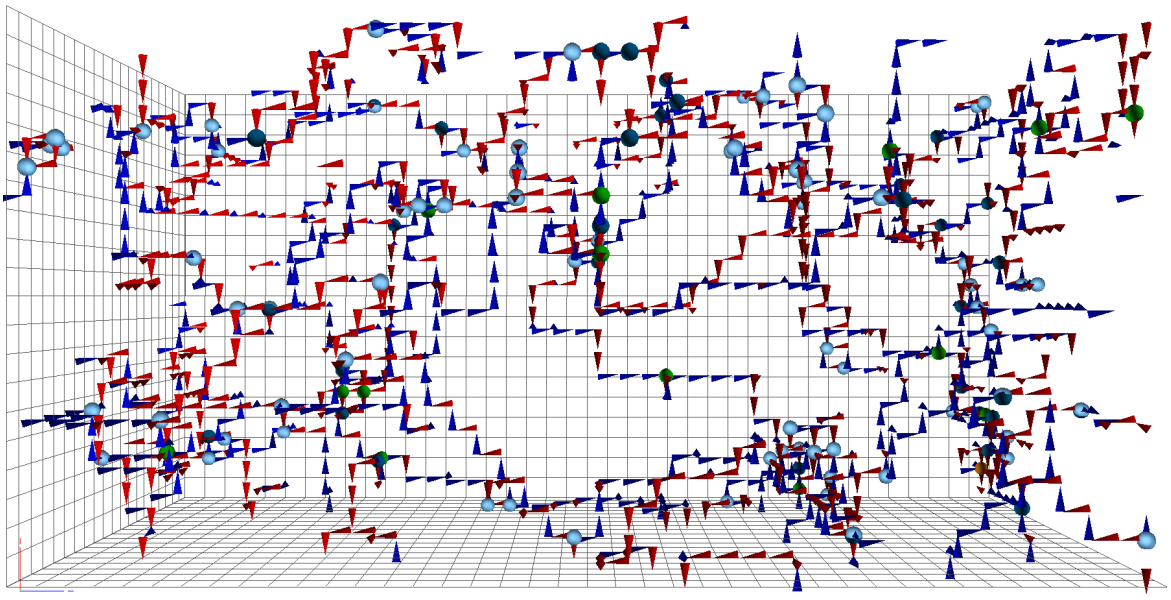

Fig. 4.5 Points with two or more vortices piercing a 3D cube are shown on the $t = 1$ time slice. The number of vortices piercing a cube is denoted by the colour: blue = 3, green = 4, orange = 5, red = 6. Whilst there are no red points present in this slice, they occur rarely on other slices. (**Interactive**)

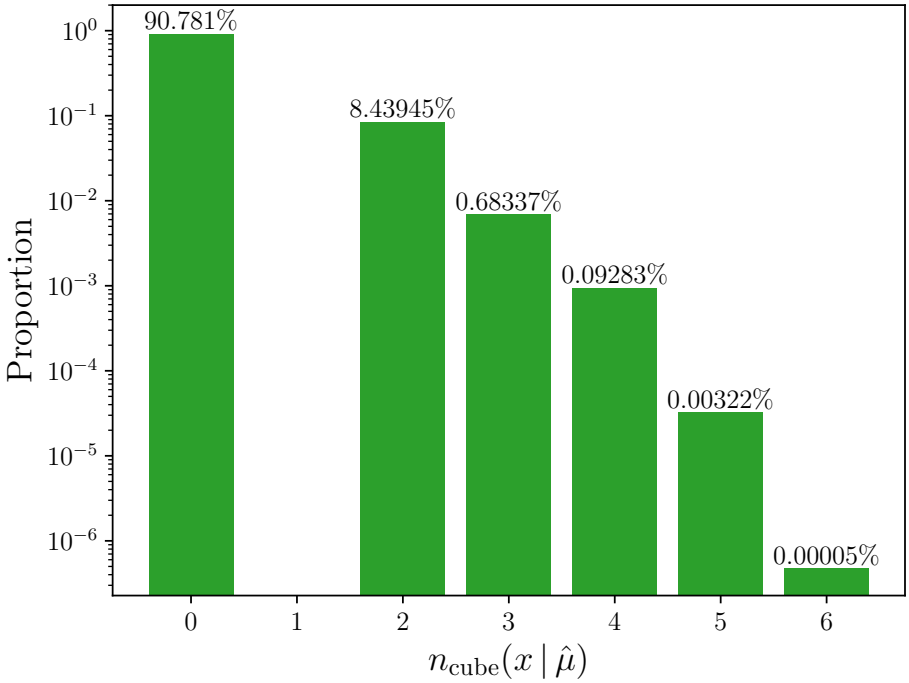

Fig. 4.6 The ensemble average of the number of vortices piercing each 3D cube. As it is necessary to preserve continuity of the vortex flux, we see that there are no cubes with one vortex piercing them. The largest vortex contribution is from $n_{\text{cube}} = 2$, arising from vortices propagating without branching or touching. We also see that $n_{\text{cube}} = 3$ branching points dominate the $n_{\text{cube}} = 5$ branching points.

4.2 Space-Time Oriented Vortices

For each link in a given 3D slice there are two additional plaquettes that lie in the x_i–t plane, pointing in the positive and negative time directions. Vortices associated with space-time oriented plaquettes contain information about the way the line-like vortices evolve with time, or equivalently, how the vortex surfaces appear in four dimensions.

In a given 3D slice we only have access to one link associated with a space-time oriented vortex, and as such we plot an arrow along this link to indicate its association with this vortex. Considering the four-dimensional Levi-Cevita tensor, we adopt the following plotting convention for these space-time oriented vortices:

$+1$ vortex, forward in time, $\implies$ cyan arrow, positively oriented,

$+1$ vortex, backward in time, $\implies$ cyan arrow, negatively oriented,

-1 vortex, forward in time, $\implies$ orange arrow, positively oriented,

-1 vortex, backward in time, $\implies$ orange arrow, negatively oriented.

These conventions are shown diagrammatically in Fig. 4.7. Utilising these conventions, the first time slice now contains temporal information as highlighted in Fig. 4.8. The full 3D models are difficult to interpret as a 2D image and a therefore omitted from this presentation, however the interactive 3D models for the first two time slices are available in the supplementary material of Ref. [21].

As we step through time, we expect to see the positively oriented space-time vortex indicator links retain their colour but swap direction as they transition from being forwards in time to backwards in time, as shown in Fig. 4.9.

The space-time oriented indicator links act as predictors of vortex line motion between slices. The simplest case of vortex motion is shown diagrammatically in Fig. 4.10. The shaded red plaquettes indicate the location of a spatially-oriented vortex which would be plotted in the suppressed $\hat{x}$ direction, and the red line demonstrates how the centre charge pierces between the two time slices. This figure demonstrates a spatially-oriented vortex shifting one lattice spacing in the $\hat{y}$ direction between time slices. For a vortex located at x and pointing in the $\pm\hat{x}$ direction, this motion will be indicated by an orange indicator link on the $Z_z(x + \hat{y})$ link. Thus we see that spatially-oriented vortices move in a direction perpendicular to both the jet and the indicator link.

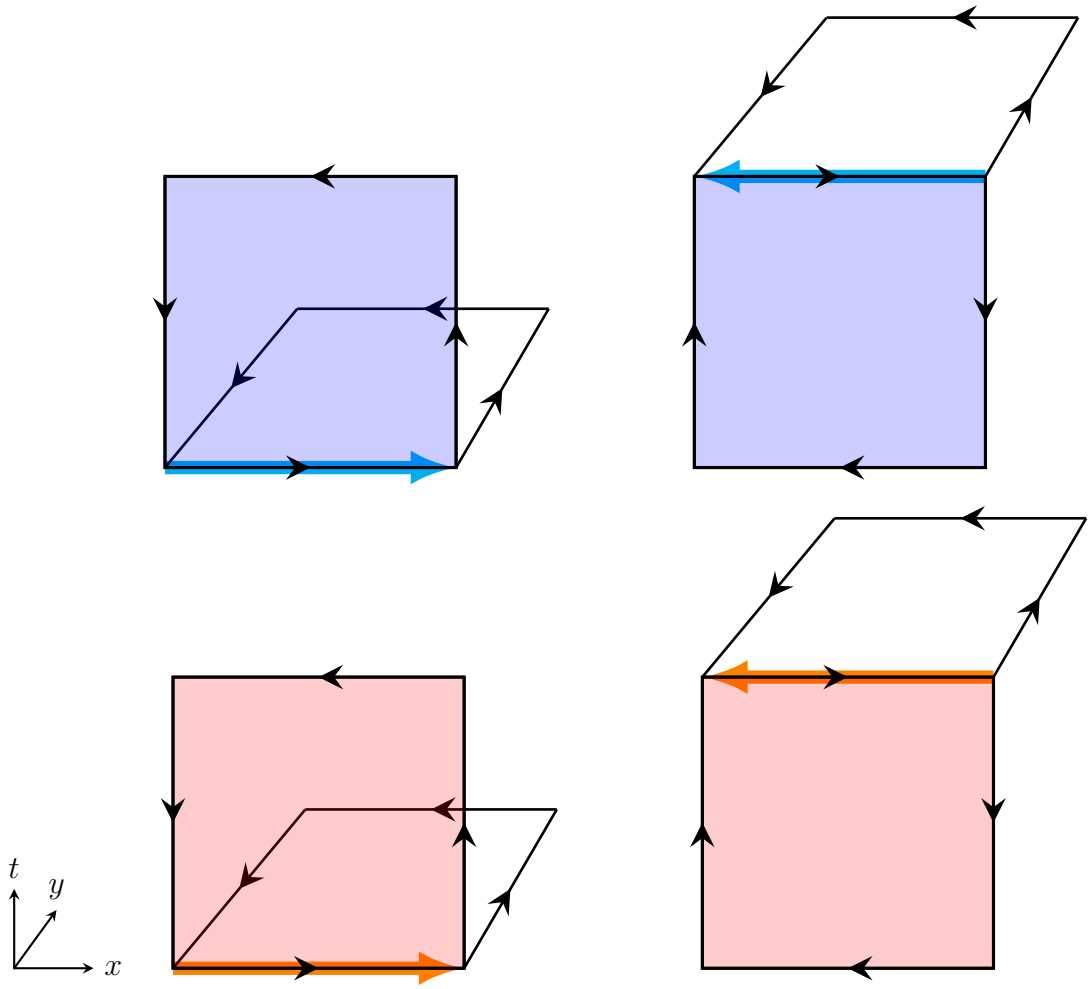

Fig. 4.7 **Top:** A +1 vortex in the forward (left)/backward (right) x–t plane (shaded blue) will be plotted as a cyan arrow in the $\pm\hat{x}$ direction respectively. **Bottom:** A −1 vortex in the forward (left)/backward (right) x–t plane (shaded red) will be plotted as an orange arrow in the $\pm\hat{x}$ direction respectively.

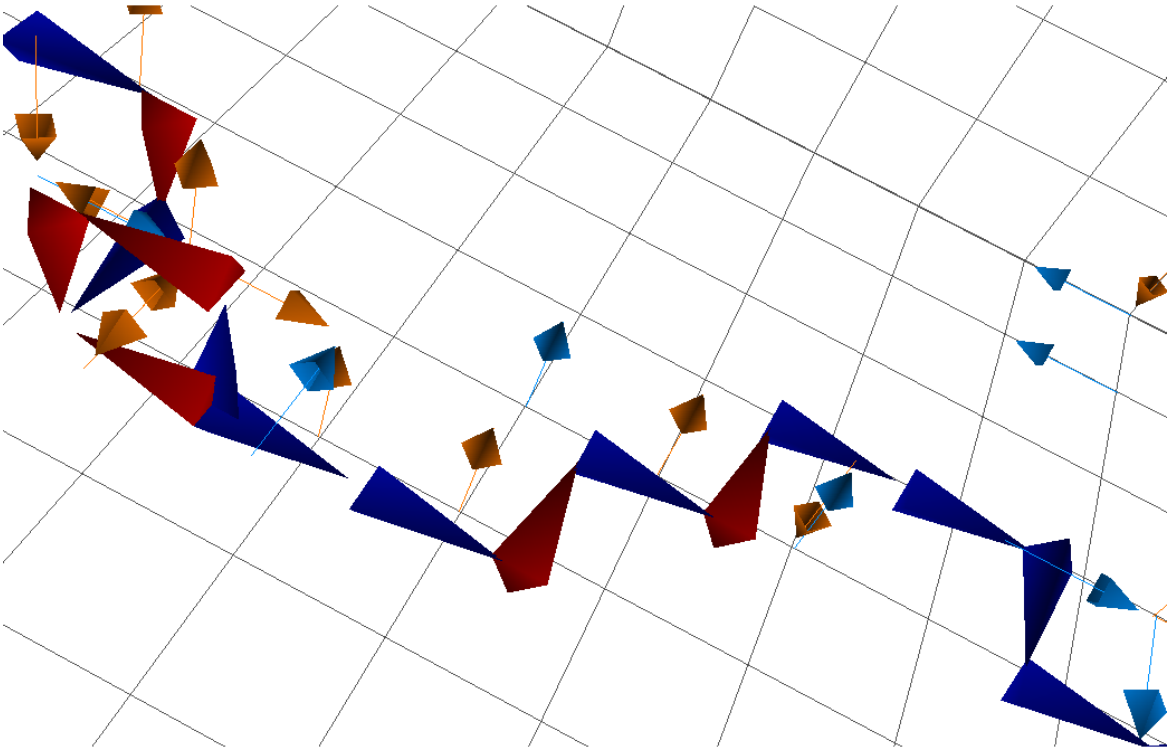

Fig. 4.8 On the $t = 1$ time slice, the flow of $m = +1$ centre charge is illustrated by the jets, and the spatial links indicate the presence of centre vortices in the suppressed time direction. These indicator links show how the jets will evolve through the suppressed Euclidean time direction. Rendering conventions are described in the text.

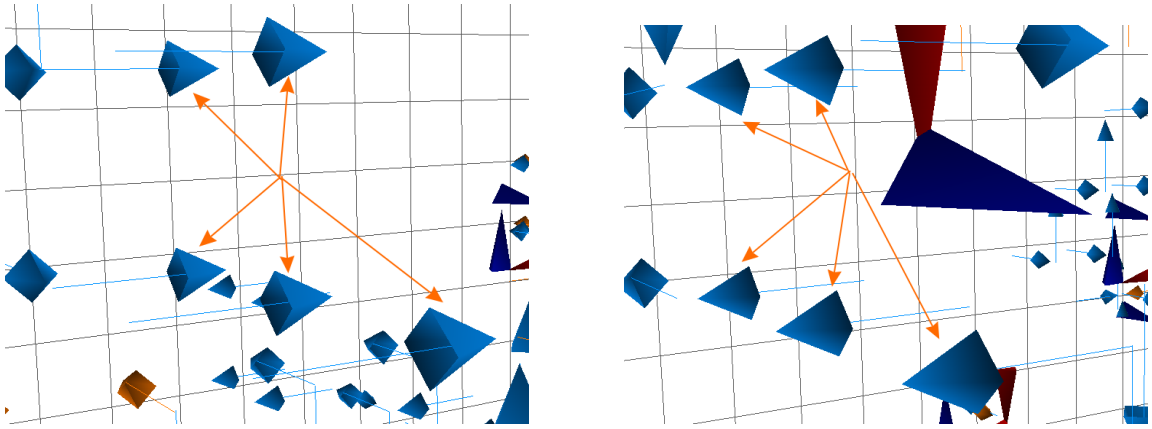

(a) $t = 1$ (b) $t = 2$

Fig. 4.9 Space-time oriented vortices changing as we step through time. We observe the space-time indicator links change direction, however the phase (colour) of the vortex remains the same.

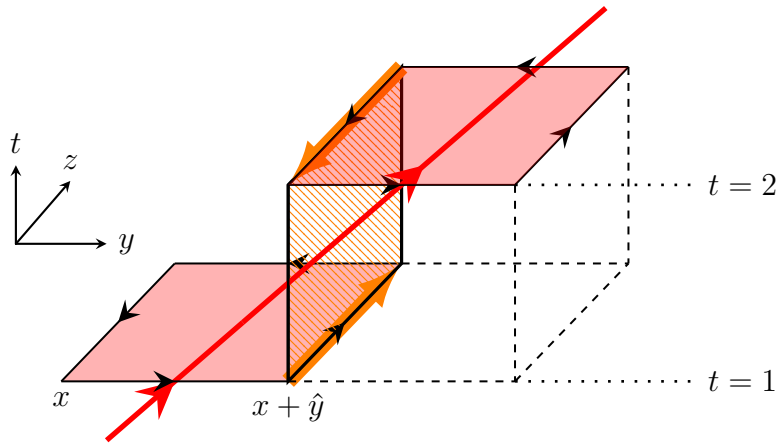

Fig. 4.10 An example of a spatially-oriented vortex at the space-time coordinate x moving one plaquette between time-slices. The solid red line indicates how the flow of vortex charge pierces between time slices. By our visualisation conventions, the shaded red plaquettes would have a spatially-oriented jet plotted in the suppressed $\hat{x}$ direction. Space-time vortices are illustrated by the orange indicator links belonging to the space-time plaquette. We observe that spatially-oriented vortices move in the time direction (hidden in our 3D models), perpendicular to the indicator link.

To see this predictive power in action, consider Fig. 4.11. Here we see in Fig. 4.11a a line of three $m = +1$ spatially-oriented vortices each with an associated $m = -1$ space-time oriented vortex below them. As we step to $t = 2$ in Fig. 4.11b we observe the space-time oriented arrows change direction, and the spatially-oriented vortex line shifts one lattice spacing down in the direction perpendicular to the indicator links, such that the space-time oriented vortices are now above them.

Another example of space-time oriented vortices predicting the motion of spatially-oriented vortex lines is shown in Fig. 4.12. In Fig. 4.12a, we observe a line of four $m = -1$ (red) spatially-oriented vortices with no space-time oriented links associated with them, indicating that this line should remain fixed as we step through time. Alternatively, towards the top of the red line we observe a branching point with two associated -1 space-time indicator arrows. The forward-oriented arrow indicates that this branching point will move. That is, the sheet piercing the $t = 1$ slice is generating non-trivial space-time vortices as it proceeds to pierce the $t = 2$ slice. Observing the same region at $t = 2$ in Fig. 4.12b, we see that this is precisely what occurs. The vortex line has remained fixed, whereas the branching point has shifted.

The cases presented in Fig. 4.11 and Fig. 4.12 are ideal, where the spatially-oriented vortex lines shift only one lattice spacing between time slices. However, it is frequently the case where the spatially-oriented vortices shift multiple lattice spacings per time

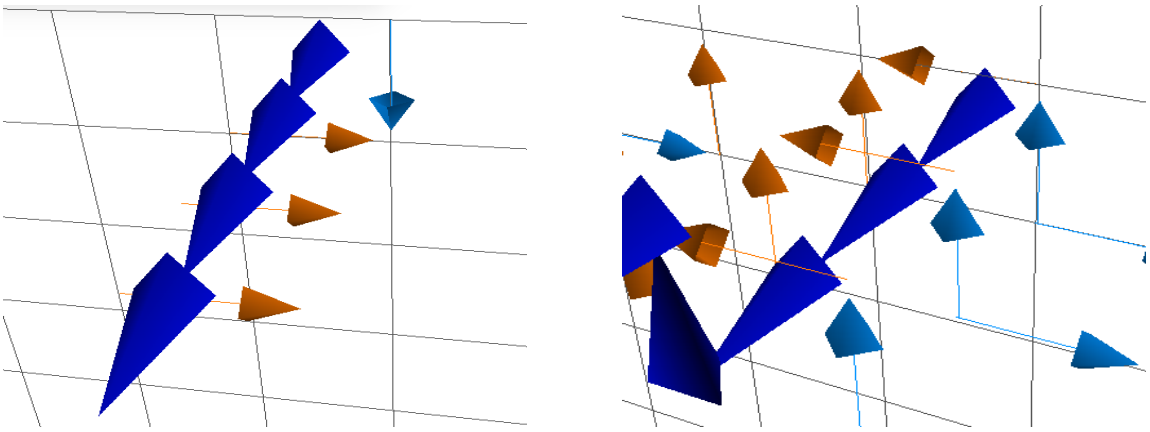

(a) $t = 1$ (b) $t = 2$

Fig. 4.11 An example of space-time oriented vortices predicting the motion of the spatially-oriented vortices. Here we see the $m = +1$ (blue) vortex line transition one lattice spacing down as we step from $t = 1$ to $t = 2$. Note that the orange space-time vortex indicator links have changed direction.

step, as demonstrated in Fig. 4.13. In Fig. 4.13a, we observe a large sheet of space-time oriented vortices with a line of spatially oriented vortices above them. As we transition to $t = 2$ in Fig. 4.13b, the line is carried along the sheet and now appears at the bottom.

To see how this occurs diagrammatically, consider Fig. 4.14. The conventions in this figure are the same as in Fig. 4.10. Within each slice we would observe the space-time oriented links shown, however the spatially-oriented vortex appears to move three plaquettes in one time step. These multiple transitions make it difficult to track the motion of vortices between time slices. However, the space-time oriented vortices remain a useful tool for understanding how centre vortices evolve with time. Note that if a spatially-oriented vortex has no associated space-time oriented vortices then it is guaranteed to remain stationary. In this respect, the lack of space-time oriented vortices is also a valuable indicator of vortex behaviour.

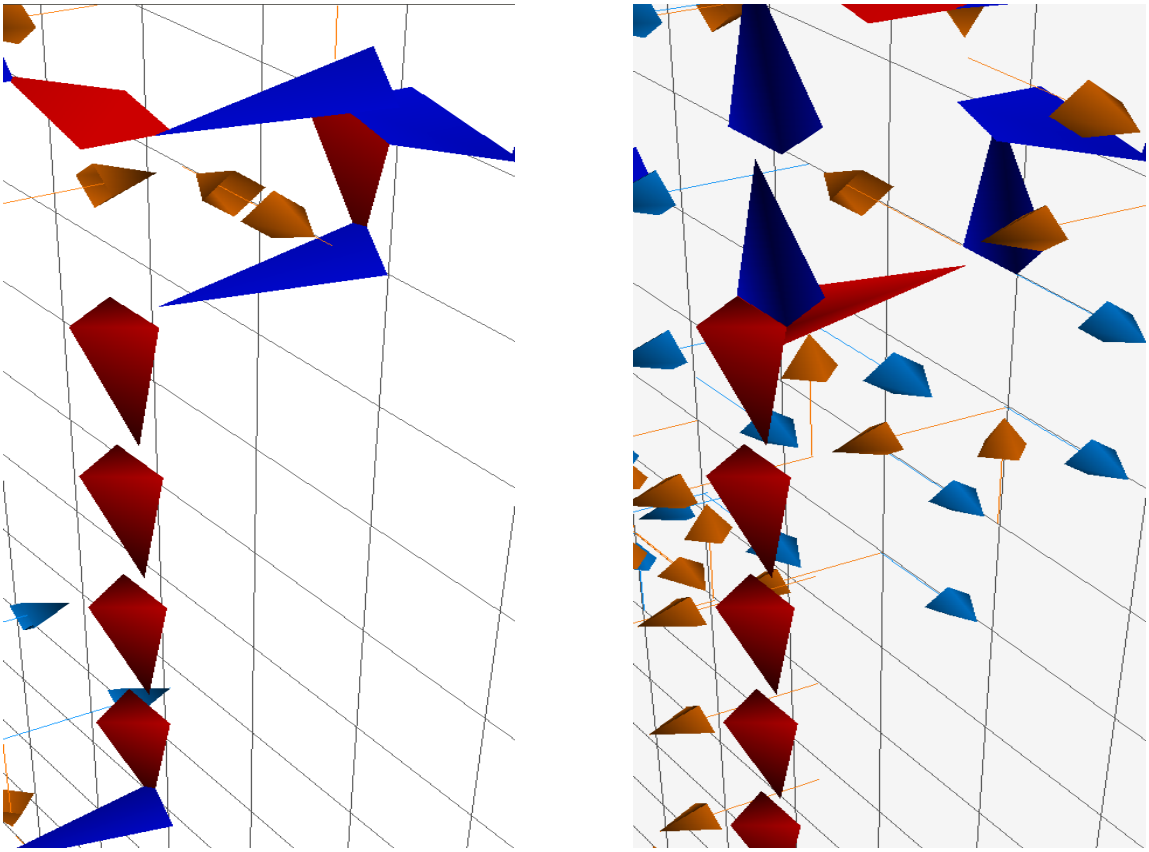

(a) $t = 1$ (b) $t = 2$

Fig. 4.12 An second example of space-time oriented vortices predicting the motion of the spatially-oriented vortices. We observe the -1 (red) vortex line with no associated space-time vortex indicator links remains stationary as we transition from $t = 1$ to $t = 2$. However, the branching point with associated space-time vortex indicator link moves down and to the left during the transition.

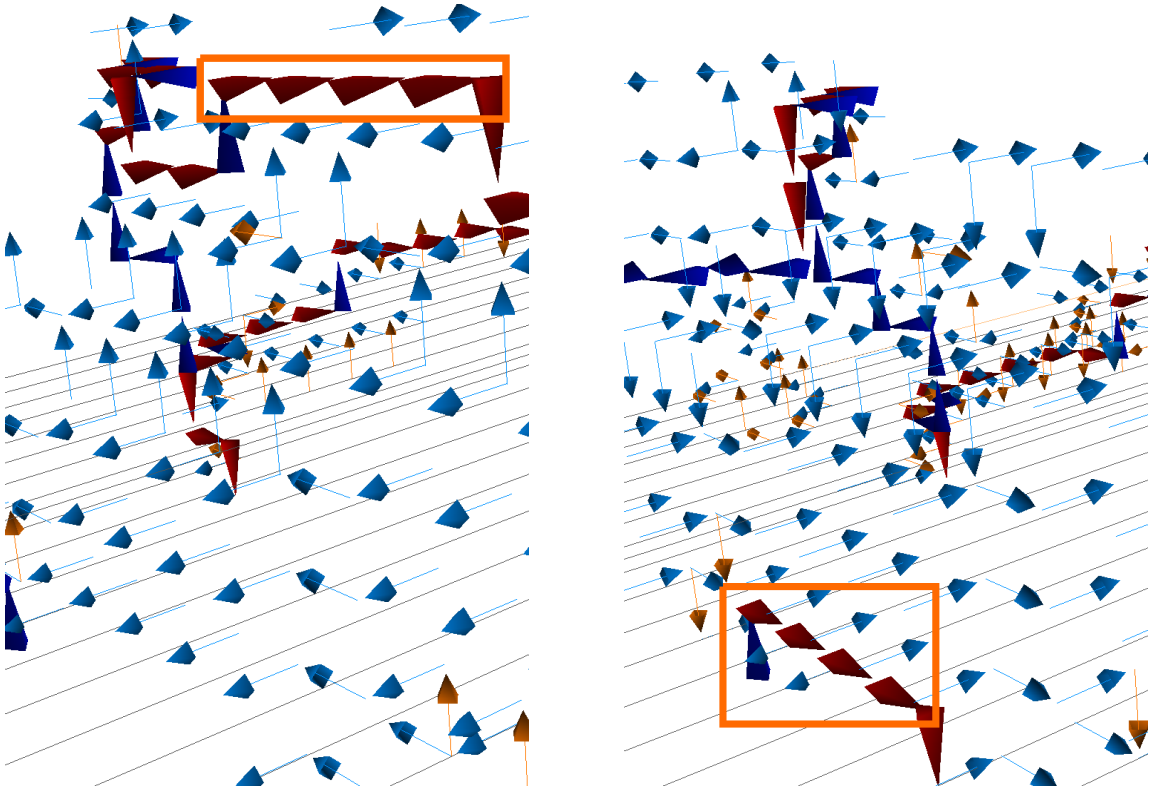

(a) $t = 1$ (b) $t = 2$

Fig. 4.13 An example of a sheet of space-time oriented vortices predicting the motion of spatially-oriented vortices over multiple lattice sites from $t = 1$ to $t = 2$. The highlighted line of red vortices flows along the sheet of cyan time-oriented indicator links.

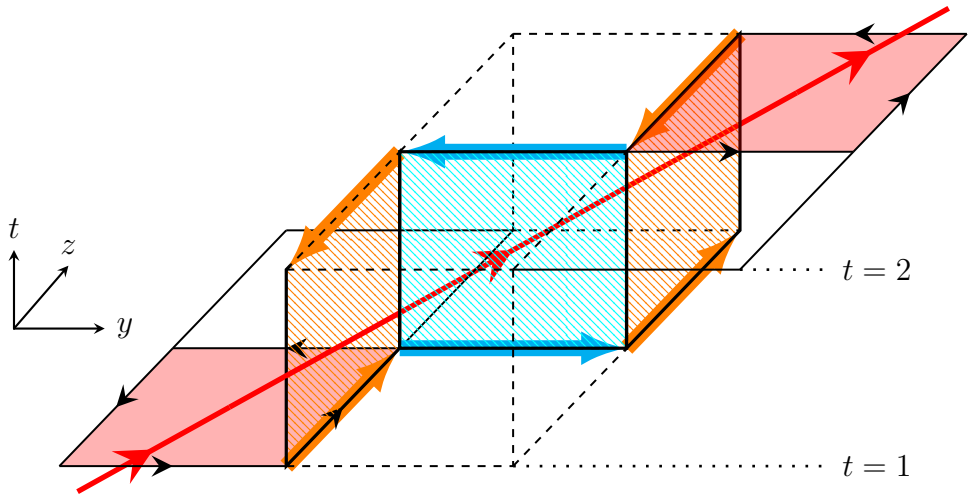

Fig. 4.14 A demonstration of how spatially-oriented vortices can transition multiple lattice spacings in a single time step. Conventions are the same as in Fig. 4.10

4.3 Centre Vortices and Topological Charge

We now wish to explore the relationship between centre vortices and topological charge. This relationship can be examined in terms of not only the vortices themselves, but the substructures present in the vortex vacuum. We begin this section by first defining topological charge and its relationship to centre vortices. We then describe singular points and branching points in the context of generating topological charge, before finally considering the correlations between vortex structures and topological charge obtained from configurations that have undergone gauge field smoothing.

4.3.1 Topological Charge

The non-trivial ground state of QCD is associated with different vacua that are not related to one another via a gauge transformation. Topological charge serves to enumerate these distinct vacuum states, and therefore in the continuum will take integer values. In the continuum, the topological charge, Q, is calculated as [98]

$$Q = \int d^4x \frac{1}{16\pi^2} \epsilon_{\mu\nu\rho\sigma} \operatorname{Tr}(F_{\mu\nu} F_{\rho\sigma}) \tag{4.2}$$

One may also consider the topological charge density, $q(x)$, defined as the integrand of Eq. (4.2),

$$q(x) = \frac{1}{32\pi^2} \epsilon^{\mu\nu\rho\sigma} \operatorname{Tr}\left(F_{\mu\nu}(x) F_{\rho\sigma}(x)\right) . \tag{4.3}$$

Topological charge density is not uniformly distributed, and instead clumps into regions of high density, known as instantons. It is therefore of interest to observe whether regions of high topological charge density are correlated with the presence of centre vortices.

To calculate the topological charge density on the lattice, it is common to make use of the clover definition of $F_{\mu\nu}$ presented in Eq. (2.36). As with the lattice actions discussed in Chapter 2, it is possible to further systematically improve upon the topological charge definition by addition of terms with higher orders of the lattice spacing. This is done by the additional inclusion of (2×2), $(1 \times 2) + (2 \times 1)$, $(1 \times 3) + (3 \times 1)$ and

(3×3) clover loop combinations to form the 5-loop improved topological charge [99]

$$\begin{aligned} F_{\mu\nu}^{5-\text{loop}} = &- \frac{23}{36} F_{\mu\nu}^{(1\times1)} - \frac{139}{180} F_{\mu\nu}^{(2\times2)} \\ &+ \frac{112}{45} F_{\mu\nu}^{(1\times2)+(2\times1)} - \frac{7}{20} F_{\mu\nu}^{(1\times3)+(3\times1)} \\ &+ \frac{1}{20} F_{\mu\nu}^{(3\times3)} \,. \end{aligned} \tag{4.4}$$

This definition of the topological charge density has been shown to provide better convergence to integer values of the total topological charge [90]. In this chapter we make use of the simple 1×1 topological charge definition when analysing centre-projected configurations, as the gauge link information is highly localised around the projected vortex locations. However, for the original and smoothed configurations we instead employ the 5-loop improved definition.

We calculate the topological charge density on an original lattice configuration after eight sweeps of three-loop $\mathcal{O}(a^4)$-improved cooling [90] (see Section 3.4.1). This smoothing is necessary to remove short-range fluctuations and associated large perturbative renormalisations, but is a sufficiently low number of sweeps so as to minimally perturb the configuration. Topological charge density obtained after minimal over-improved stout-link smearing is explored in Sec. 4.3.4.

We plot regions of positive topological charge density in yellow, and regions of negative topological charge density in blue, with a colour gradient to indicate the magnitude. Only topological charge density of sufficient magnitude is plotted to better emphasise regions of significance. Overlaying the topological charge density visualisation onto our previous 3D models, we obtain the visualisation shown in Fig. 4.15.

Under centre projection the topological charge changes notably, as might be expected for a local operator. Fig. 4.16 shows a histogram of the total topological charge Q across the ensemble obtained with the gluonic definition after 5 sweeps of over-improved stout-link smearing. This is compared to Q obtained from the projected configurations, calculated via the singular points defined in Section 4.3.2. Clearly, the topological charge is not preserved. We also check in panel (c) of Fig. 4.16 whether the relative sign of the topological charge calculated on each configuration is the same. Here we also observe little correlation in the relative sign.

Observing the percolation of non-trivial centre vortices in the context of topological charge density provides new insight into the instability of instanton-like objects to centre-vortex removal [17]. We can quantitatively evaluate the correlation between the

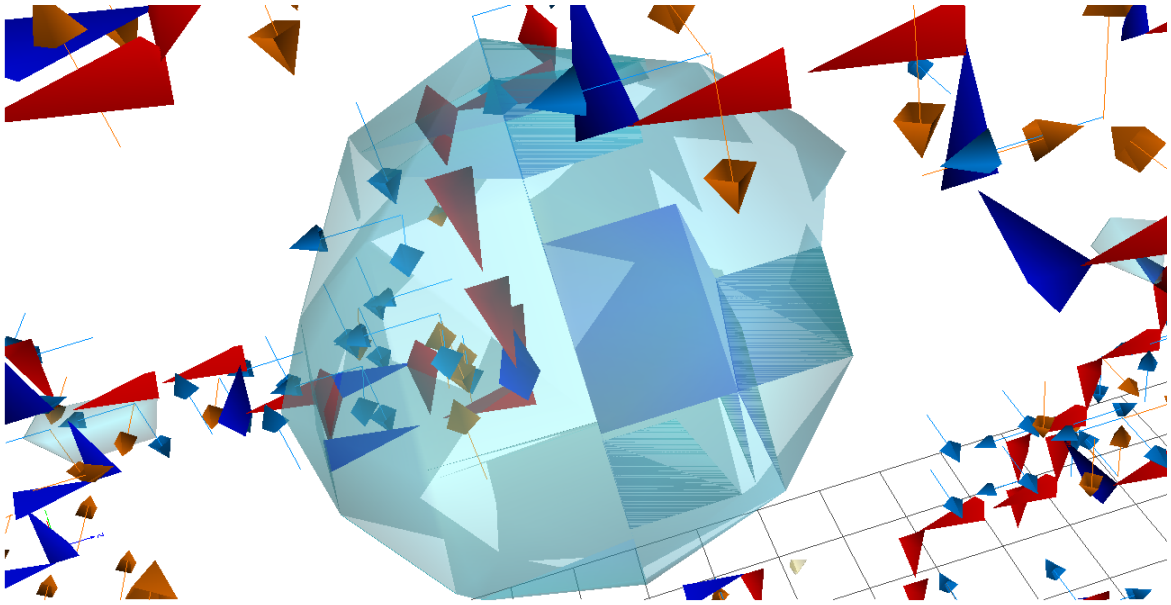

Fig. 4.15 Regions of high topological charge density are rendered as translucent blue ($q(x) < 0$) and yellow ($q(x) > 0$) volumes, overlaying the $t = 1$ slice.

locations of centre vortices and the regions of significant topological charge density obtained from the vortex-only configurations by using the measure

$$C = V \frac{\sum_x |q(x)|\, L(x)}{\sum_x |q(x)| \sum_x L(x)} - 1\,, \tag{4.5}$$

where V is the lattice volume, and

$$L(x) = \begin{cases} 1\,, & \text{Vortex associated with any} \\ & \text{plaquette touching } x, \\ 0\,, & \text{Otherwise,} \end{cases} \tag{4.6}$$

contains information from the full 4D volume. This method of constructing $L(x)$ allows for a single vortex to result in multiple non-zero $L(x)$ locations. However, $L(x)$ is defined in this way so that vortex information associated with plaquettes is shifted to the regular lattice, allowing it to be compared with the topological charge density. A value of $C = 0$ indicates no correlation. $C < 0$ and $C > 0$ indicate anti-correlation or correlation respectively.

We can also compare the results of this calculation to the maximally correlated value for C, which can be obtained by postulating that all x for which $L(x) = 1$ correlate to the $\sum_x L(x)$ highest values of $|q(x)|$, denoted $|q_i|$. As we are assuming

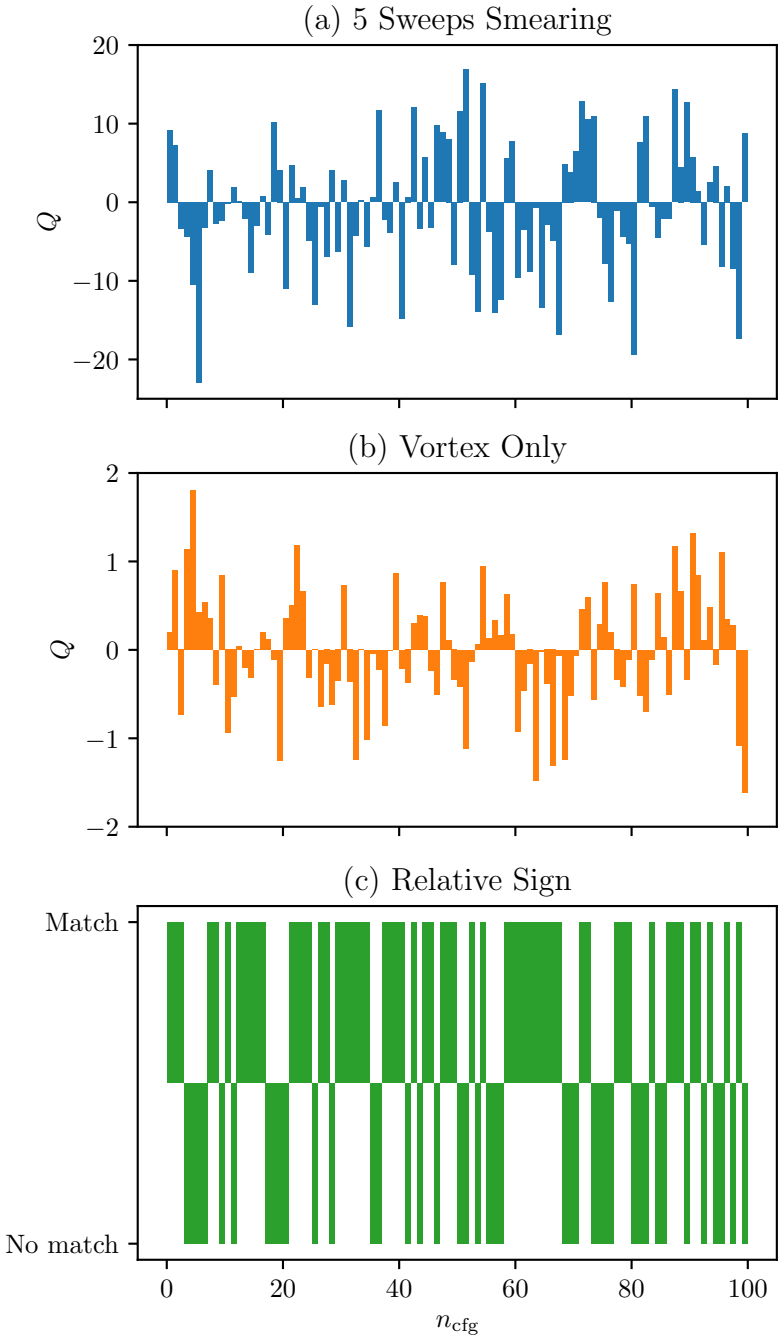

Fig. 4.16 A histogram of total topological charge Q (a) using the gluonic definition after 5 sweeps of over-improved stout-link smearing and (b) direct centre projection from the original gauge fields. It is apparent that singular points following centre projection do not preserve the total topological charge (note also the scale change between (a) and (b)). Panel (c) shows whether the sign matches between plots (a) and (b); again it is apparent that there is little correlation.

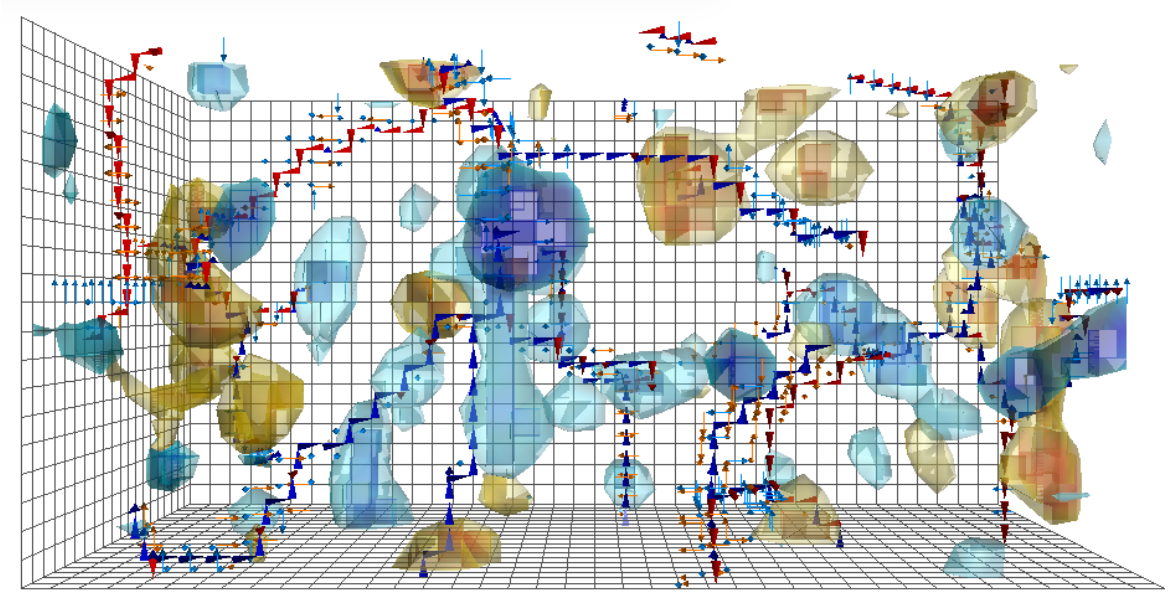

Fig. 4.17 The centre vortex structure and topological charge density after eight sweeps of cooling, for $t = 1$. (**Interactive**)

perfect correlation, $L(x) = 1$ for all i, and hence the numerator of Eq. 4.5 reduces to a sum over $|q_i|$. Hence,

$$C_{\text{Ideal}} = V \frac{\sum_{i=1}^{N} |q_i|}{\sum_x |q(x)| \sum_x L(x)} - 1 \,, \tag{4.7}$$

where N is the number of sites with $L(x) = 1$. By evaluating C/C_{Ideal} for each configuration, we obtain a normalised measure ranging between 0 and 1 for positively correlated quantities. Averaging over our configurations, we can make use of $\overline{C/C_{\text{Ideal}}}$ to quantitatively express the correlation strength between $L(x)$ and $|q(x)|$.

Evaluating C/C_{Ideal} and averaging over our ensemble of 100 configurations provides $\overline{C/C_{\text{Ideal}}} = 0.672(6)$. Thus, there is a significant correlation between the positions of vortices and topological charge density. The small uncertainty also indicates that this correlation is consistent across the ensemble.

Finally, we visualise the vortex configurations after smoothing to investigate how the vortex structure changes. The results, presented in Fig. 4.17, follow eight sweeps of $\mathcal{O}(a^4)$-improved cooling. We note that an enormous amount of the vortex matter is removed. However, it is well established that, under smoothing, the vortex-only configurations retain many of the salient long-range features of QCD [15, 17, 20], suggesting that the removed vortices are in some way irrelevant to these long-range properties.

4.3.2 Singular Points

Given the presence of the antisymmetric tensor in the definition of topological charge density presented in Eq. (4.3), it is clear that for there to be non-trivial topological charge present on the projected vortex configurations, we require the vortex field strength to span all four dimensions. This condition is met at *singular points*, where the tangent vectors of the vortex surface span all four dimensions. The contribution to the topological charge from these singular points is discussed in detail in Refs. [10, 62, 66, 69].

In our visualisations, singular points appear as a spatially-oriented vortex running parallel to the link identifier of a space-time oriented vortex, as shown in Fig. 4.18. Points satisfying this condition, whilst being difficult to locate by eye in our visualisations of space-time oriented vortices, actually occur frequently, as illustrated in Fig. 4.19. At these points we have vortices generating field strength in all four space-time dimensions. An example of a singular point is shown in Fig. 4.20.

The vortex configuration in Fig. 4.18 spans all four dimensions because the jet indicates a vortex in the x–y plane generating non-zero field strength $F_{xy}(x)$ and the z-oriented indicator link denotes a vortex in the z–t plane, giving rise to non-zero $F_{zt}(x)$. Hence, at the point x the topological charge density can be non-trivial.

Around the lattice site $\mathbf{x}$ in Fig. 4.18 there are four $x-y$ and four $z-t$ plaquettes, allowing for a multiplicity of 16. As there are three unique combinations of orthogonal planes in 4D (x–y and z–t, x–z and y–t, y–z and x–t), this gives a total maximum multiplicity of 48 for each singular point. However, this maximum is highly unlikely, and the highest multiplicity in the configuration shown in Fig. 4.19 is 12.

We can verify the relationship between singular points and topological charge by identifying vortices satisfying the parallel condition shown in Fig. 4.18 and plotting these points against the results of the topological charge calculation performed on the projected vortex-only configurations. As seen in Fig. 4.21, when we apply the correct sign to the odd index permutations we observe that there is perfect agreement between the location of singular points and the identified topological charge.

To quantify the correlation between $q(x)$ and singular points, we make use of a measure similar to that defined in Eq. (4.5),

$$C = V \frac{\sum_x |q(x)|\, L_s(x)}{\sum_x |q(x)|\, \sum_x L_s(x)} - 1\,. \tag{4.8}$$

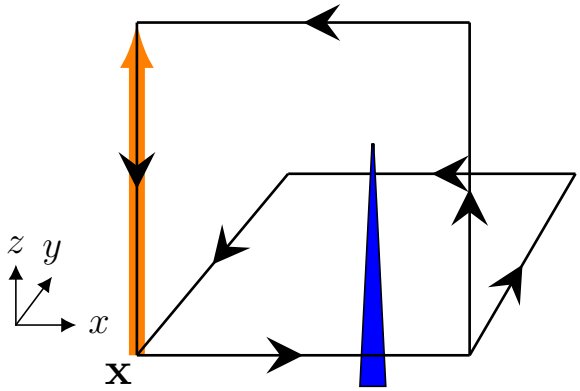

Fig. 4.18 The signature of a singular point, in which the tangent vectors of the vortex surface span all four dimensions. In this case, the blue jet is associated with field strength in the $x-y$ plane, and the orange space-time vortex indicator link is associated with a vortex generating field strength in the $z-t$ plane. Hence, the vortex surface spans all four dimensions.

However, we redefine our identifier $L(x)$ to be

$$L_s(x) = \begin{cases} 1\,, & \text{Singular point at } x, \\ \\ 0\,, & \text{Otherwise.} \end{cases} \tag{4.9}$$

In the case of singular points and $|q(x)|$ obtained from the projected configurations, we expect that the obtained correlation will be identical to the ideal value, calculated in the same manner as Eq. 4.7. This is indeed what we observe, with $\overline{C/C_{\text{Ideal}}} = 1$. In Sec. 4.3.4 we will make use of this measure again to examine the correlation between singular points and different topological charge density calculated prior to centre vortex projection where the expected values are less apparent.

4.3.3 Branching Points

The relationship between branching points and topological charge is of particular interest as they are important for generating regions of high topological charge density on the projected vortex configurations. To understand why, consider a clover term $C_{\mu\nu}$ as defined in Eq. (2.36). On a projected configuration, each of the four imaginary parts of the plaquettes in Eq. (2.36) can take one of three possible values: $\pm\sqrt{3}/2$ or 0. If a single vortex pierces the clover, it will contribute $|q(x)| = \sqrt{3}/2$. To obtain larger values of $|q(x)|$, it is necessary for multiple plaquettes in at least one of the clover

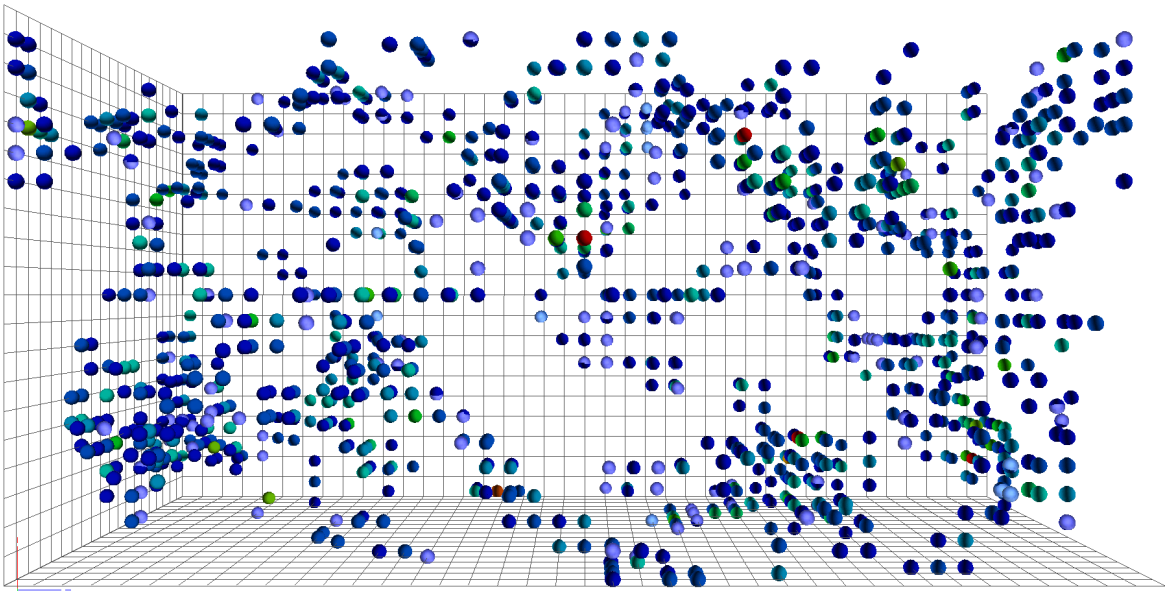

Fig. 4.19 All points on the $t = 1$ time slice in which a singular point occurs, i.e. a spatially-oriented vortex jet runs parallel to a space-time oriented vortex indicator link as shown in Fig. 4.18. The colour indicates the multiplicity M observed on this slice, with the lowest value in blue ($M = 1$) and the highest in red ($M = 12$). (**Interactive**)

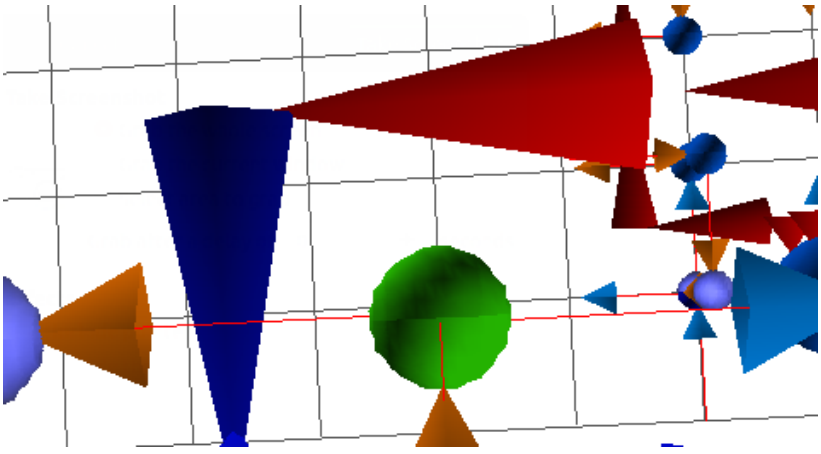

Fig. 4.20 A singular point (green sphere) resembling the structure of Fig. 4.18. This singular point is generated by the red jet and the orange indicator link running in parallel.

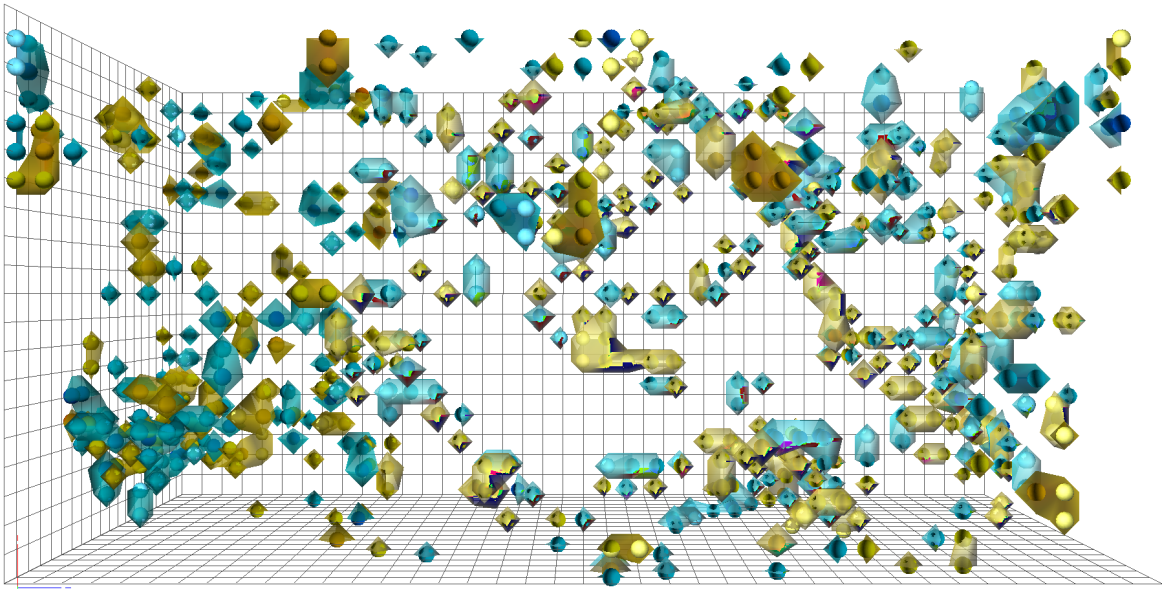

Fig. 4.21 Topological charge density from singular points (shown as dots) is compared with topological charge calculated from vortex-only configurations for $t = 1$. (**Interactive**)

terms to contribute both non-trivially and with the same sign so that the magnitude of the topological charge density increases above the lowest non-trivial value. This is equivalent to requiring that multiple vortex jets pierce the clover parallel to each other, such that they form a pattern like that shown in Fig. 4.22. To conserve the vortex flux, the configuration in Fig. 4.22 is most simply achieved by placing a branching point immediately below the two parallel vortices. Hence, there is reason to suspect that branching points may be well-correlated with regions of high topological charge.

The argument made above by no means claims that branching points *must* be associated with large values of $|q(x)|$, as there are most certainly alternative vortex arrangements that will lead to the same values. For example, a branching point could generate two parallel vortex lines that then continue parallel to one another for some distance, generating topological charge density away from the original branching point. Or alternatively, two separate vortex lines could come close to one another, running parallel without the need for any local branching point. Thus, the correlation between large values of $|q(x)|$ and branching points is not expected to be perfect. However, the presence of a correlation provides information on the role of branching points in generating large topological charge density. Inspection of the 3D model in Fig. 4.23 suggests a significant correlation, as is highlighted in Fig. 4.24.

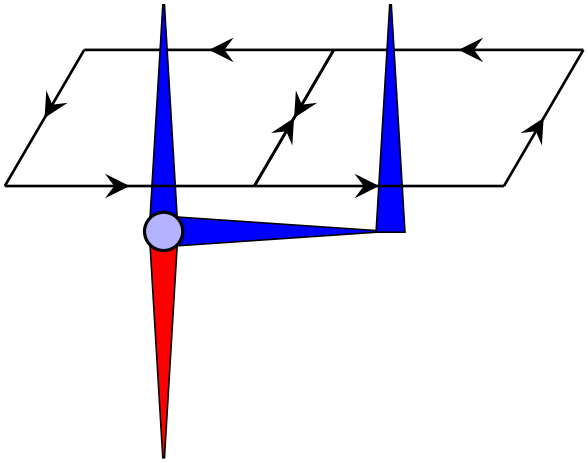

Fig. 4.22 An example of vortex branching generating a region of high topological charge by piercing two out of the four plaquettes that make up a clover.

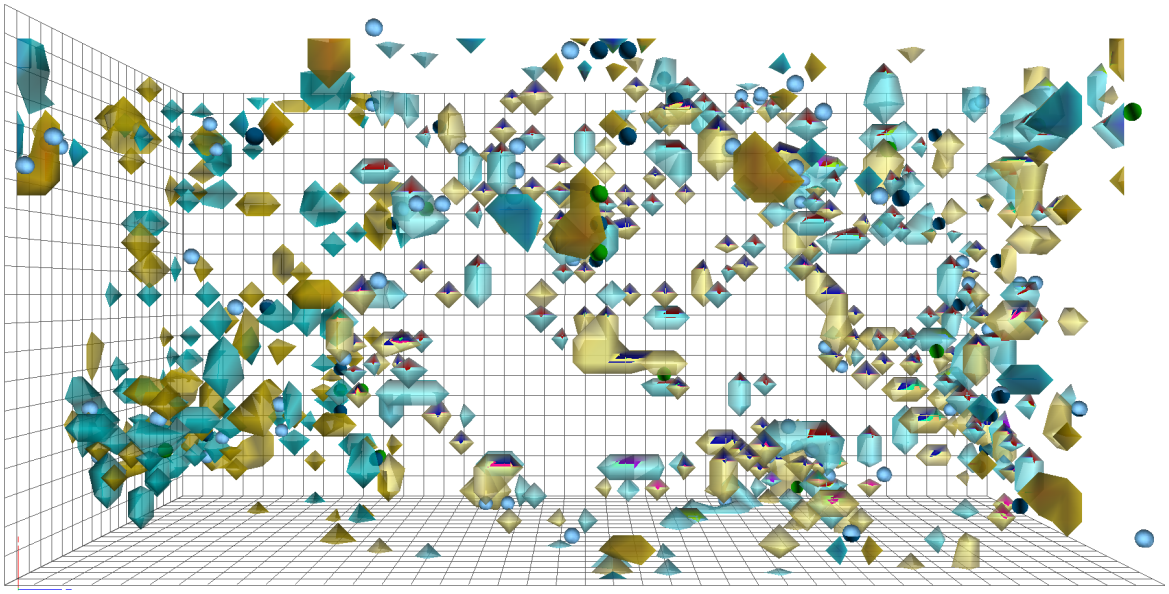

Fig. 4.23 Branching points (dots) plotted alongside the topological charge density from the projected vortex configurations. It can be observed that the branching points are almost always neighbouring topological charge density. (**Interactive**)

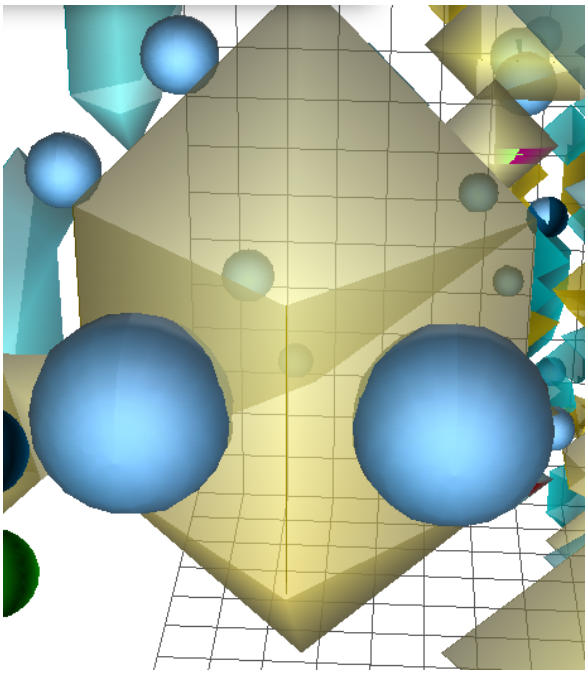

Fig. 4.24 An example of two branching points and their associated topological charge density.

To evaluate the correlation numerically we again make use of the measure defined in Eq. (4.5). As branching points exist on the dual 3D lattice of each time-slice, we denote the dual lattice sites by $\tilde{x}$. For the four unique combinations of three dimensions, xyz, xyt, xzt and yzt, we define our branching point indicator measure as

$$L_\mu(\tilde{x}) = \begin{cases} 1\,, & \text{Branching point associated with } \tilde{x} \\ & \text{in 3D slices of constant } \mu, \\ 0\,, & \text{otherwise}\,. \end{cases} \tag{4.10}$$

The μ index in Eq. (4.10) indicates which dimension is playing the role of time; i.e. which dimension is not included in the 3D cubes. Similarly, we define $q_\mu(\tilde{x})$ to be the average of the topological charge over each 3D cube around $\tilde{x}$. We then have four correlation measures for each 3D combination that can be averaged over, giving a total correlation of

$$C = \frac{1}{4}\sum_\mu V \frac{\sum_{\tilde{x}} |q_\mu(\tilde{x})|\, L_\mu(\tilde{x})}{\sum_{\tilde{x}} |q_\mu(\tilde{x})|\, \sum_{\tilde{x}} L_\mu(\tilde{x})} - 1\,. \tag{4.11}$$

By constructing the ideal correlation as defined in Eq. (4.7) for each choice of 3D coordinates and averaging as done in Eq. (4.11), we can also calculate the ideal correlation with which we can compare against.

With this measure now suitably defined, we find that we obtain an ensemble average of $\overline{C/C_{\text{Ideal}}} = 0.518(7)$. This result indicates that there is a notable correlation between branching points and topological charge density and, as expected, they are not the only source of large topological charge. This result is interesting as it speaks to the tendency of vortex lines to either re-combine or diverge away from branching points, rather than remain in close proximity to one another, which provides an interesting consideration for the construction of $SU(3)$ vortex models such as those presented in Refs. [12, 69].

4.3.4 Correlation with Topological Charge Density

When considering correlations between vortex matter and topological charge density, it is natural to wonder whether the vortex structures identified on the projected vortex-only configurations correlate to the topological charge density identified on the original configurations. As is well established, to accurately identify topological charge density directly from the lattice gauge links it is necessary to first perform smoothing to filter short-range fluctuations [95, 100].

To this end, we perform 5 sweeps of over-improved stout-link smearing, with smearing parameters $\epsilon = -0.25$ and $\rho = 0.06$ (see Section 3.4.3), to minimally smooth the configurations before extracting the topological charge density [95]. To ensure the smoothed configurations maintain information captured in the vortex projection, we also produce smeared configurations that are preconditioned in maximal centre gauge.

We also obtain vortices from these smoothed configurations by fixing them to maximal centre gauge and then centre projecting, giving us in total three vortex configurations and three topological charge configurations. The methods by which these ensembles are obtained are summarised in Fig. 4.25.

We now repeat our correlation calculations for the singular points, branching points and the vortices themselves for four new combinations of vortex and topological charge density configurations. These results, as well as the correlation results from the previous sections, are summarised in Fig. 4.26. We see that for all of the new correlations presented, there is a soft correlation between the vortex structures and the topological charge density. Of all the correlations of $q^{\text{S}}(x)$ or $q^{\text{PS}}(x)$ with vortex information, the strongest correlation is with the original $Z_\mu^{\text{VO}}(x)$. It is notable that the branching point correlation is similar to the vortex correlation in panels (a) and (b) of Fig. 4.26. These configurations best represent the physical gauge fields with minimal smoothing

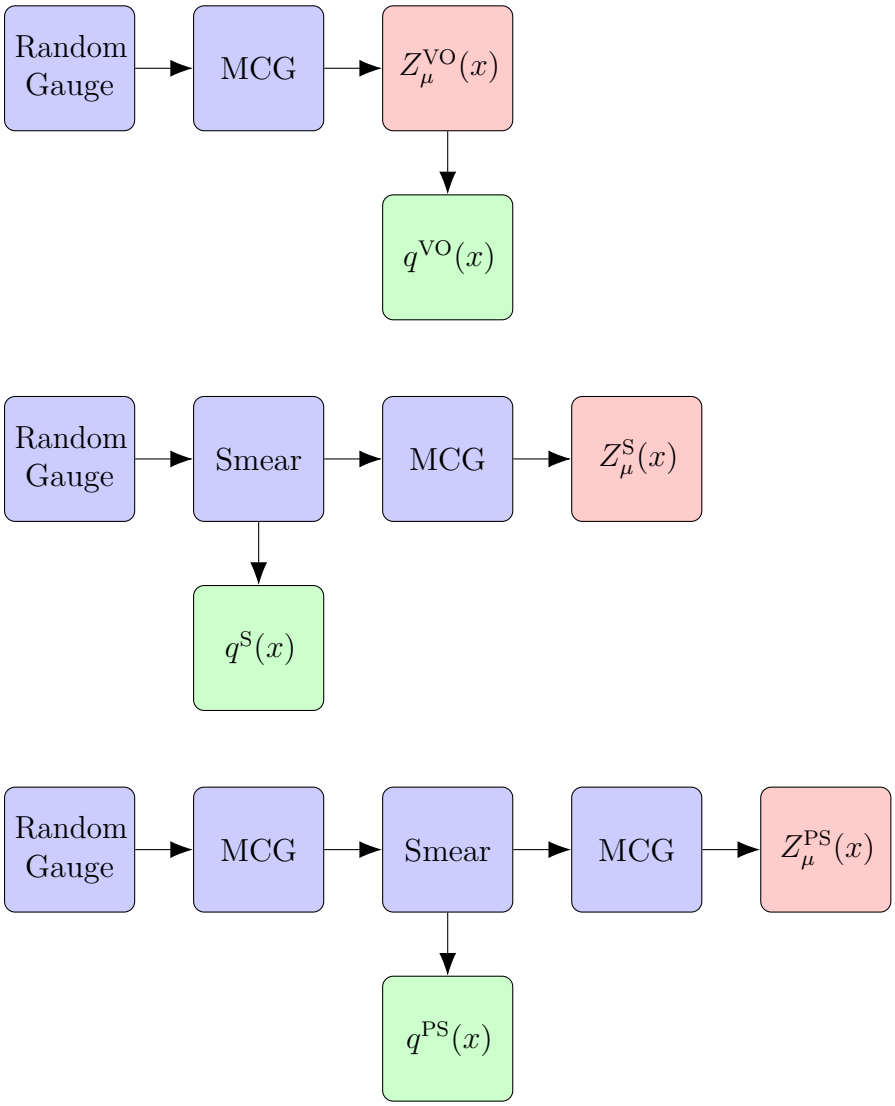

Fig. 4.25 Summary of the processes used to obtain vortex and topological charge density configurations. 'MCG' denotes gauge fixing to maximal centre gauge and 'Smear' denotes application of 5 sweeps of over-improved stout-link smearing as described in the text. From these methods we obtain the vortex only (VO), smeared (S) and preconditioned smeared (PS) topological charge and vortex configurations. As the topological charge density is gauge invariant, it could equivalently be calculated following gauge fixing to maximal centre gauge.

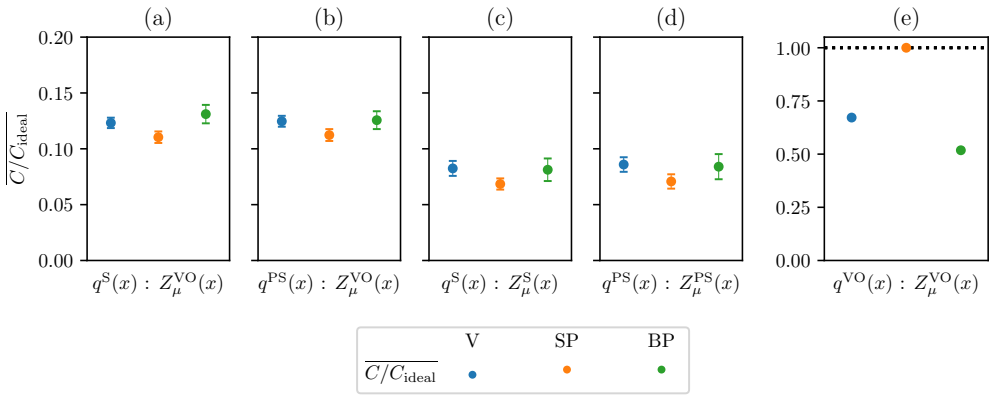

Fig. 4.26 Correlation values for vortices (V), singular points (SP) and branching points (BP) obtained from centre projected configurations, $Z_\mu(x)$, with topological charge density, $q(x)$, obtained via various means described in the text and shown diagrammatically in Fig. 4.25. Data points indicate results for the normalised correlation values, $\overline{C/C_{\text{Ideal}}}$.

to extract the topological charge, and as such this correlation has implications for the significance of branching points in regards to generating regions of significant topological charge density.

Of particular interest is the fact that the correlation does not improve when the vortex configuration is preconditioned by the same degree of smoothing as the topological charge, as shown in Fig. 4.26 (c) and (d). This suggests that the primary cause of the more subtle correlation is the vortex projection rather than the smoothing. In fact, we even observe that the correlation shifts further from the ideal value of 1 when the vortex configuration is obtained following 5 sweeps of smoothing. This arises because the number of vortex structures is reduced under smearing, as seen in Fig. 4.27, but the overlap with topological charge has clearly not improved substantially. As noted earlier in Fig. 4.17, under cooling this sparsity of vortices is further amplified, indicating that as the degree of smoothing increases, vortices are increasingly removed from the lattice.

An additional consideration for the observed correlation is the fact that projected vortices do not perfectly correlate with the location of the physical thick vortices. Rather, the projected vortices appear within the thick vortex core, but under different Gribov copies of maximal centre gauge they will be identified at different specific lattice sites [7]. This variability can contribute to the more subtle correlation observed in Fig. 4.26.

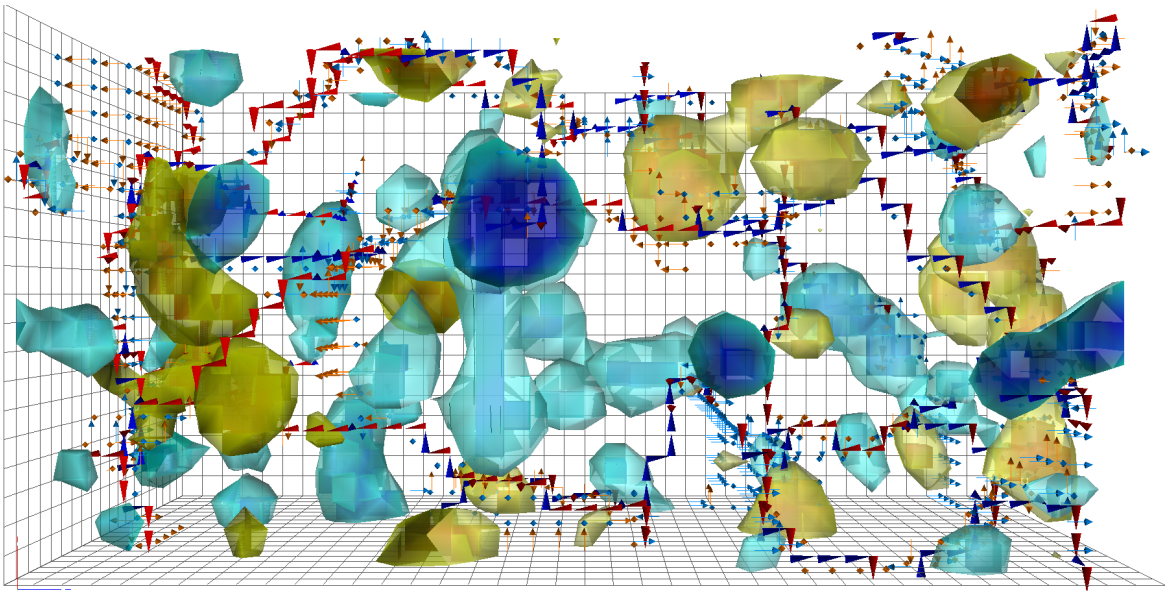

Fig. 4.27 The vortex structure and topological charge present after 5 sweeps of over-improved stout-link smearing, preconditioned with maximal centre gauge ($Z_\mu^{\mathrm{PS}}(x)$ and $q^{\mathrm{PS}}(x)$). (**Interactive**)

These findings reinforce the result that whilst centre vortices reproduce many of the salient features of QCD, vortex-only configurations are only subtly correlated with the topological charge density of the configurations from which they are obtained. However, the correlation does exist and is consistent across the ensemble, indicating that centre vortices are connected to the topological charge density of the lattice.

4.4 Conclusion

In this chapter we have presented a new way to examine the four-dimensional structure of centre vortices on the lattice through the use of 3D visualisation techniques. These visualisations give new insight into the geometry and Euclidean time-evolution of centre vortices, and reveal a prevalence of singular points and branching points in the vortex vacuum. It is especially remarkable how common branching points are in SU(3) gauge theory.

We have also explored the connection between these vortex structures and topological charge density. While demonstrating that the topological charge density obtained on projected vortex configurations is generated by singular points, we discovered an interesting correlation between branching points and topological charge; namely

that branching points provide an important mechanism for generating large values of topological charge density.

We explored the connection with topological charge density obtained from the original configurations after varying degrees of smoothing. We deduced that the topological charge density of the gauge fields is significantly affected under centre projection, however the modification maintains a positive correlation with the original topological charge density identified on the lattice. It is clear from the work presented here that analysis of the vortex vacuum through the use of novel visualisations provides new perspectives on the ground-state of QCD, and can highlight relationships that otherwise may go unnoticed.

Chapter 5

Static Quark Potential

This chapter is based on the paper "Static quark potential from centre vortices in the presence of dynamical fermions", Biddle, Kamleh, and Leinweber [22].

The discussion presented in Chapters 3 and 4 demonstrate the current understanding of the centre vortex picture in the context of pure Yang-Mills theory. A natural next step for the vortex model is to examine how the presence of dynamical fermions impacts the structure of centre vortices. Any subsequent shift in vortex structure can be measured by calculating observables arising from vortex-only and vortex-removed ensembles. In this chapter, we perform the first such analysis and present a calculation of the static quark potential on vortex-modified ensembles in the presence of dynamical fermions. After identifying centre vortices on the lattice, it is possible to isolate the contribution to the static quark potential from both the vortices alone and the original gauge field after vortex removal. This calculation reveals a significant shift in vortex structure induced by the presence of fermion loops in the vacuum fields and further reinforces the central role vortices play in producing the salient phenomena of QCD.

For the remainder of this thesis we shift our focus to the three $32^3 \times 64$ lattices described in Table. 2.1. We choose two dynamical ensembles with different pion masses to assess the dependence on the dynamical fermion mass, as well as making use of a pure-gauge ensemble with a lattice spacing similar to that of the dynamical ensembles to facilitate comparisons with the well-known behaviour of centre vortices in the pure gauge sector. This set of three ensembles allows us to effectively analyse the changes in the behaviour of centre vortices brought about by the introduction of dynamical fermions.

This chapter is structured as follows. Section 5.1 introduces the calculation of the static quark potential through the use of Wilson loops. Section 5.2 describes the variational method used to calculate the static quark potential. Section 5.3 discusses the results of this work, introducing novel modifications to the standard Coulomb term. Section 5.4 summarises our findings.

5.1 Static Quark Potential

As briefly mentioned in Section 3.1, the static quark potential provides a measurement of the potential between two massive, static quarks at a separation distance r. On the lattice, the static quark potential can be obtained by considering the Wilson loop

$$W(r,\, t) = \mathrm{Tr}\, R(\vec{x}, t_0) T(\vec{y}, t_0) R^\dagger(\vec{x}, t_1) T^\dagger(\vec{x}, t_0)\,, \tag{5.1}$$

which has two spatial paths connecting points $\vec{x}$ and $\vec{y}$ satisfying $|\vec{y} - \vec{x}| = r$ via the shortest set of links on the lattice. The forward spatial path $R(\vec{x}, t_0)$ is separated from the backward spatial path $R^\dagger(\vec{x}, t_1)$ by the temporal extent of the loop, $t_1 - t_0 = t$. The loop is closed via the static quark propagators $T(\vec{y}, t_0)$ and $T^\dagger(\vec{x}, t_0)$, which correspond to the product of links in the positive and negative temporal directions respectively. A diagram of this Wilson loop construction is shown in Fig. 5.1.

When the spatial separation extends off-axis to encompass displacements in more than one spatial direction, an oblique path is chosen to reduce rotational lattice artefacts. An integer step size vector $\vec{s}$ is initialised by taking the spatial separation $\vec{r}$ and dividing out the smallest element. If the two largest elements of $\vec{s}$ are both greater than 1, then these are divided by the smaller of the two so that the step size vector $\vec{s}$ has at most one element that is greater than 1. The spatial link path is constructed by cycling between the spatial directions $\hat{\jmath}$ with step size s_j. When the total displacement r_j in a direction $\hat{\jmath}$ has been reached we set the step size $s_j = 0$. This is perhaps most easily understood with an example. For $\vec{r} = (6, 3, 2)$, then the initial step size vector $\vec{s} = (3, 1, 1)$. The path $\vec{r}$ is traversed by starting at $\vec{x}$ and cycling through the steps $\vec{s} = (3, 1, 1)$ twice, then updating $\vec{s} = (0, 1, 0)$ to the remaining displacement to reach the end point $\vec{y}$.

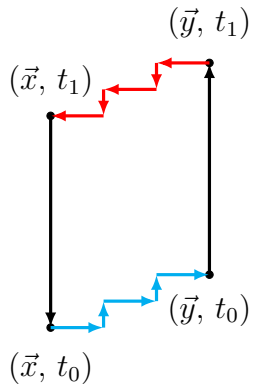

Fig. 5.1 Diagram of a Wilson loop. Shown are the forward (blue) and backward (red) spatial paths where different levels of smearing are used to create our variational matrix. Links in the positive temporal direction are oriented vertically upwards.

The expectation value of the Wilson loop is connected to the static quark potential V^α for state α via the expression

$$\langle W(r,\, t)\rangle = \sum_\alpha \lambda^\alpha(r)\, \exp\left(-V^\alpha(r)\, t\right)\, . \tag{5.2}$$

Here, α enumerates the sum over energy eigenstates. This expectation value in Eq. (5.2) is taken not only over the lattice ensemble, but over the range of spatial paths that provide the same r value. In this work, we consider a maximum of 16 on-axis points, and a range of 0 to 3 off-axis points. The temporal extent considered has a maximum of $t = 12$ for the untouched and vortex-removed ensembles, and a maximum of $t = 32$ for the vortex-only. The larger value for the vortex-only ensemble is used because the onset of noise occurs much later, and we find better plateau fits using this extended range.

Due to the cubic symmetry of the lattice, when considering a link path between two spatial points separated by a given displacement vector $\vec{r} = \vec{y} - \vec{x}$ it is possible to permute the three spatial coordinates and obtain the same value for the separation $r = |\vec{r}|$. Averaging over these permutations allows for further improvement of statistics for the corresponding Wilson loop and better extraction of the ground state.

5.2 Variational Analysis

The analysis of the static quark potential is susceptible to excited state contamination and signal to noise challenges. In particular, the dynamical ensembles are typically noisier at a given lattice spacing compared to the pure gauge case. To better extract the ground state potential at earlier Euclidean time, we create a correlation matrix by introducing different levels of smearing along the two spatial edges of the Wilson loops describing the profile of the flux tube,

$$W_{ij}(r,\, t) = \mathrm{Tr}\, R_i(\vec{x}, t_0) T(\vec{y}, t_0) R_j^\dagger(\vec{x}, t_1) T^\dagger(\vec{x}, t_0). \tag{5.3}$$

Here the forward and backwards paths $R_i(\vec{x}, t_0)$ and $R_j^\dagger(\vec{x}, t_1)$ are constructed using links that have respectively had i and j sweeps of spatial APE smearing [91] applied, with a smearing parameter of $\alpha = 0.7$. For the untouched and vortex-removed ensembles, the $SU(3)$ projection component of the APE smearing algorithm is performed using the unit-circle projection method described in Ref. [93].

As discussed in Section 3.4, the vortex-only ensembles present some difficulties in the application of standard smearing algorithms. To account for this, we perform centrifuge preconditioning to rotate the vortex-only ensembles away from the centre group, $\mathbb{Z}_3$. APE smearing with smearing fraction $\alpha = 0.7$ using Max Re Tr projection is then applied, as this avoids the issues associated with analytic projection when applied to VO ensembles. This procedure is suitable for generating a variational basis for the vortex-only configurations.

For N choices of smearing sweeps, we obtain the $N \times N$ correlation matrix

$$\begin{aligned} G_{ij}(r,t) &= \langle W_{ij}(r,t) \rangle \\ &= \sum_\alpha \lambda_i^\alpha \lambda_j^{*\alpha} \exp\left(-V^\alpha(r)\, t\right) \end{aligned} \tag{5.4}$$

where the i, j indices enumerate the N smearing variations on the initial and final spatial edges of the Wilson loop respectively. The complex scalars λ_i^α and $\lambda_j^{*\alpha}$ represent the coupling of each smeared leg of the Wilson loop to the static quark potential V^α. Note that in the following we choose to suppress the implied r dependence of G_{ij} and V for clarity.

Presuming that the signal is dominated by the N lowest energy states, such that $\alpha \in [0,\, N-1]$, we wish to find a basis $\mathbf{u}^\alpha$ such that,

$$G_{ij}(t)\, u_j^\alpha = \lambda_i^\alpha\, z^{*\alpha}\, e^{-V^\alpha\, t}\,, \tag{5.5}$$

where $z^{*\alpha} = \sum_i \lambda_i^{*\alpha}\, u_i^\alpha$ is now the coupling between this new basis and the energy eigenstate $|\alpha\rangle$. Note that for the remainder of this paper we adopt the convention that repeated Latin indices are to be summed over whilst repeated Greek indices are not. Eq. (5.5) is equivalent to requiring that

$$\lambda_i^{*\alpha}\, u_i^\beta = z^{*\alpha}\, \delta^{\alpha\beta}. \tag{5.6}$$

Noting that the time dependence in Eq. (5.5) enters only through the exponential term, we can consider stepping forward in time by some amount Δt such that,

$$\begin{aligned} G_{ij}(t_0 + \Delta t)\, u_j^\alpha &= \lambda_i^\alpha\, z^{*\alpha}\, e^{-V^\alpha\,(t_0+\Delta t)} \\ &= e^{-V^\alpha \Delta t}\, G_{ij}(t_0)\, u_j^\alpha\,. \end{aligned} \tag{5.7}$$

This recursive relationship is precisely a generalised eigenvalue problem, which can be solved via standard numerical techniques to obtain the eigenvectors $\mathbf{u}^\alpha$. An identical argument can be made for the left eigenvectors $\mathbf{v}^\alpha$, such that they satisfy

$$v_i^\alpha\, G_{ij}(t) = z^\alpha\, \lambda_j^{*\alpha}\, e^{-V^\alpha\, t}\,, \tag{5.8}$$

and hence

$$v_i^\alpha\, G_{ij}(t_0 + \Delta t) = e^{-V^\alpha \Delta t}\, v_i^\alpha\, G_{ij}(t_0)\,. \tag{5.9}$$

Making use of Eq. (5.5) and Eq. (5.9), we find that

$$v_i^\alpha\, G_{ij}(t)\, u_j^\beta = z^\alpha\, z^{*\beta}\, \delta^{\alpha\beta}\, e^{-V^\alpha\, t}\,. \tag{5.10}$$

As such, we define the eigenstate-projected correlator

$$\begin{aligned} G^\alpha(t) &= v_i^\alpha\, G_{ij}(t)\, u_j^\alpha \\ &= z^\alpha\, z^{*\alpha}\, e^{-V^\alpha\, t}\,, \end{aligned} \tag{5.11}$$

and extract the potential by computing the log-ratio

$$V_{\text{eff}}^{\alpha}(t) = \ln\left(\frac{G^{\alpha}(t)}{G^{\alpha}(t+1)}\right), \tag{5.12}$$

to obtain the static quark potential. We then consider constant fits to the lowest energy state, $V_{\text{eff}}^{0}(r,t)$.

We use a 4×4 correlation matrix for the untouched and vortex-removed ensembles, with a basis constructed from 6, 10, 18 and 30 sweeps of APE smearing. For the vortex-only ensembles, even with centrifuge preconditioning and MaxRe Tr reuniterisation applied, the configurations are still slow to vary as a function of smearing sweeps. As a consequence of this, we choose a 2×2 correlation matrix with 2 and 60 sweeps of APE smearing to provide a meaningful distinction between the basis elements.

For each calculation, we need to select fixed values for the variational parameters, t_0 and Δt. For the original and vortex-removed ensembles, we find that increasing Δt has minimal effect on the level of noise, whilst providing slight improvement in ground state identification. Thus, we choose a larger value of $\Delta t = 3$. Selecting larger values of t_0 introduces substantial noise into the results obtained from these ensembles, so we maintain $t_0 = 1$ on these ensembles.

Selection of variational parameters is slightly different on the vortex-only ensembles. For the diagonal correlators, $G_{ii}(t)$, where source and sink match and all states should contribute positively, i.e. $\lambda_i^{\alpha}\lambda_i^{*\alpha} > 0$, the effective mass approaches from below. This is indicative of short-distance positivity violation arising in the process of centre projection. In the context of a variational analysis, we extend t_0 to the greatest feasible degree to avoid the region of positivity violation at early times [101]. Indeed, our focus is on understanding whether projected centre vortices can capture the long-distance, nonperturbative features of QCD. To this end, we choose $(t_0,\ \Delta t)$ to be (5, 4), (4, 5) and (4, 2) for the pure gauge, $m_\pi = 701$ MeV, and $m_\pi = 156$ MeV vortex-only ensembles respectively. The difference in variational parameters between the ensembles arises from when the onset of noise dominates the signal.

To calculate uncertainties, we perform a third-order single-elimination jackknife calculation [102]. Fit window selection is performed to prioritise finding the earliest appropriate value of t_{min}, in a method similar to that outlined in Ref. [103]. As such, we select an initial t_{max} to be the largest value maintaining $V(r, t_{\text{max}}) > \Delta V(r, t_{\text{max}})$, where $\Delta V(r, t_{\text{max}})$ is the jackknife uncertainty in $V(r, t_{\text{max}})$. An initial value of $t_{\text{min}} = t_0 + 2$ is chosen. t_{max} is then decreased until a covariance fit over the range $[t_{\text{min}},\ t_{\text{max}}]$ produces

Table 5.1 The ansätze used for the three ensembles.

Type	Ansatz	Functional form
Untouched	Cornell	$V(r) = V_0 - \alpha/r + \sigma\, r$
Vortex-only	Linear	$V(r) = V_0 + \sigma\, r$
Vortex-removed	Coulomb	$V(r) = V_0 - \alpha/r$

a χ^2 per degree of freedom, $\tilde{\chi}^2$, of less than 1.3. If no such t_{max} is found, t_{min} is increased by one lattice unit and the procedure is repeated. The on-axis results of this fitting procedure are shown for the lightest pion mass ensemble in Fig 5.2. Once fits have been performed for all values of r, we select a single fit window with a width of at least two lattice units (i.e. at least three time values) such that it is typically encompassed by the range of fit windows found for each value of r.

After the potential $V(r)$ is determined, we then perform functional fits to the UT, VO and VR potentials. The ansätze used for each ensemble are given in Table 5.1. The functional fits take into account the full covariance matrix, and error regions are constructed via repetition of the fits on the jackknife ensembles. The selection of the range $[r_{\text{min}}, r_{\text{max}}]$ to fit over is performed in a manner similar to the fit window selection for the effective mass. For the UT and VR ensembles we initialise r_{min} to the lowest available value, as we find that our window selection method naturally avoids the short-range region that is plagued by lattice systematics. To explicitly avoid this region for the vortex-only potential, we initialise $r_{\text{min}} = 5$ for these ensembles. r_{max} is initialised to the largest available value on all ensembles. Over this initial range, the functional fit is performed and the χ^2 per degree of freedom, $\tilde{\chi}^2$, is calculated. If it is greater than 1.3 then r_{max} is reduced by $\Delta r = 0.2$ and the fit is repeated. If $r_{\text{max}} - r_{\text{min}} < 3$, r_{max} is reset to its maximum extent and r_{min} is increased by $\Delta r = 0.2$. In our plots, points that are included in the fit are shown in solid colours, whereas points excluded from the fit are shown as faded.

We also present plots of the local slope calculated from a series of linear fits taken over a sliding r window of width 4 lattice units. Each fit window is successively shifted in increments of $\Delta r = 0.4$ lattice units, with the fitted slope plotted at the left-most edge. We find that $r = 5$ is approximately where the onset of linearity begins, and hence we begin our sliding windows from this value. The excluded short-distance region is greyed out in the plots presented. This procedure for obtaining the local slope provides a simple method for gauging the linearity of the potential over a range of distances.

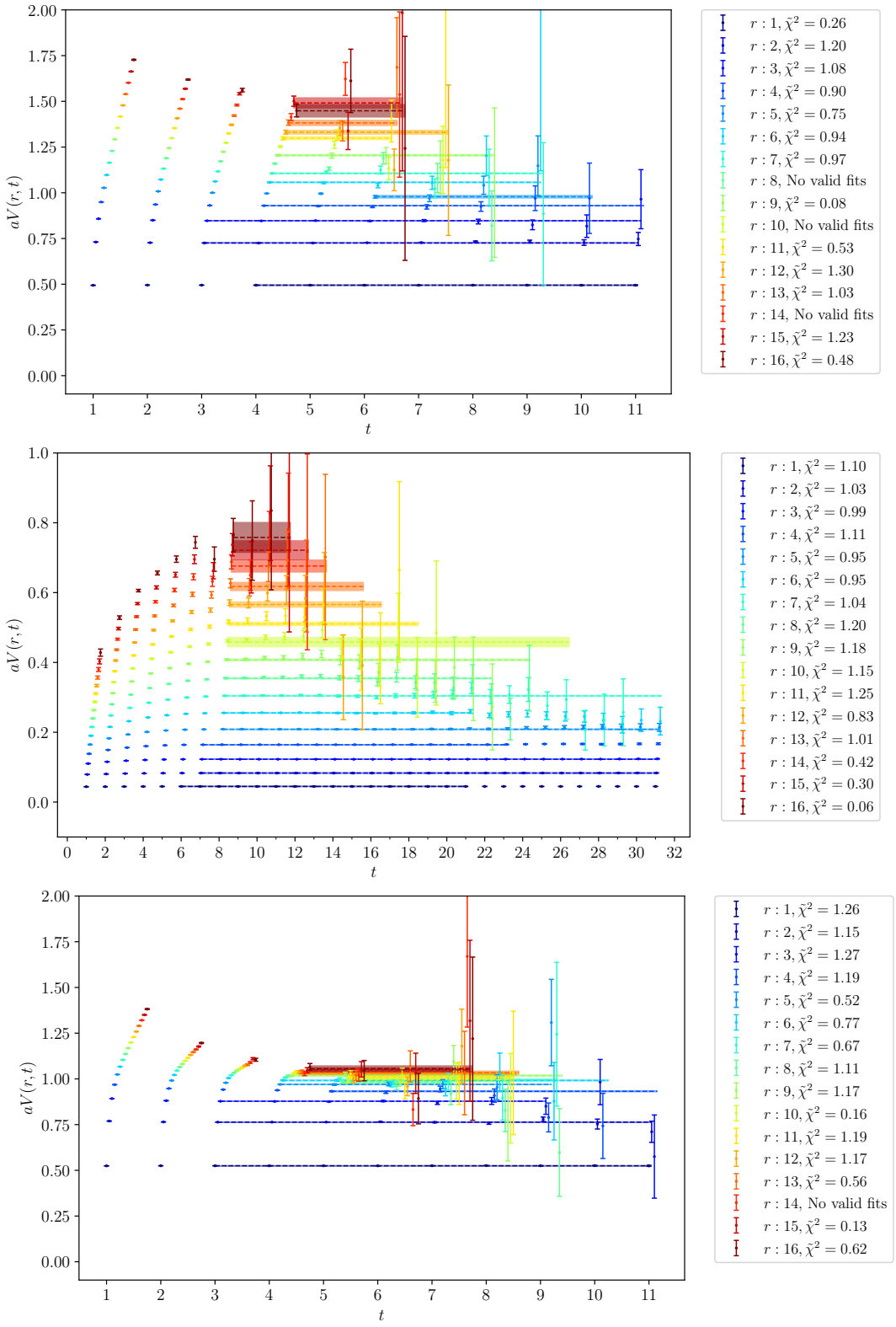

Fig. 5.2 The on-axis projected effective mass from the original $m_\pi = 156\,\text{MeV}$ ensemble. Results are shown for the original (**top**), vortex-only (**middle**) and vortex-removed (**bottom**) ensembles. The selected fit window that meets the $\tilde{\chi}^2$ criteria as described in the text is shown as the dashed lines. The shaded region shows the jackknife error on the fit. Points at the same value of t are horizontally offset for visual clarity. Any points with a relative error greater than 50% are excluded from the plot.

5.3 Results

We now present the results for the static quark potential. To verify that our variational technique is appropriate, we first calculate the vortex-only potential from the $m_\pi = 156$ MeV ensemble without a variational method to check if the results from the variational analysis are consistent and represent an improvement. Given the similarity of the lattice spacing on our three ensembles, summarised in Table 2.1, we will consider r in lattice units for the remainder of this work. We find that the fitted string tension is lower after a variational analysis, with $\sigma_{\mathrm{VO}} = 0.0484(4)$ and $\sigma_{\mathrm{VO}} = 0.0490(4)$ with and without variational analysis respectively. Additionally, the effective mass plateau fits occur at earlier times with the variational analysis, especially at larger r values. This suggests that the variational analysis is appropriate and represents an improvement over the naive method.

We show the VO potential with and without variational analysis in Fig. 5.3. Fitting is performed via the method outlined in the previous section. We observe from the local slope plot that the long range potential is similar across both methods. The fact that the differences are so slight is a testament to the excellent signal-to-noise ratio in vortex only ensembles and the subsequent access to large Euclidean times in the Wilson loops. Nevertheless, the use of a variational method does improve the onset of lower-lying plateaus and is thus preferred.

As we are studying gauge fields that include dynamical fermions, this gives rise to the possibility of string breaking. However, it is well known that there is poor overlap between the infinitely heavy static quark state and the heavy-light meson-meson state which arises from the string breaking transition [104]. To identify string breaking, it is instead necessary to include operators for heavy-light meson-meson states in the correlation matrix, as done in Refs. [104, 105].

The purpose of the variational analysis employed here is to ensure accurate identification of the ground state potential to enable comparison between the original and vortex-modified ensembles. Our basis does not include any of the appropriate operators to directly observe string breaking in this analysis. The inclusion of these operators requires inversion of the fermion matrix, which poses technical difficulties on the vortex-only fields due to their rough nature. These difficulties can be ameliorated with the use of sophisticated smoothing techniques such as those described in Ref. [89]. However, this would introduce a level of complication to the variational analysis beyond what is necessary for this study and is left to future work.

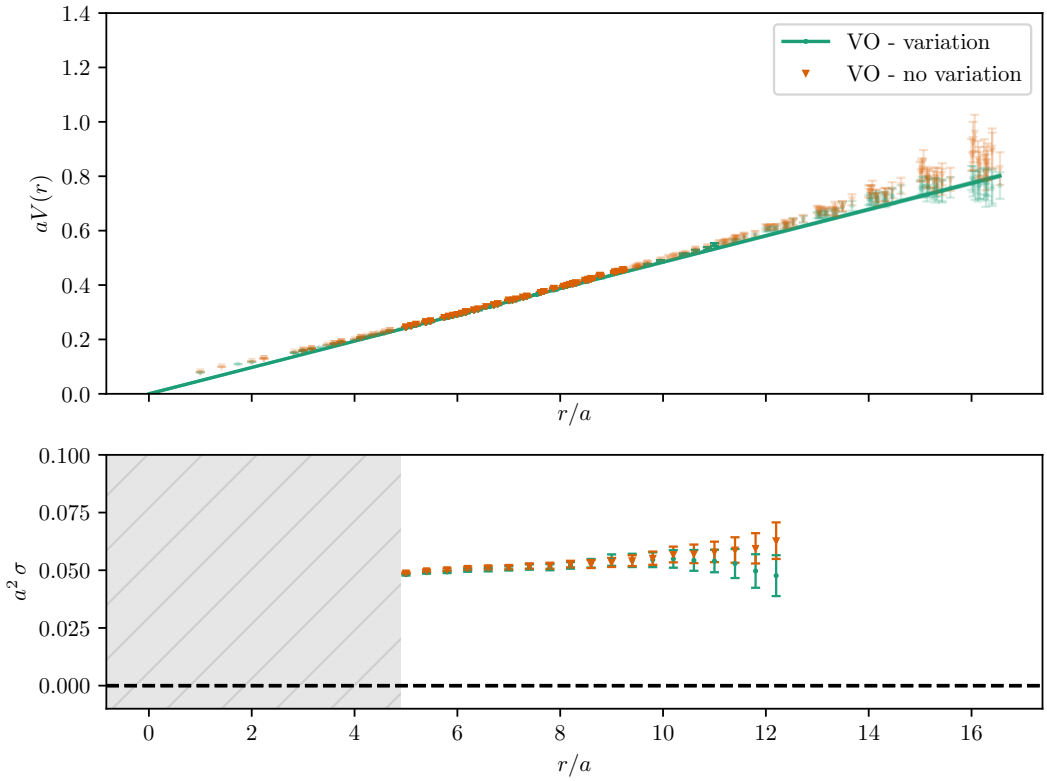

Fig. 5.3 A comparison of the vortex-only potential from the $m_\pi = 156$ MeV ensemble extracted after no spatial smearing and our variational method as described in the previous section. V_0 is set to 0 for both sets of results. The functional fit for the variational results is also plotted. We observe a similar potential for both choices, however the linearity of the fit is improved after a variational method, with a larger range of points meeting the fit criteria discussed in the text.

5.3.1 Standard Potential Fits

The static quark potential from the pure gauge ensemble is presented in Fig. 5.4. Our results coincide with findings from previous studies [13, 16, 17]. The untouched potential is Coulomb-like at short distances whilst becoming linear as r increases. We observe that the vortex-removed and vortex-only potentials of Table 5.1 qualitatively capture these regimes respectively. Vortex removal results in Coulomb-like behaviour at short distances, with approximately constant behaviour at moderate to large r indicating the absence of a linear string tension. We do note, however, that the Coulomb term provides a poor representation of the VR results at large r. Contrasting the vortex-removed results, we observe that the vortex-only ensemble features no $1/r$ behaviour, instead displaying a linear potential with a slope of approximately 62% that of the original ensemble.

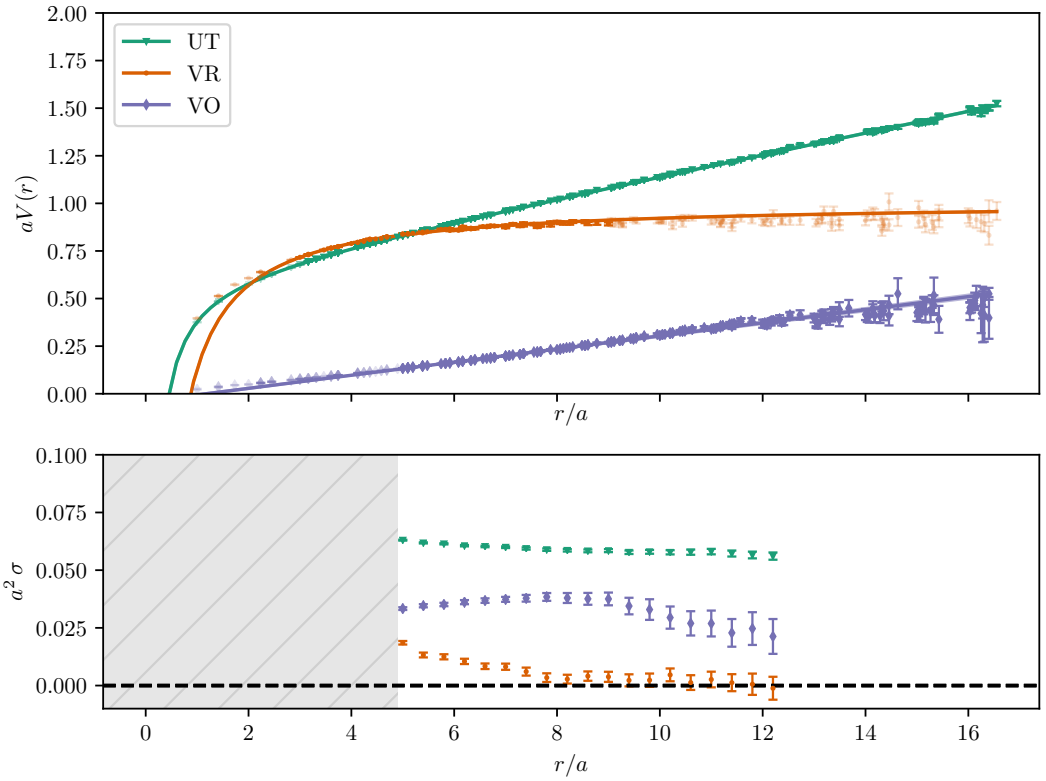

Fig. 5.4 The static quark potential as calculated from the pure Yang-Mills ensemble. Points are obtained from the variational analysis and solid lines show the fitted ansatz for each ensemble. The choice of ansatz is as described in Table 5.1. Faded points indicate that this point was not included in fitting the ansatz, as described in the text. The lower plot shows the fitted local slope of a forward-looking sliding linear window from r to $r + 4a$.

Table 5.2 The fitted string tensions from the vortex-only and untouched ensembles, and their respective ratios.

m_π (MeV)	$a^2\,\sigma_{\mathrm{VO}}$	$a^2\,\sigma_{\mathrm{UT}}$	$\sigma_{\mathrm{VO}}/\sigma_{\mathrm{UT}}$
Pure gauge	0.0344(9)	0.0558(3)	0.62(2)
701	0.0570(7)	0.0537(7)	1.06(2)
156	0.0484(4)	0.0386(1)	1.25(3)

The fitted string tension values from the untouched and vortex-only ensembles are presented in Table 5.2. The ratio of the vortex-only string tension to the untouched string tension is shown in the third column. We see that while the vortex field from the pure gauge background is only able to recreate 62% of the untouched string tension, in the presence of dynamical fermions there is a different story. The fitted vortex-only string tension increases upon the introduction of dynamical fermions at the heaviest pion mass. At $m_\pi = 701$ MeV the fitted string tension for the vortex-only and untouched fields are nearly equal, whereas on the lightest ensemble at $m_\pi = 156$ MeV the fitted string tension on the vortex-only field exceeds the untouched value by about 25%.

What is clear is that that the presence of dynamical fermions significantly alters the texture of the vortex vacuum, even at an unphysically large quark mass. The question then posed is how best to shed some light on the nature of this 'sea change.' Fig. 5.5 shows the static quark potential results for the heavy dynamical ensembles, with $m_\pi = 701$ MeV. Examining the local slope as it varies with r provides some insight. Note that the lattice spacings (as set by the Sommer scale) of the three ensembles listed in Table 2.1 are approximately the same, so it is reasonable to make broad comparisons in the slopes of the potentials.

As before, vortex removal captures the short-range physics while removing any linear rise associated with a confining potential. Strikingly, the vortex-only field projected from the dynamical ensemble now fully reproduces the long-range potential. This is best observed in the moving local slope displayed in the lower panel of Fig. 5.5. The more precise fitted string tension σ shows approximate agreement as reported in Table 5.2. This will be discussed in greater detail in the next subsection.

Finally, we present the static quark potential on the ensemble with the lightest pion mass of 156 MeV in Fig. 5.6. Here we observe the untouched and vortex-only slopes crossover, with approximate agreement of the local slope in the region $r \in [5.5, 7]$. As we extend to larger distances, we observe that the vortex-only string tension exceeds

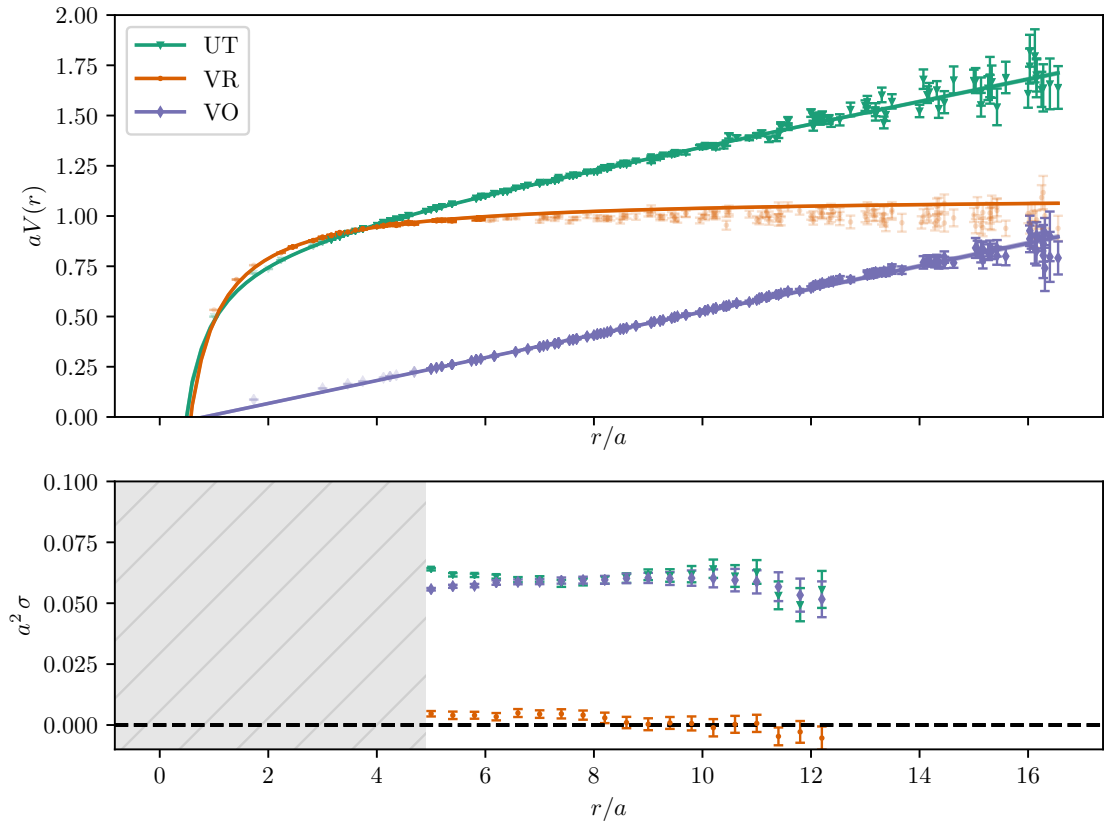

Fig. 5.5 The static quark potential as calculated from the $m_\pi = 701$ MeV ensemble, with features as described in Fig. 5.4.

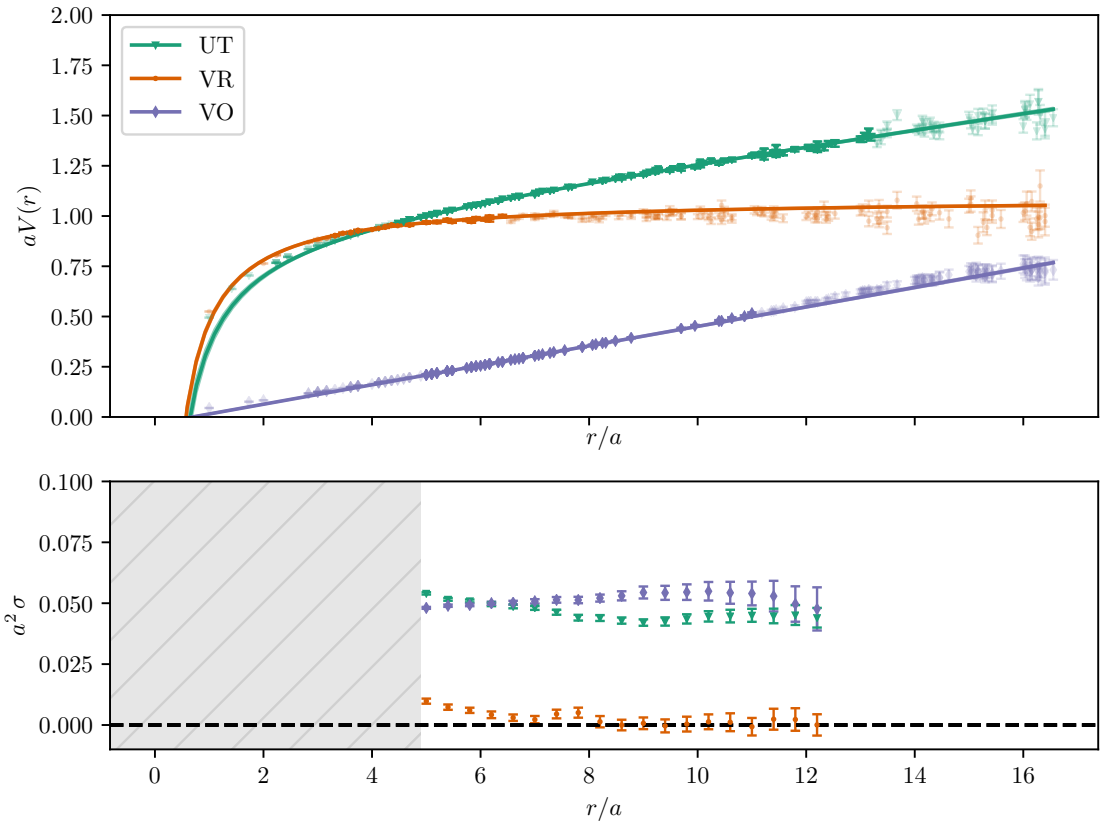

Fig. 5.6 The static quark potential as calculated from the $m_\pi = 156$ MeV ensemble, with features as described in Fig. 5.4.

Table 5.3 Results of the standard static quark potential fits to the three ensembles. The fit parameters are described in Table 5.1 and $\tilde{\chi}^2$ denotes the χ^2 per degree of freedom.

Type	$(r_{\min}, r_{\max})$	$\tilde{\chi}^2$	aV_0	α	$a^2\sigma$
Pure gauge					
UT	(3.10, 16.55)	1.12	0.608(3)	0.286(7)	0.0558(3)
VR	(3.00, 9.05)	1.23	1.010(2)	0.881(7)	–
VO	(5.00, 16.40)	0.97	−0.041(4)	–	0.0344(9)
$m_\pi = 701$ MeV					
UT	(3.10, 16.55)	1.30	0.847(7)	0.42(1)	0.0537(7)
VR	(3.00, 6.55)	1.30	1.092(4)	0.59(1)	–
VO	(5.00, 16.55)	1.03	−0.047(4)	–	0.0570(7)
$m_\pi = 156$ MeV					
UT	(4.40, 13.25)	1.29	0.93(1)	0.61(4)	0.0386(1)
VR	(3.10, 5.40)	1.28	1.106(5)	0.68(2)	–
VO	(5.00, 11.15)	1.28	−0.033(2)	–	0.0484(4)

the original value. This overestimation is corroborated by the fit values, where the value of σ reported in Table 5.2 is approximately 25% larger than the untouched.

The unanticipated overestimation of the VO string tension at the lightest mass gives an indication that there is some additional physics that is not being accounted for. A hint as to the possible answer is revealed in the vortex-removed fits. Specifically, the standard Coulomb term retains a residual increase in strength at moderate to large r that does not match the approximately constant behaviour of the vortex-removed results. The slow rise present in the standard Coloumb term could also interfere with the fitted linear term coefficient, resulting in an underestimation of the string tension in the UT results where both the Coulomb and string-tension terms are present.

Table 5.3 shows that as pion mass decreases, the fitted value of the Coulomb term coefficient, α, on the UT ensembles increases. This would then enhance possible contamination of the fitted UT string tension resulting from physics absent from the standard Coulomb term, amplifying the discrepancy between the original and vortex-only string tensions. This motivates modifications to the Coulomb term that we introduce in the next section in order to obtain better descriptions of the lattice results and more accurate estimates of the string tension.

5.3.2 Modified Coulomb Potential Fits

We have seen the difficulty in fitting the Coulomb term parameter, α, in our ansatz to a wide range of values on the dynamical ensembles. At the shortest distances, there is a well-known difficulty associated with fitting α for both the original and vortex-removed ensembles [106], stemming from the small statistical errors present at short range coupled with the presence of finite lattice-spacing systematics.

It is possible to apply a lattice correction to the Coulomb term to compensate for these short-distance artifacts [107, 108]. However, here we are mainly concerned with the long distance behaviour and adopt the simple solution of excluding small values of the static quark separation r from our fits.

A more serious limitation in the fit functions used above is revealed upon vortex removal. The standard Coulomb term is only able to describe the vortex-removed results over a limited range. This demonstrates a need for a modified fit function in order to describe the large r behaviour of the vortex-removed potential.

The decoupling of the static quark potential into the vortex-removed and vortex-only components also provides us with an opportunity. Specifically, the large r behaviour of the untouched potential is dominated by the linear string tension. The dominance of the linear term at large r hides any subleading effects.

The vortex-only component of the potential is well described by a linear string tension. The origin of the confining string tension is attributed to non-trivial vacuum structure, with the centre-vortex model of course being the most pertinent to this study. On the other hand, the vortex-removed potential does not possess a string tension as testified by the absence of a linear slope. This provides us with a chance to model effects that would otherwise be obscured by the rising linear string tension.

The first modified ansatz we propose is novel, with a model based on anti-screening of the Coulomb potential,

$$V_{\text{as}}(r) = V_0 - \frac{\alpha}{1 - e^{-\rho r}} \,. \tag{5.13}$$

The Laurent series of this function is dominated by the lowest order term $\tilde{\alpha}/r$ at short distances providing a Coloumb-like potential, where the effective Coulomb coefficient is $\tilde{\alpha} = \alpha/\rho$. Anti-screening implies that the strong coupling constant $\alpha_s(r)$ increases with increasing separation between two test colour charges. If α_s increases as r increases, this will have the effect of counteracting decreasing behaviour of the $1/r$ term.

Table 5.4 Results of the functional fits to the modified ansätze described in the text. The values of ρ for the untouched ensembles are fixed to the value obtained from the corresponding vortex-removed fit.

Type	$(r_{\min}, r_{\max})$	Fit function	$\tilde{\chi}^2$	$a\,V_0$	α	$a^2\,\sigma$	ρ
Pure gauge							
VR	$(2.90, 16.55)$	V_{as}	1.10	1.20(3)	0.27(3)	–	0.28(2)
VR	$(2.90, 16.55)$	V_{sc}	1.13	0.931(5)	1.01(3)	–	0.15(2)
UT	$(3.00, 16.55)$	$V_{\text{as}} + \sigma\,r$	1.16	0.652(4)	0.081(2)	0.0572(3)	0.28
UT	$(3.00, 16.55)$	$V_{\text{sc}} + \sigma\,r$	1.19	0.573(2)	0.301(7)	0.0572(3)	0.15
$m_\pi = 701$ MeV							
VR	$(1.80, 16.55)$	V_{as}	0.97	1.42(2)	0.42(3)	–	0.53(2)
VR	$(1.80, 16.55)$	V_{sc}	1.01	1.005(2)	0.85(2)	–	0.31(2)
UT	$(3.00, 16.55)$	$V_{\text{as}} + \sigma\,r$	1.29	1.02(1)	0.259(9)	0.0588(5)	0.53
UT	$(3.00, 16.55)$	$V_{\text{sc}} + \sigma\,r$	1.30	0.761(4)	0.54(2)	0.0585(5)	0.31
$m_\pi = 156$ MeV							
VR	$(3.00, 16.40)$	V_{as}	1.18	1.48(6)	0.48(6)	–	0.51(4)
VR	$(3.00, 16.40)$	V_{sc}	1.18	1.009(3)	1.05(8)	–	0.33(3)
UT	$(4.40, 9.25)$	$V_{\text{as}} + \sigma\,r$	1.28	1.17(4)	0.37(3)	0.0459(9)	0.51
UT	$(4.40, 9.25)$	$V_{\text{sc}} + \sigma\,r$	1.28	0.804(7)	0.84(7)	0.0457(9)	0.33

The specific form of the ansatz we have chosen here is motivated by the observation of the flat, constant-like behaviour of the vortex-removed potential at large distances. Specifically, at large r the exponential in the denominator of Eq. (5.13) tends to zero, such that a constant value $V_{\text{as}} \to V_0 - \alpha$ is rapidly approached as r increases. The implication of this is that the running coupling, α_s, is approximately linear in r within the fitted region. Previous lattice studies of the running of the strong coupling do show an increase in α_s with the separation r, although they are limited in the applicable range of scale (up to $\sim$0.5 fm) [107, 109, 110]. Importantly, the form of Eq. (5.13) is controlled such that the large r behaviour cannot describe a rising linear potential tension and hence should not interfere with a fitted string tension.

Intuitively, anti-screening can be understood by noting that at short distances gluons carry colour charge away from a quark or anti-quark such that the effective colour charge within a given radius is diluted, leading to asymptotic freedom at short distances [111]. We know from previous studies of the pure-gauge vortex-removed gluon propagator that flat behaviour consistent with asymptotic freedom is observed at large q^2 [15]. We also know that anti-screening arises from the non-Abelian nature of the gluon field, and as the vortex-removed field remains non-Abelian it seems reasonable to postulate that anti-screening will still be present in the absence of confinement.

Of course there are more sophisticated calculations of the running of α_s [110, 112–117], but these have limited applicability here, either due to the limited range of perturbation theory in QCD or being inspired by the string tension. It is not clear how these apply to vortex-modified fields. Here we choose instead to simply model the observed behaviour of the vortex-removed potential.

We also consider an alternative model to fit the vortex-removed results. The second modified ansatz we propose is a screened Coulomb potential, commonly known as the Yukawa potential,

$$V_{\text{sc}}(r) = V_0 - \frac{\alpha}{r}\, e^{-\rho r}\,. \tag{5.14}$$

Once again this has a Coulomb-like $1/r$ behaviour at small r. At large r the exponential term has the effect of turning off the Coulomb interaction such that $V_{\text{sc}} \to V_0$ as r increases.

One interpretation of the Yukawa model in this context is that the gluon dynamically acquires an effective mass ρ in the infrared. As a non-zero gluon mass is forbidden at the Lagrangian level by gauge invariance, this mechanism must be dynamical and

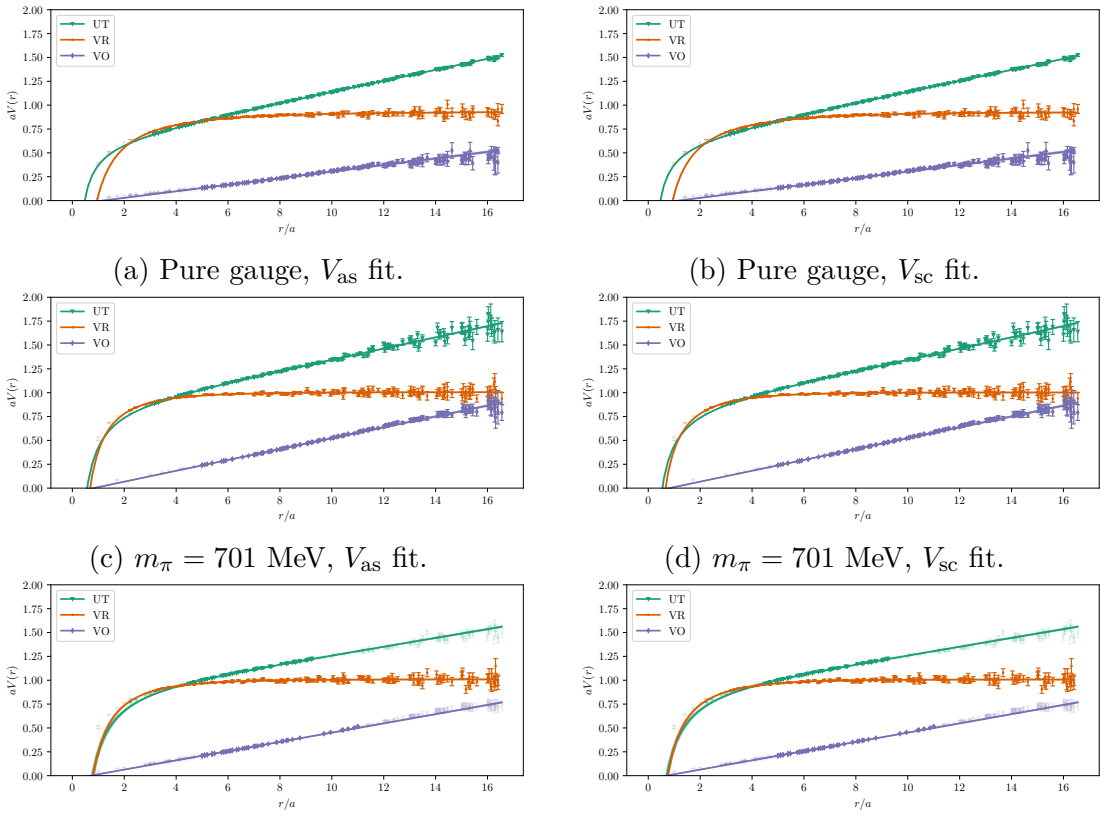

(a) Pure gauge, V_{as} fit.

(b) Pure gauge, V_{sc} fit.

(c) $m_\pi = 701$ MeV, V_{as} fit.

(d) $m_\pi = 701$ MeV, V_{sc} fit.

(e) $m_\pi = 156$ MeV, V_{as} fit.

(f) $m_\pi = 156$ MeV, V_{sc} fit.

Fig. 5.7 Fits to the lattice results for the potentials using the modified Coulomb term functions V_{sc} and V_{as} described in the text. The vortex-removed results are now described well by the modified potentials.

scale-dependent. Indeed, the dynamical generation of an effective gluon mass has been proposed elsewhere as a possible mechanism for the gluon propagator to take a finite value in the infrared limit [118–123].

It must be emphasised that the finiteness of the gluon propagator in the infrared limit is distinct to the presence (or absence) of confinement. The signature of confinement is dependent on the nature of the running of the gluon mass. Specifically, gluon confinement is associated with an inflection point or turn-over in the gluon propagator, which in turn implies the running gluon mass should not be constant. We know that vortex-removed theory does not generate a string tension and hence is non-confining. Introducing the possibility of a constant effective gluon mass at a finite scale would model the vortex-removed potential in a way which is separate to any confinement mechanism. It should also be noted that the relationship between gluon confinement and quark confinement remains an open question. The former is observed through

the inflection point in the gluon propagator and the latter through the static quark potential.

We now turn to the results from our modified Coulomb ansätze. Table 5.4 presents the fit parameters, with the resulting potentials illustrated in Fig. 5.7. We see that both V_{as} and V_{sc} are able to describe the vortex-removed results well, with similar values for the reduced χ^2. At first glance it seems somewhat counter-intuitive that both an anti-screened and screened model are able to describe the same results. Numerically, this is possible because of the interplay between the V_0 and α. Both ansätze approach a constant value in the large r limit, with $V_{\text{as}} \to V_0 - \alpha$ and $V_{\text{sc}} \to V_0$ respectively.

We see that both modified ansätze provide a superior fit to the vortex-removed results when compared to the standard Coulomb ansatz, allowing the fit window to extend to the maximum available r_{max}. In all cases the fitted value of r_{min} is less than or equal to the standard potential fits, indicating that the modifications made to the Coulomb terms are still able to account for the short distance behaviour of the potential up to the presence of lattice artefacts.

Having verified that our modified ansätze are successfully able to describe the vortex-removed potential results at large r, we can then use this information to improve our fits to the untouched results. This is accomplished by fixing ρ to be the value obtained from the corresponding vortex-removed ensemble, then adding a linear term to accommodate the string tension component of the untouched potential. The motivation behind fixing ρ is that the cleanest fit value for this parameter will be obtained in the absence of a string tension term which will dominate the large r behaviour. Indeed, we find that if left as a free parameter ρ is poorly constrained by the untouched potential fits due to the presence of the dominating linear term.

The fits to the untouched ensembles are of comparable range and $\tilde{\chi}^2$ to the original Cornell fits, however when we look at the ratio of the vortex-only string tension to the untouched, shown in Table 5.5, we see the significant impact the modified Coulomb terms play. The untouched string tension on the pure gauge ensemble is similar to the Cornell fit value, however on the dynamical ensembles the string tension is increased due to cleanly removing the contamination from the slow rise in the standard Coulomb term at moderate to large r. Remarkably, this results in agreement between the vortex-only and untouched string tensions on both dynamical lattices, as seen by the corresponding ratios taking values close to unity in Table 5.5.

The fits to the results are unable to distinguish between the two modified ansätze. Indeed, the resulting improvements to the untouched potential fits result in values for

Table 5.5 Ratios of the vortex-only to untouched string tensions from the Cornell and modified fit functions.

m_π (MeV)	$\sigma_{\rm VO}/\sigma_{\rm UT}^{\rm cornell}$	$\sigma_{\rm VO}/\sigma_{\rm UT}^{\rm as}$	$\sigma_{\rm VO}/\sigma_{\rm UT}^{\rm sc}$
Pure gauge	0.62(2)	0.60(2)	0.60(2)
701	1.06(2)	0.97(2)	0.97(2)
156	1.25(3)	1.05(2)	1.06(2)

the string tension that are essentially identical. We also tested an n-tuple form factor, $(1 + (r/\rho)^n)^{-1}$, to suppress the Coulomb term at large r, and this provided a similar result. This gives us confidence that any systematic errors arising from the modified Coulomb terms are minimal in the final string tensions reported.

The physical arguments provided for the two modified ansätze are simply to demonstrate some plausible mechanisms that might underpin their empirically motivated forms. Due to the interplay between α and V_0 it is likely that more than one effect will contribute to the fitted values. With a high-precision scaling analysis, a future examination may be able to resolve the physics represented by these modifications. The key result here is that by successfully modelling the observed long distance behaviour of the vortex-removed potential, we have been able to remove a source of contamination in the untouched potential fits and provide improved values for the fitted string tension for the first time.

For a given ansatz, the fitted value of ρ on the two dynamical lattices are similar, and are roughly double the fit value on the pure gauge ensemble. This indicates that the effects contributing to the medium to long-range behaviour of the vortex-removed potential are mainly sensitive to the presence or absence of dynamical fermions, but are only weakly dependent on the sea quark mass.

There are indications of increased screening by the light dynamical fermions in both the untouched and vortex-only results. Significantly, at longer distances we observe both modified ansätze show a decrease in the fitted value of the untouched and vortex-only string tensions when transitioning from the heavy to light pion mass.

As we have not corrected for short-distance lattice artefacts the fitted values of α should be interpreted with some caution, but are also worth discussing. The Coulomb term coefficients arising from the fits to the untouched potentials are summarised in Table 5.6 (recalling that for the $V_{\rm as}$ ansatz the effective short-distance coupling is $\tilde{\alpha} = \alpha/\rho$). For the pure gauge ensemble, the fitted values are close to the universal

Table 5.6 The (effective) Coulomb term coefficients from the Cornell and modified fits to the untouched potentials.

m_π (MeV)	$\alpha_{\mathrm{UT}}^{\mathrm{cornell}}$	$\tilde{\alpha}_{\mathrm{UT}}^{\mathrm{as}}$	$\alpha_{\mathrm{UT}}^{\mathrm{sc}}$
Pure gauge	0.286(7)	0.293(7)	0.301(7)
701	0.42(1)	0.49(2)	0.54(2)
156	0.61(4)	0.72(6)	0.84(7)

value of $\pi/12 \simeq 0.26$ derived from a thin flux tube effective field theory [124]. We observe the Coulomb couplings increase with decreasing sea quark mass for all three ansätze considered herein. This trend has been previously observed for the standard potential fits in Ref. [125]. It is interesting to see that this trend is replicated in our modified fits as well, as it suggests that the modified Coulomb terms are sensitive to the same short-distance physics as the standard ansatz.

The crucial finding of this work is that the introduction of dynamical fermions at any pion mass induces a measurable shift in the behaviour of centre vortices. Applying the modified ansätze introduced herein, the pure gauge vortex-only potential remains unable to reproduce the untouched string tension, whereas in contrast the respective dynamical string tensions show good agreement. The vortex-removed ensembles consistently show complete removal of the long range confining potential. This reinforces the argument that the salient non-perturbative properties of the ground state vacuum fields are encapsulated in the centre vortex degrees of freedom.

5.4 Conclusion

In this chapter we have presented the first calculation of the static quark potential from centre vortices obtained in the presence of dynamical fermions in QCD. The difficulties in fitting a standard Coulomb term to a wide range of vortex-removed values revealed a source of systematic contamination at moderate to large separations, resulting in the under estimation of the untouched string tension. In response we proposed two modified Coulomb ansätze. The first modified ansatz seeks to model the effect of anti-screening in the running coupling for QCD. The second modified ansatz takes the form of a Yukawa potential, accomodating a dynamical effective gluon mass. Both ansätze for the vortex-removed potential approach a constant value in the large r limit, and are able to describe the static quark potential on the vortex-removed ensembles.

Extending the modified Coloumb potentials with a linear string tension enables fits to the untouched potential.

The vortex-removed ensembles lack a linear confining potential for both the large and small pion masses considered here. Resolving the long-range behaviour of the vortex-removed static quark potential with the fit parameter ρ enables us to remove a source of systematic contamination in the untouched potential fits, providing an improved determination of the untouched string tension. In doing so, we find good agreement between the vortex-only and untouched string tensions in the presence of dynamical fermions. The fact both modified ansätze yield fit values for the string tension that are essentially identical suggests that any systematic errors introduced by the modifications are minimal. Evidence of quark loop screening is seen at the light quark mass.

These results suggest that the presence of dynamical fermions resolves the pure-gauge discrepancy between the original and vortex-only potential at large distances, presenting an important step in understanding the QCD vacuum. Historically, despite remarkable qualitative results, the centre-vortex model has not agreed quantitatively with pure Yang-Mills calculations. It is fascinating to see that with the improvements presented here that good agreement is achieved for the string tension with the introduction of dynamical fermions in full QCD.

It is important to note that the mechanism for the observed phenomenological improvement is currently unknown. In pure gauge theory the identified centre vortex string tension is dependent on the specific gauge fixing procedure [7, 10, 11, 126, 127]. For example, in Laplacian centre gauge the full string tension is recovered [128–133]. Future investigation into these gauge fixing dependencies with vortices derived from dynamical gauge fields would assist in further understanding the differences that have been observed herein.

Another avenue of improvement would be to expand the variational operator basis. In particular, the inclusion of a heavy-light meson-meson operator may clarify the long-range behaviour of the vortex-modified potential and reveal possible connections to string breaking.

The concept of *separation-of-charge* (S_c) confinement has been proposed elsewhere and studied in the context of the gauge-Higgs model [134–137]. Key to this concept is the existence of an order parameter, analogous to the Edwards-Anderson order parameter for spin-glass systems, that can be calculated to determine if a given vacuum phase is S_c-confining. It has not yet been verified numerically if QCD is S_c-confining.

Testing the response of the corresponding order parameter to vortex projection/removal would also be an interesting line of future study.

Despite the scope for future improvement, these findings strengthen the evidence that centre vortices are responsible for the long-range confining potential of QCD, and provide a first glimpse of the interplay between centre vortices and dynamical fermions. Motivated by these powerful results, in the next chapter we explore the gluon propagator from vortex modified ensembles in the presence of dynamical fermions.

Chapter 6

Gluon Propagator and Positivity Violation

This chapter is based on the paper "Impact of Dynamical Fermions on the Centre Vortex Gluon Propagator", Biddle, Kamleh, and Leinweber [23].

The results presented in Chapter 5 demonstrated for the first time a quantitative agreement between the vortex-only static quark potential and the corresponding untouched potential. These results motivate further exploration of the relationship between centre vortices and dynamical fermions. Here we continue this line of investigation by calculating the Landau gauge gluon propagator on the same three ensembles utilised in the previous chapter.

We will also examine the gluon spectral density by calculating the Euclidean correlator to determine the presence or absence of positivity violation. Positivity violation serves as an indicator of gluon confinement [138]. It is well understood that positivity violation in the gluon and quark propagators is a necessary condition for light-quark confinement [139]. As such, positivity violation arising from centre vortices serves as a strong indication that the centre vortex mechanism underpins the confinement of physical particles.

6.1 Gluon Propagator

6.1.1 Definition

In the continuum, the momentum-space Landau gauge gluon propagator is of the form

$$D^{ab}_{\mu\nu}(q) = \left(\delta_{\mu\nu} - \frac{q_\mu q_\nu}{q^2}\right) \delta^{ab}\, D(q^2)\,, \tag{6.1}$$

where where $D(q^2)$ is the scalar gluon propagator. On the lattice, the scalar propagator for $p^2 \neq 0$ is calculated by considering [15]

$$D(p^2) = \frac{2}{3\,(n_c^2 - 1)\,V}\Big\langle \mathrm{Tr}\, A_\mu(p)\, A_\mu(-p)\Big\rangle\,. \tag{6.2}$$

where $n_c = 3$ is the number of colours, V is the lattice volume and $A_\mu(p)$ is calculated via the discrete Fourier transform of the midpoint definition of the gauge potential [140],

$$A_\mu(x + \hat{\mu}/2) = \frac{1}{2i}\,\Big(U_\mu(x) - U^\dagger_\mu(x)\Big) - \frac{1}{6i}\,\mathrm{Tr}\,\Big(U_\mu(x) - U^\dagger_\mu(x)\Big) + \mathcal{O}(a^2)\,. \tag{6.3}$$

As the gauge fields used in this analysis are generated using the $\mathcal{O}(a^2)$-improved Iwasaki action [141], the tree-level behaviour of the gluon propagator is improved by making the substitution [29, 142, 143]

$$p_\mu \to q_\mu = \frac{2}{a}\sqrt{\sin^2\left(\frac{p_\mu a}{2}\right) + \frac{1}{3}\sin^4\left(\frac{p_\mu a}{2}\right)}\,, \tag{6.4}$$

where p_μ are the usual lattice momentum variables

$$p_\mu = \frac{2\pi\, n_\mu}{a N_\mu}, \quad n_\mu \in \left(-\frac{N_\mu}{2}, \frac{N_\mu}{2}\right]\,, \tag{6.5}$$

and N_μ is the lattice extent in the μ direction. The tree-level continuum scalar propagator is then given by $D(q^2) = \frac{1}{q^2}$. This choice of momentum variables reduces the sensitivity of the gluon propagator to finite lattice spacing effects at large momenta [144].

The perturbative scalar propagator is defined as $D(q^2) = \frac{Z(q^2)}{q^2}$. For the remainder of this section we will focus on the renormalisation function $Z(q^2) = q^2\, D(q^2)$. We then renormalise $Z(q^2)$ in the momentum space subtraction (MOM) scheme [145, 146] on the untouched configurations by enforcing the condition that $Z^{\mathrm{UT}}(\mu^2) = 1$ at the largest available momentum on all ensembles, $\mu = 5.5$ GeV. This is performed via

determination of a constant Z_3^{UT} satisfying

$$\frac{Z_{\mathrm{bare}}^{\mathrm{UT}}(\mu^2)}{Z_3^{\mathrm{UT}}} = Z^{\mathrm{UT}}(\mu^2) = 1\,. \tag{6.6}$$

Renormalising the vortex-modified results requires more careful consideration, as there is no *a priori* method by which it should be performed. Specifically, the problem arises from the absence of a perturbative expectation for the vortex-only propagator. The vortex-removed results are expected to encapsulate the high-momentum behaviour, and as such one can reasonably expect that the MOM scheme method would apply to these ensembles. However, the vortex-only results are dominated by infrared strength and a decay to 0 at high momentum. Hence, a multiplicative renormalisation based on a perturbative expectation does not apply.

To approach this renormalisation issue, we present two sets of results. The first set will display all propagators from an ensemble divided by Z_3^{UT} as determined via the MOM scheme described in Eq. (6.6). This allows us to readily compare the vortex-modified propagators across all ensembles.

Based on the findings of Ref. [15], we also consider renormalising the vortex-modified propagators via a best-fit approach. To do this, we consider taking a linear combination of the vortex-only and vortex-removed bare renormalisation functions, $Z_{\mathrm{bare}}^{\mathrm{VO}}(q^2)$ and $Z_{\mathrm{bare}}^{\mathrm{VR}}(q^2)$ respectively, such that the "reconstructed" propagator

$$Z^{\mathrm{recon}}(q^2) = \frac{\zeta^{\mathrm{VO}}\, Z_{\mathrm{bare}}^{\mathrm{VO}}(q^2) + \zeta^{\mathrm{VR}}\, Z_{\mathrm{bare}}^{\mathrm{VR}}(q^2)}{Z_3^{\mathrm{UT}}} \tag{6.7}$$

is fit to $Z^{\mathrm{UT}}(q^2)$ via a linear least-squares fit. Here, ζ^{VO} and ζ^{VR} are fit parameters defined such that the renormalised vortex-modified propagators are

$$Z^{\mathrm{VO}}(q^2) = \frac{\zeta^{\mathrm{VO}}}{Z_3^{\mathrm{UT}}}\, Z_{\mathrm{bare}}^{\mathrm{VO}}(q^2)\,, \tag{6.8}$$

$$Z^{\mathrm{VR}}(q^2) = \frac{\zeta^{\mathrm{VR}}}{Z_3^{\mathrm{UT}}}\, Z_{\mathrm{bare}}^{\mathrm{VR}}(q^2)\,. \tag{6.9}$$

Fitting the reconstructed propagator is subject to the constraint

$$Z^{\mathrm{recon}}(\mu^2) = Z^{\mathrm{UT}}(\mu^2) = 1\,, \tag{6.10}$$

so that the MOM scheme is replicated in the fit. This reduces the fit to a single parameter, as we can constrain e.g. ζ^{VR} to be

$$\zeta^{\mathrm{VR}} = \frac{Z_3^{\mathrm{UT}} - \zeta^{\mathrm{VO}}\, Z_{\mathrm{bare}}^{\mathrm{VO}}(\mu^2)}{Z_{\mathrm{bare}}^{\mathrm{VR}}(\mu^2)}\,. \tag{6.11}$$

Once a fit is found, the renormalisation defined in Eqs. (6.8, 6.9) is applied such that the reconstructed propagator is simply given by the sum

$$Z^{\mathrm{recon}}(q^2) = Z^{\mathrm{VO}}(q^2) + Z^{\mathrm{VR}}(q^2)\,. \tag{6.12}$$

As we shall see, this fitting approach is appealing as it produces excellent agreement between the pure-gauge untouched propagator and the reconstructed propagator as defined in Eq. (6.7).

To improve the lattice gluon propagator and suppress lattice cutoff artefacts, we follow the analysis of Refs. [15, 53, 147]. A momentum half-cut and a cylinder cut of radius $2a$ are performed. This removes points where one direction dominates the off-diagonal signal. $Z(3)$ averaging [147] is also employed, which exploits the symmetry of the scalar propagator by averaging over values obtained from points with the same Cartesian radius.

6.1.2 Results

We first present the pure-gauge calculation of the scalar propagator, with all results renormalised using the untouched renormalisation constant, Z_3^{UT}. The results from the three ensembles, UT, VO and VR are shown in Fig. 6.1. As expected, these results agree with those of Ref. [15], with the untouched propagator defined by an infrared peak and an ultraviolet plateau to tree-level. The vortex-modified counterparts qualitatively capture these two features, with the vortex-only propagator featuring an infrared peak, whereas the vortex-removed results retain the ultraviolet plateau. However, there is still significant infrared strength present in the vortex-removed propagator, which indicates that some long-range physics remains in the vortex-removed ensemble.

We now consider the dynamical ensemble with the heaviest pion mass. We plot the gluon propagator calculated on this ensemble in Fig. 6.2. We observe that even at this unphysically large pion mass, the impact on the propagator is significant. Qualitatively, the propagators retain the same features as described for the pure-gauge sector, however the untouched propagator is noticeably screened, as is to be expected

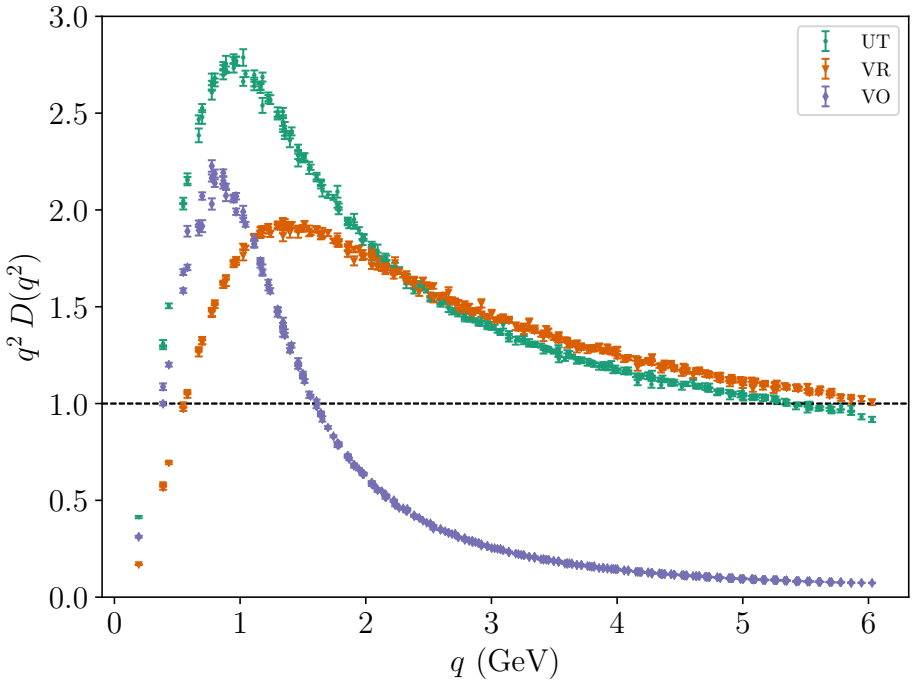

Fig. 6.1 Pure-gauge gluon propagator as calculated on the untouched (green), vortex-removed (orange) and vortex-only (purple) ensembles. All propagators a renormalised by applying the renormalisation constant found by applying the MOM scheme to the untouched propagator. A black line at $Z(q^2) = 1$ is used to show the asymptotic behaviour.

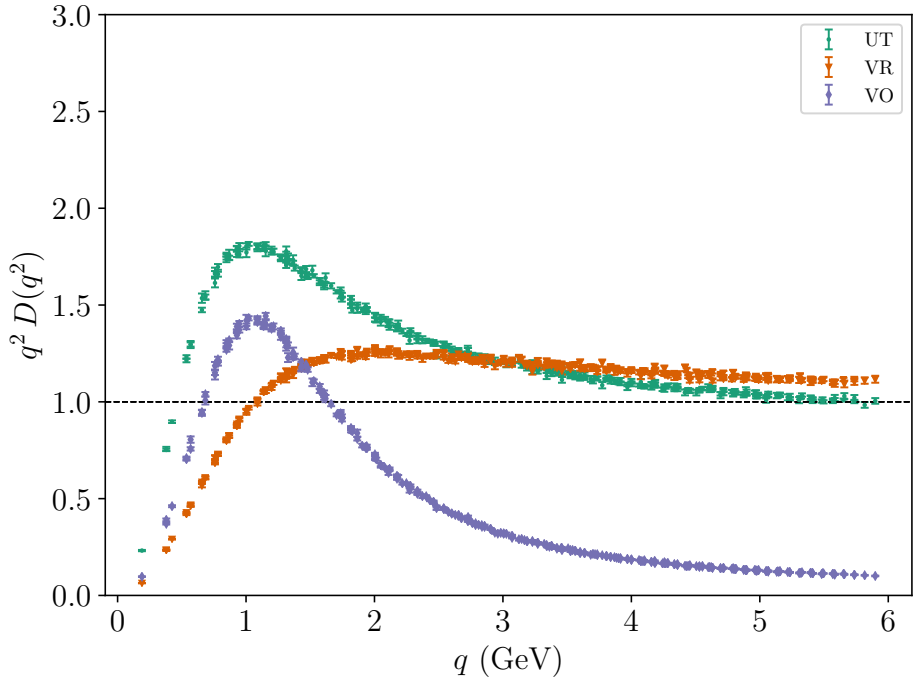

Fig. 6.2 $m_\pi = 701$ MeV gluon propagator. The data scheme is as described in Fig. 6.1.

from the introduction of dynamical fermions [138]. The vortex-only propagator also exhibits screening, which is a heretofore unseen effect. Furthermore, the infrared enhancement of the vortex-removed propagator is significantly reduced when compared to the pure-gauge results shown in Fig. 6.1, and now displays behaviour completely consistent with the perturbative expectation. These two changes indicate a noticeable shift in the behaviour of the centre vortices under the introduction of dynamical fermions.

The story is similar for the results of the lightest pion mass, shown in Fig. 6.3. Screening effects are further enhanced in the untouched propagator as the pion mass is reduced, although it is difficult to observe any change in screening in the vortex-only propagator. To aid in this, we plot a comparison of the vortex-only propagators across all three ensembles in Fig. 6.4. Here we can clearly see the presence of screening upon introduction of dynamical fermions. Between the two dynamical ensembles, screening effects are slightly enhanced as the pion mass decreases, however the effect is very subtle. The vortex-removed propagator also retains the suppression of infrared enhancement found at $m_\pi = 701$ MeV. Given that the behaviour of the vortex-modified propagators is so similar between the two pion masses, it appears that the mere presence

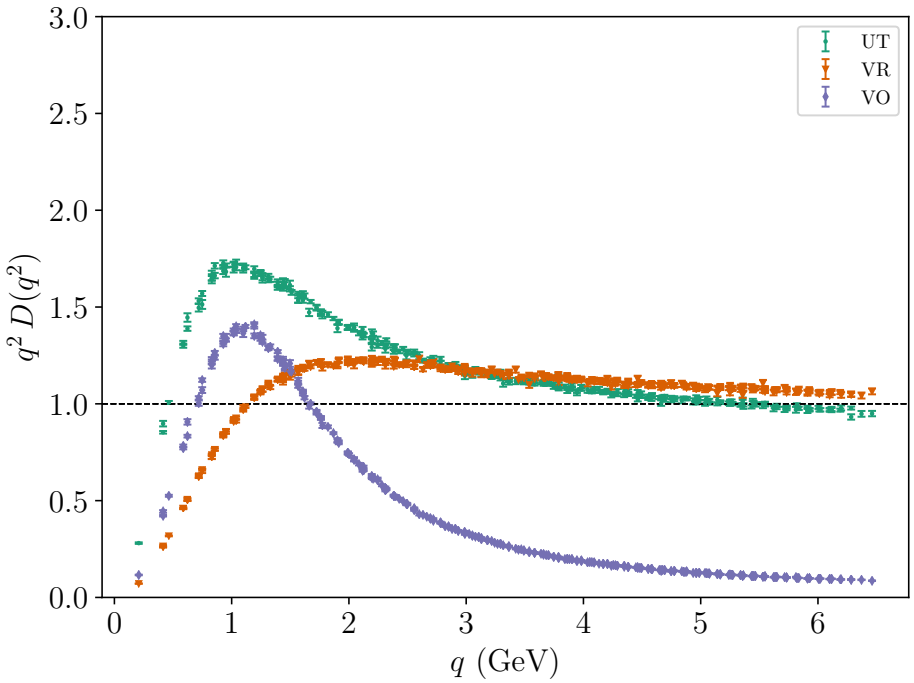

Fig. 6.3 $m_\pi = 156$ MeV gluon propagator. The data scheme is as described in Fig. 6.1.

of dynamical fermions plays a substantial role in altering centre vortex structure and the manner in which they generate the gluon propagator.

An interesting trend in the results presented in Figs. 6.1, 6.2 and 6.3 is the fact that the vortex-removed results exceed the untouched results at high momentum with the same renormalisation constant applied. It is well understood that a larger renormalisation constant is necessary to account for increased roughness in an ensemble [148]. Given that the vortex removal process represents a significant change in the texture of the gauge field, it appears that such roughness has been induced in the vortex-removed fields. This finding supports the need for more detailed consideration of the renormalisation of the vortex-modified propagators.

We now repeat the above presentation but with the second renormalisation method applied, as defined at the end of Sec. 6.1.1. The pure-gauge results are presented in Fig. 6.5. The shape of the propagators is naturally the same as before, with the interesting addition from the renormalisation method being the reconstructed propagator. Here we observe good agreement between the untouched and reconstructed propagators. This indicates that the additional degree of freedom in the renormalisation method is to some extent encapsulating the manner in which the untouched propagator is partitioned into its vortex-modified components.

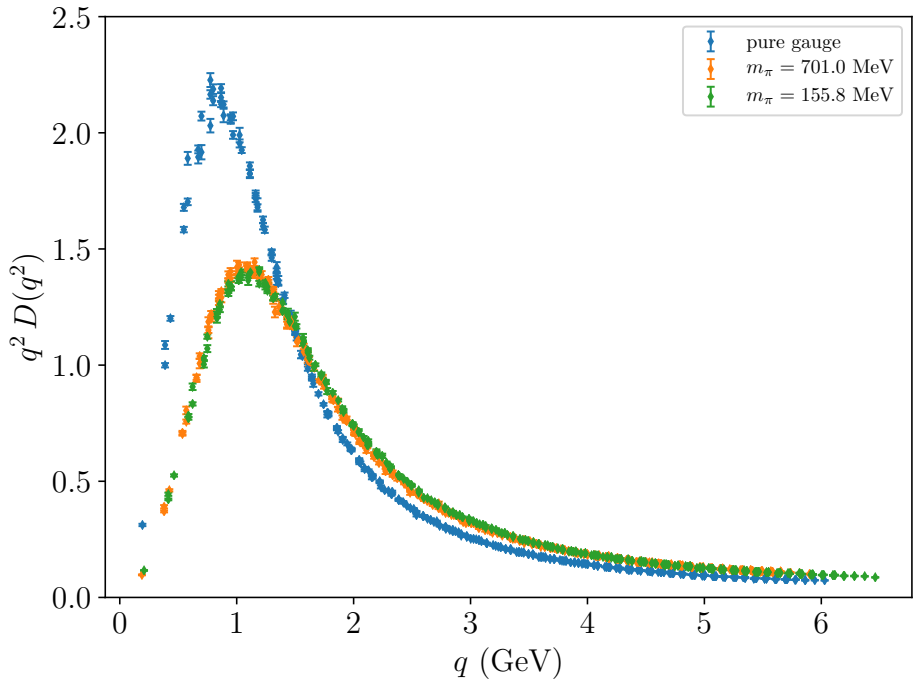

Fig. 6.4 The vortex-only propagators from all three ensembles. Screening is distinctly visible as we transition from pure-gauge to dynamical gauge fields.

Table 6.1 The MOM scheme renormalisation constants, Z_3^{UT}, as well as the fitted renormalisation constants defined in Eq. (6.7).

Ensemble	Z_3^{UT}	ζ^{VO}	ζ^{VR}
Pure gauge	7.112	0.5543	0.8985
$m_\pi = 701$ MeV	9.316	0.6916	0.8251
$m_\pi = 156$ MeV	11.510	0.5834	0.8780

The dynamical ensembles with this renormalisation method applied show a reduced agreement between the untouched and reconstructed propagators relative to the pure gauge results. The significance of this disagreement is unknown, and represents another interesting shift in behaviour when transitioning from pure-gauge to dynamical QCD. The fit constants as described in Eqns. (6.6) and (6.7) are presented in Table 6.1.

When comparing the vortex-only propagators with this new renormalisation scheme we observe that screening effects remain apparent, as is evident from Fig. 6.8. Furthermore, it is also possible to see a distinct increase in screening behaviour as we transition from the heavy to light pion mass. This suggests that perhaps this renormalisation

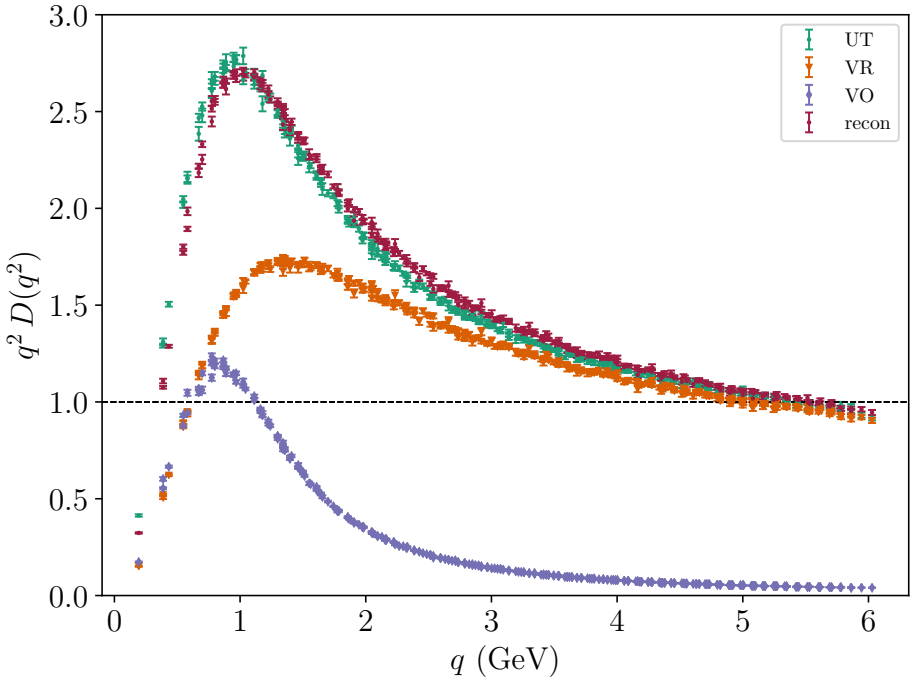

Fig. 6.5 Pure-gauge gluon propagator. All propagators are renormalised by applying the renormalisation method described at the end of Sec. 6.1.1. The "recon" data (red) is an attempted reconstruction of the original propagator by summing the vortex-only and vortex-removed propagators.

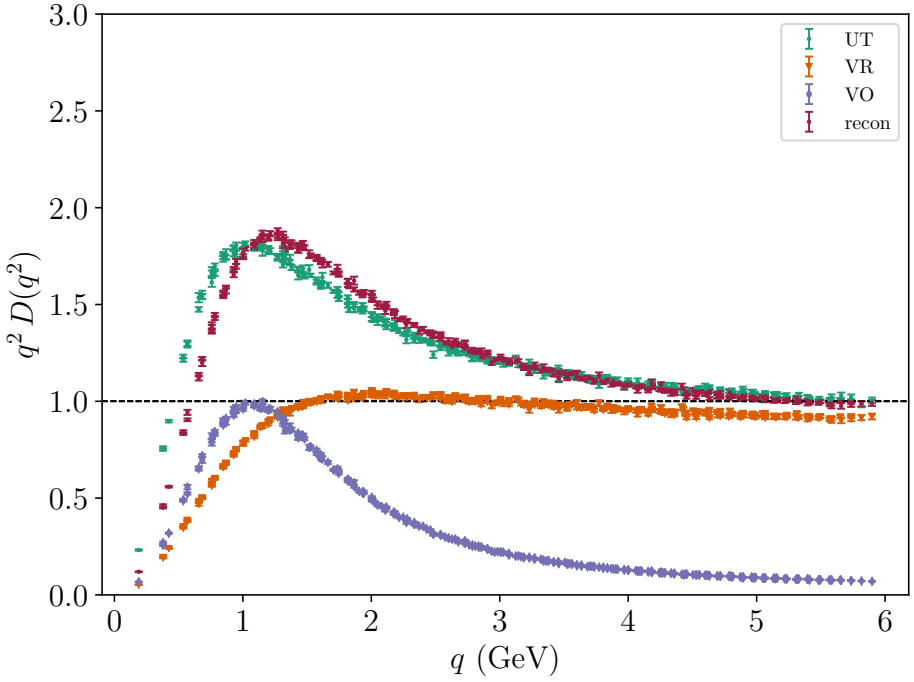

Fig. 6.6 $m_\pi = 701$ MeV gluon propagator. The data scheme is as described in Fig. 6.5.

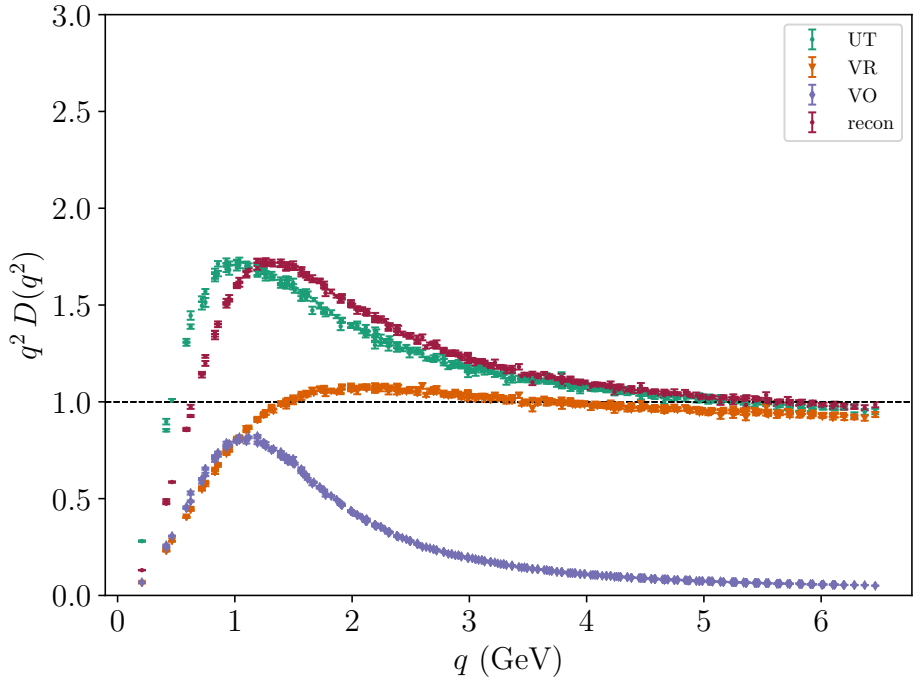

Fig. 6.7 $m_\pi = 156$ MeV gluon propagator. The data scheme is as described in Fig. 6.5.

method is more representative of the relative contributions of the vortex-only and vortex-removed propagators to the untouched propagator.

In summary, the vortex-modified propagators undergo significant changes in behaviour upon the introduction of dynamical fermions. Residual infrared strength present in the pure-gauge vortex-removed propagator is suppressed in full QCD. The vortex-only propagators effectively capture screening effects manifesting as suppressed infrared enhancement, indicating that the long-range behaviour of the vortex-only fields mirrors their untouched counterparts. Best-fit renormalisation provides further insight into the structure of these vortex fields, where we find that the sum of vortex components reconstructs the original propagator to a fair degree. This further supports the idea that the vortex-only and vortex-removed propagators embody a splitting of the vacuum into long- and short-range strength respectively.

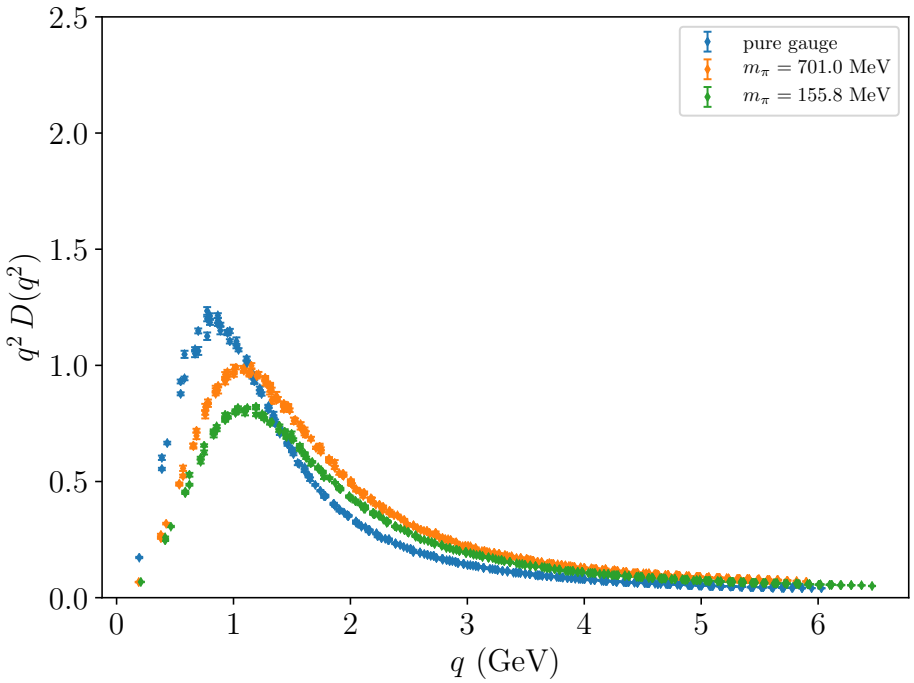

Fig. 6.8 The vortex-only propagators from all three ensembles. The best fit renormalisation method produces a greater distinction between vortex-only propagators compared to Fig. 6.4.

6.2 Positivity Violation

6.2.1 Discussion

For an arbitrary two-point function $D(x-y)$ to represent correlations between physical particles in the sense of a Wightman quantum field theory [149], it is necessary by the Osterwalder-Schrader axioms [150] for $D(x-y)$ to satisfy

$$\int d^4x\, d^4y\, f^*(-x_0, \mathbf{x})\, D(x-y)\, f(y_0, \mathbf{y}) \geq 0\,, \tag{6.13}$$

for a suitable complex test function f. If this axiom is satisfied, then the scalar propagator defined in Eq. (6.2) has spectral representation

$$D(p^2) = \int_0^\infty dm^2\, \frac{\rho(m^2)}{p^2+m^2}\,, \tag{6.14}$$

with $\rho(m^2) \geq 0$, known as the Källen-Lehmann representation.

To investigate the behaviour of the spectral representation, we consider the Euclidean correlator, $C(t)$, obtained by taking the Fourier transform of $D(p_0, \mathbf{0})$ as defined in Eq. (6.14) such that,

$$C(t) = \frac{1}{2\pi}\int_{-\infty}^{\infty} dp_0 \int_0^\infty dm^2 \frac{\rho(m^2)}{p_0^2+m^2}\, e^{-ip_0\, t}\,. \tag{6.15}$$

Extending the p_0 integral to the complex plane and employing the residue theorem, one arrives at

$$C(t) = \int_0^\infty dm\, e^{-mt}\, \rho(m^2)\,. \tag{6.16}$$

Clearly if $C(t) < 0$ for any t then $\rho(m^2)$ is not positive definite, and we say that positivity has been violated. This implies that there is no Källen-Lehmann representation as defined in Eq. (6.14), and as such the propagator does not represent a correlation between physical states. Hence, the states do not appear in the physical spectrum. In the context of the gluon propagator, this can be taken as an indication that gluons are confined.

On the lattice [145], the Euclidean correlator, $C(t)$, is given by the discrete Fourier transform of the temporal component of Eq. (6.2),

$$C_{\text{lat}}(t) = \frac{1}{N_t}\sum_{n_t=0}^{N_t-1} e^{-2\pi i n\, t/N_t} D(q_4(n_t)^2)\,, \tag{6.17}$$

where N_t is the lattice extent in the temporal direction and q_4 is the lattice momentum described in Eq. (6.4) and Eq. (6.5). As $D(0)$ is associated with the lowest frequency mode of the propagator, it is a dominant term in Eq. (6.17). As such, it is essential to ensure that finite volume effects are accounted for.

On the lattice, finite volume effects alter the tensor structure of the propagator given in Eq. (6.1) such that it has the general form [145]

$$D^{ab}_{\mu\nu}(q) = \left(\delta_{\mu\nu} - \frac{h_{\mu\nu}(q)}{f\left(q^2\right)}\right) \delta^{ab}\, D\left(q^2\right) , \tag{6.18}$$

where $f(q^2) \to q^2$ and $h_{\mu\nu} \to q_\mu q_\nu$ for large q_μ, but $f^{-1}(q^2)$ is finite at $q = 0$. We define

$$\tilde{h}_{\mu\nu}(q) = \frac{h_{\mu\nu}(q)}{f(q^2)} , \tag{6.19}$$

and note that in the infinite volume limit,

$$\begin{aligned} \tilde{h}_{\mu\mu}(q) &= f^{-1}(q^2)\, h_{\mu\mu}(q) \\ &= \frac{q_\mu q_\mu}{q^2} \\ &= \frac{q^2}{q^2} \to 1 \text{ as } q^2 \to 0 . \end{aligned}$$

However, on a finite volume lattice, $f^{-1}(q^2)$ cannot approach infinity. Since q_μ can take the value of 0 and $f^{-1}(q^2)|_{q^2=0}$ is finite, $\tilde{h}_{\mu\mu} = 0$ for $q_\mu = 0$ in a finite volume. Thus, the extraction of the scalar propagator $D(0)$ from the lattice propagator requires a normalisation different from that of Eq. (6.2).

This change in normalisation can be implemented by noting that the quantity

$$\left(\delta_{\mu\nu} - \frac{q_\mu q_\nu}{q^2}\right) , \tag{6.20}$$

changes in the finite volume of the lattice to

$$\left(\delta_{\mu\nu} - \tilde{h}_{\mu\nu}(q)\right) . \tag{6.21}$$

For $q_\mu \neq 0$, setting $\mu = \nu$ and summing provides

$$\sum_\mu \left(\delta_{\mu\mu} - \frac{q_\mu q_\mu}{q^2}\right) = 4 - 1 = 3 . \tag{6.22}$$

But for $q_\mu = 0$ on the lattice, $\tilde{h}_{\mu\nu}(0) = 0$ and

$$\sum_\mu \left(\delta_{\mu\mu} - \tilde{h}_{\mu\mu}(q)\right) = 4\,. \tag{6.23}$$

This results in

$$D^{aa}_{\mu\mu}(0) = 4\,(n_c^2 - 1)D(0)\,, \tag{6.24}$$

as opposed to

$$D^{aa}_{\mu\mu}(q) = 3\,(n_c^2 - 1)D(q),\ q \neq 0\,. \tag{6.25}$$

To verify the validity of this factor we explore the behaviour of the ratio of off-diagonal to diagonal propagator components for $q_\mu = 0$, i.e. ratios of the form

$$\frac{D_{\mu\nu}(0)}{D_{\rho\rho}(0)} = \frac{\tilde{h}_{\mu\nu}(0)}{1 - \tilde{h}_{\rho\rho}(0)},\ \mu \neq \nu\,, \tag{6.26}$$

where ρ is not summed. As $\tilde{h}_{\mu\nu} \approx 0$, this ratio provides direct access to $\tilde{h}_{\mu\nu}$ relative to the Kronecker delta of 1.

The values of these ratios calculated on the pure-gauge untouched configurations are shown in Fig. 6.9. It is clear that these ratios are consistent with 0 at $1\,\sigma$, indicating that both the diagonal and off-diagonal components of $\tilde{h}_{\mu\nu}$ are small relative to 1. These results are corroborated by the other ensembles used in this work. This determination justifies the use of a factor of 4 instead of 3 in calculating the scalar propagator at zero momentum to address the impact of the finite volume.

6.2.2 Results

With this understanding developed, it is now possible to calculate $C(t)$ as defined in Eq. (6.17). The results for the pure-gauge ensembles are shown in Fig. 6.10. As expected [138], the untouched correlator shows clear signs of positivity violation. Interestingly, the vortex-only correlators also exhibit robust positivity violation. The positivity violation present in the vortex-removed result at large distances is consistent with the observations made in Fig. 6.1, where residual infrared strength in the vortex-removed gluon propagator is apparent. Thus, the separation of perturbative and non-perturbative physics through vortex modification is imperfect in the pure gauge sector.

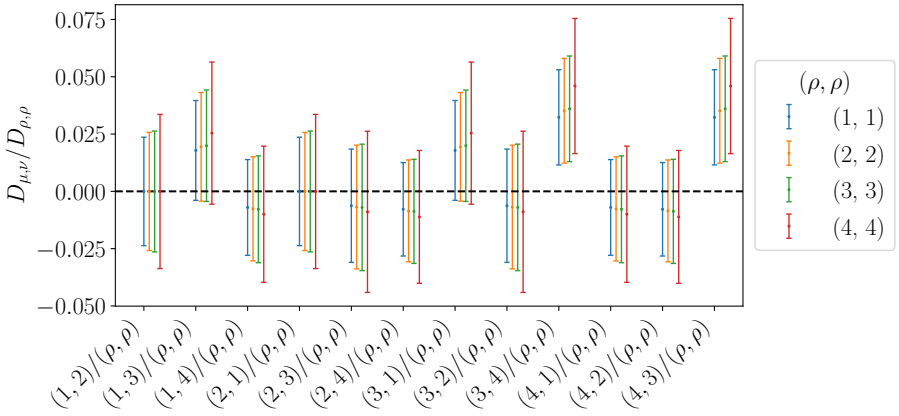

Fig. 6.9 A plot of the 0-momentum ratio of the off-diagonal to diagonal tensor gluon propagator as described in Eq. (6.26). We observe that the majority of values are consistent with zero, indicating that the lattice correction function $\tilde{h}_{\mu\nu} \to 0$ as $q \to 0$.

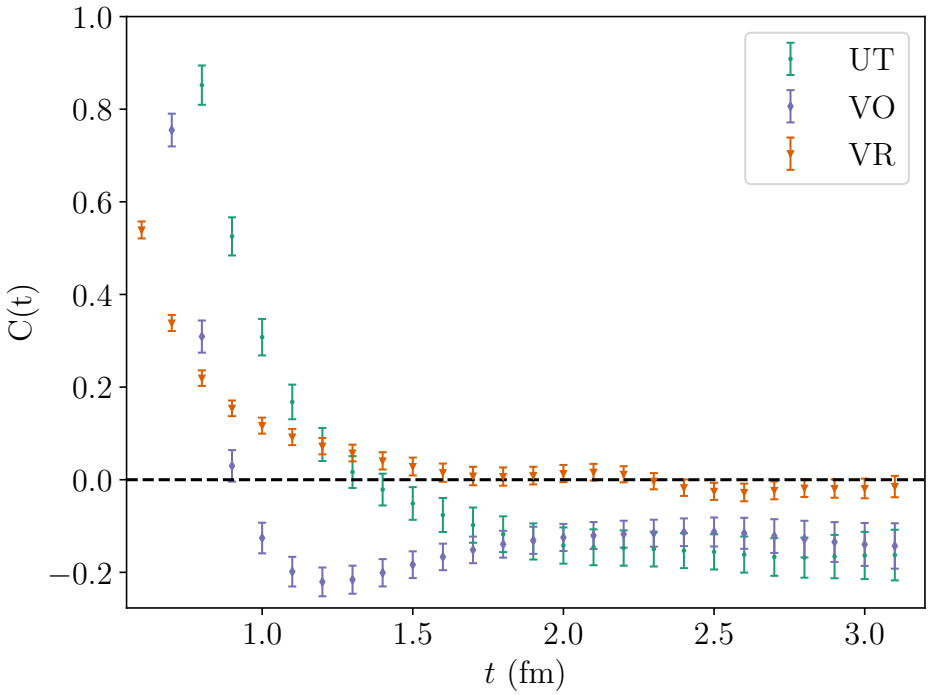

Fig. 6.10 Pure-gauge Euclidean correlator. Shown are the results from the untouched (green), vortex-removed (orange) and vortex-only (purple) ensembles. A dashed line at $C(t) = 0$ is provided to aid in observing positivity violation.

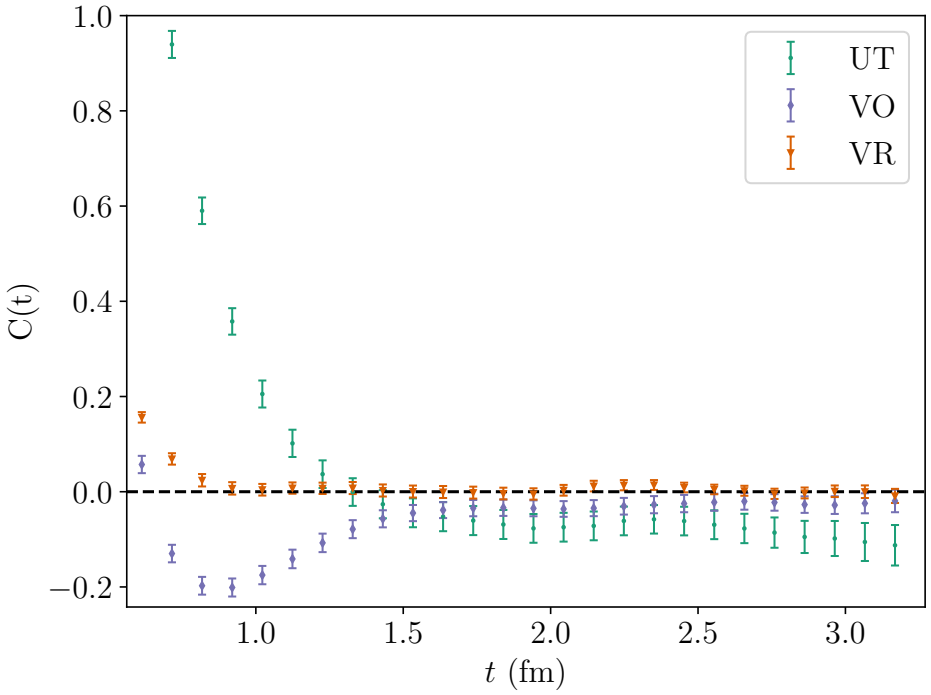

Fig. 6.11 $m_\pi = 701$ MeV Euclidean correlator. Data is as described in Fig. 6.10.

The results from the dynamical ensembles, shown in Figs. 6.11 and 6.12 demonstrate an interesting change in behaviour. Here we observe a similar robust violation of positivity in the vortex-only results as observed on the pure-gauge ensemble. However, the untouched results show a lesser degree of positivity violation, especially on the lightest pion mass ensemble shown in Fig. 6.12. Note however that violation is still present at large times.

As with the gluon propagator results in the previous section, the most striking change is in the vortex-removed correlator. In this sector we now observe consistency with positivity. This supports the interpretation of the positivity violation in the vortex-removed pure-gauge results as being related to the residual non-perturbative infrared strength in the gluon propagator. As this residual strength is significantly diminished on the dynamical ensembles, we now see that the residual q^2 dependence in the VR renormalisation function may be purely perturbative in origin. In this case, vortex modification has been successful in separating perturbative and non-perturbative physics.

In summary, vortex-only configurations exhibit significant positivity violation, as would be expected of a confining infrared-dominated theory. Conversely, the vortex removed configurations show a loss of this positivity violation, admitting the possibility

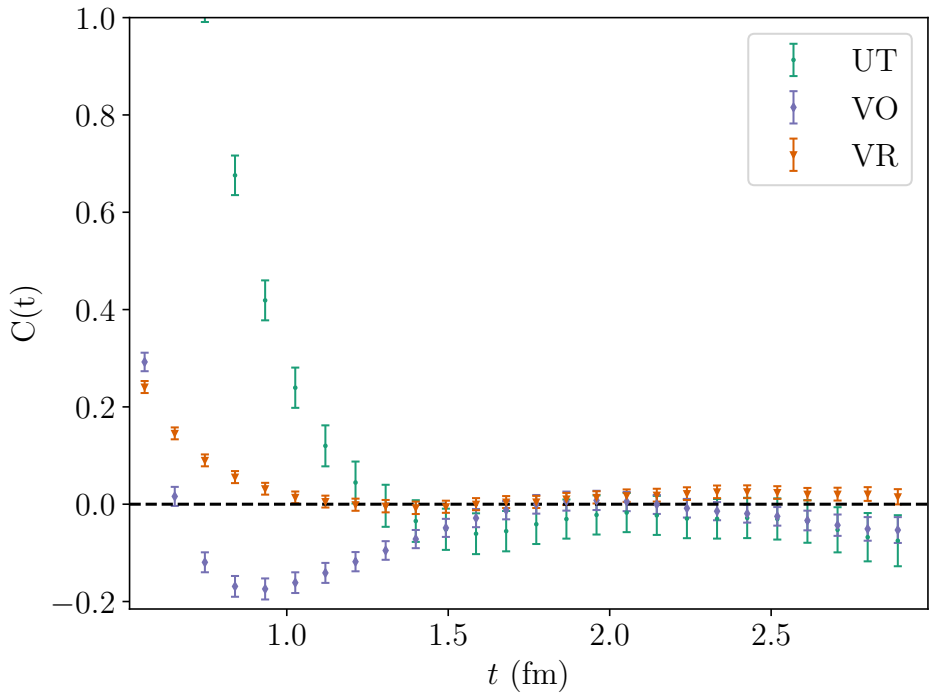

Fig. 6.12 $m_\pi = 156$ MeV Euclidean correlator. Data is as described in Fig. 6.10.

that they do support a spectral representation of the propagator constructed from perturbative gluon interactions. These results provide additional support for the fact that centre vortices encapsulate the confining aspects of QCD.

6.3 Conclusion

The results of this chapter build upon the results of Chapter 5, and provides further insight into the fascinating shift that centre vortices undergo upon the introduction of dynamical fermions. Here we have found that centre vortices in the presence of dynamical fermions are effective in capturing the non-perturbative physics of QCD. Moreover, vortex removal appears to also be far more effective at removing the infrared strength of the propagator.

In regard to positivity violation, we demonstrate the known result that unmodified lattice ensembles give rise to positivity violation in the Euclidean correlator [138]. We then determined that both with and without the presence of dynamical fermions there is clear evidence that vortex-only ensembles exhibit significant positivity violation. On our pure-gauge ensemble, the vortex-removed correlator showed slight positivity

violation at long distances, but on both dynamical ensembles this effect vanished. In full QCD, centre-vortex modification of the ground-state vacuum fields appears to provide an effective separation of perturbative and non-perturbative physics. These results present evidence that centre vortices in the QCD ground-state vacuum fields provide the origin of confinement. It is clear that there is an intimate relationship between dynamical fermions and centre vortices, and that this relationship has significant implications for the QCD vacuum.

Chapter 7

Vortex Structure in the Presence of Dynamical Fermions

This chapter is based on the paper "Centre vortex structure in the presence of dynamical fermions", Biddle, Kamleh, and Leinweber [24]

7.1 Introduction

Given the remarkable change in vortex behaviour brought about by the introduction of dynamical fermions, we now wish to return to the visualisation techniques introduced in Chapter 4 and examine the changes in vortex geometry in the presence of dynamical fermions. We seek to both expand upon and refine the previous methods to explore new aspects of centre vortex structure.

We begin this chapter by looking for changes in the bulk properties of the lattice configurations by analysing the norms and traces of the gauge links, as well as the values of the maximal centre gauge functional. Bulk discrepancies between pure-gauge and dynamical ensembles may suggest where the differences in vortex structure arise from.

The primary new visualisation technique is the development of algorithms that allow us to split the vortex structure into individual disconnected clusters. These clusters may then be rendered in different colours to allow for clear observation of the connectedness of the vacuum vortex structure. Cluster identification also allows for quantitative determination of the degree to which vortices percolate, and whether the

nature of vortex percolation changes under the introduction of dynamical fermions. As with the visualisations presented in Chapter 4, there are interactive 3D models contained in the supplementary material of Ref. [24] that are associated with figures containing (**Interactive**) in the figure caption.

Following cluster identification, we present a novel perspective that considers each cluster as a directed graph of vortex branching points, with the weight of each graph edge corresponding to the number of vortex plaquettes between branching points. This data structure enables us to develop quantitative measures of the size and shape of centre vortex clusters, facilitating a detailed comparison of vortex structure between pure-gauge and dynamical QCD.

This chapter is structured as follows. We present the analysis of the bulk gauge link properties in Sec. 7.2. In Sec. 7.3 we discuss the cluster identification algorithm and subsequent findings. In Sec. 7.4 we introduce the method by which vortex clusters can be converted to a graph, and discuss the analysis performed on these graphs. Finally, the findings of this chapter are summarised in Sec. 7.5.

7.2 Bulk Properties

In understanding the impact dynamical fermions have on the centre-vortex vacuum, it is natural to first look for bulk changes in the $SU(3)$ lattice gauge fields upon the introduction of dynamical fermions. The first measure we examine is the distribution of the local MCG functional

$$\phi_\mu(x) = \frac{1}{n_c^2} \left| \operatorname{Tr} U_\mu^\Omega(x) \right|^2 \tag{7.1}$$

defined such that the total MCG functional given in Eq. (3.14) can be written as

$$\Phi = \frac{1}{V\, N_{\text{dim}}} \sum_{x,\,\mu} \phi_\mu(x) \tag{7.2}$$

The distribution of $\phi_\mu(x)$ values is presented for the untouched ensembles in Fig. 7.1.

We observe that the pure gauge ensemble achieves a typically larger value of $\phi_\mu(x)$, indicating that the links have been brought closer to the centre of $SU(3)$. The two dynamical ensembles follow each other rather closely, although the heavier pion mass appears to achieve slightly larger Φ values than its lighter counterpart. It should be

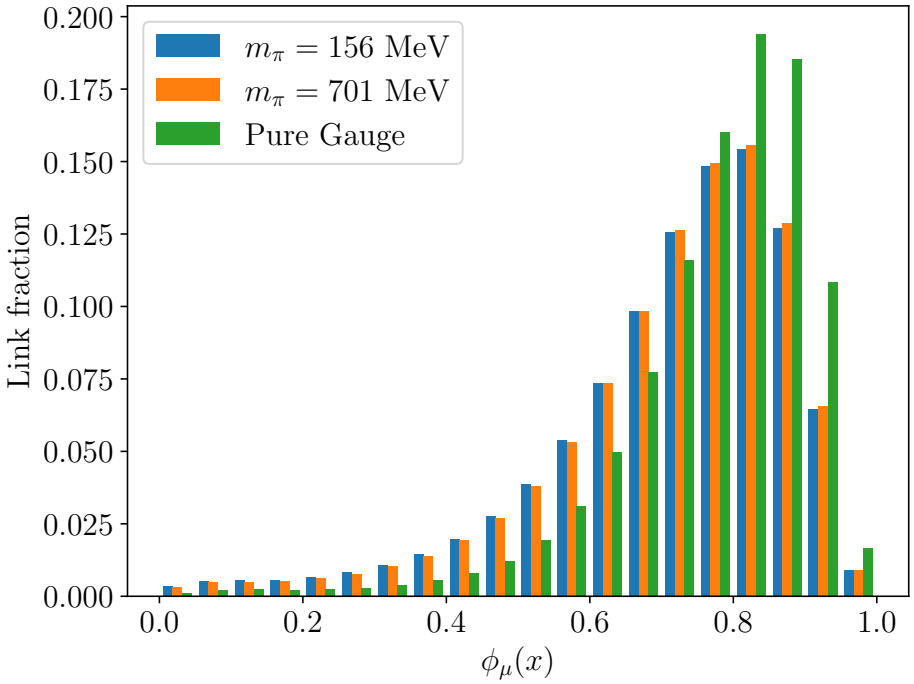

Fig. 7.1 Distribution of the local maximal centre gauge functional, $\phi_\mu(x)$, as defined in Eq. 7.1.

noted however that larger values of $\phi_\mu(x)$ do not necessarily indicate that the MCG algorithm has performed better on these ensembles. As was determined in Refs. [16, 126, 151], there are a number of methods that can be used to increase the typical values of $\phi_\mu(x)$ obtained from maximal centre gauge. However, these methods do not necessarily improve the vortex-finding abilities of the procedure and in some cases actually degrade the vortex-finding performance. As such, it should be understood that the results presented in Fig. 7.1 are simply showing a noticeable change in behaviour as we transition from pure gauge to dynamical ensembles, and not necessarily a worsening of vortex identification.

Next, we wish to compare the distribution of the trace phases, $\arg\left(\operatorname{Tr} U_\mu(x)\right)$, from each ensemble both before and after fixing to maximal centre gauge. These results are presented in Fig. 7.2. As intended, the phases are tightly packed about the three centre values after fixing to maximal centre gauge. However, the pure-gauge results are distributed slightly closer to the centre elements than the dynamical ensembles.

In conjunction with the trace phases, we can also look at the magnitude of the traces, $|\operatorname{Tr} U_\mu(x)|$. These values are presented in Fig. 7.3. Note that a centre element will have $|\operatorname{Tr} U_\mu(x)| = 3$. MCG then clearly serves to not only bring the phases close to

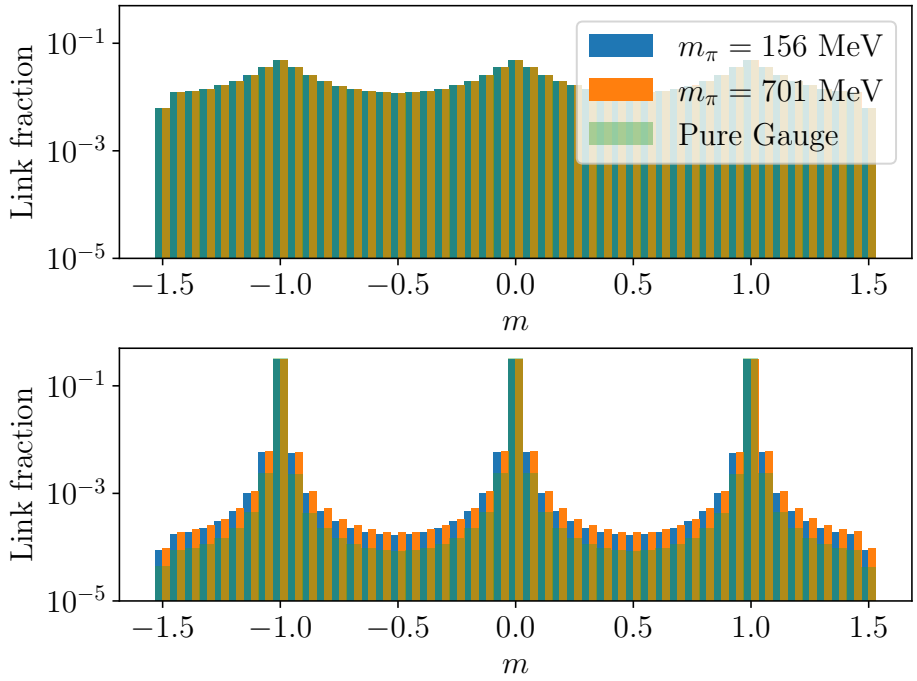

Fig. 7.2 Distribution of trace phases before (**top**) and after (**bottom**) fixing to MCG. We plot the bins for the dynamical ensembles side-by-side as they are similar to one another, with the pure gauge results overlayed.

that of a centre element, but also the magnitude. However, the effect on the magnitude is less than that on the phase. This suggests that there is still significant off-diagonal strength in the original ensembles after fixing to maximal centre gauge. Again, the pure gauge values are distributed closer to the centre value of 3 when compared with the dynamical results.

The next bulk measures we examine are two matrix norms designed to determine the residual off-diagonal strength present in the vortex-removed fields in MCG. The norms are

$$L_\mu(x) = \left(\sum_{i,j} \left| U_\mu^{ij}(x) - \delta_{ij} \right|^2 \right)^{\frac{1}{2}} \tag{7.3}$$

and

$$M_\mu(x) = \left(\sum_{\substack{i,j \\ i \neq j}} \left| U_\mu^{ij}(x) \right|^2 \right)^{\frac{1}{2}} \tag{7.4}$$

We find for the untouched configurations that the results for both norms are identical across all ensembles, as shown in Figs. 7.4 and 7.5. However, after vortex removal we

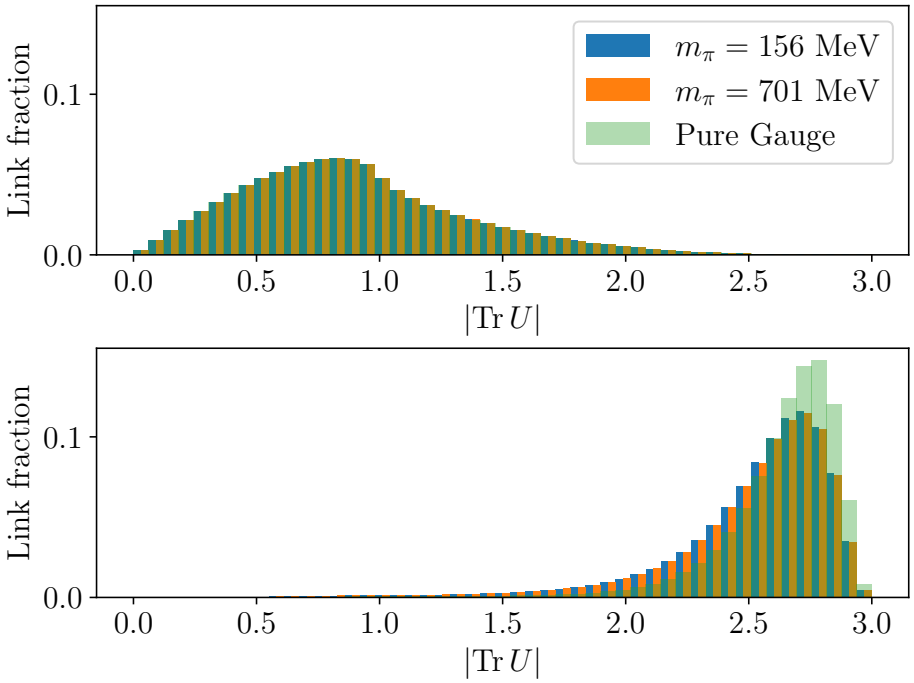

Fig. 7.3 Distribution of trace magnitudes before (**top**) and after (**bottom**) fixing to MCG.

notice that differences appear in both norms. The results for $L_\mu(x)$ and $M_\mu(x)$ on the vortex removed ensembles are shown in Fig. 7.6 and Fig. 7.7 respectively.

We observe that the dynamical ensembles retain a greater proportion of their off-diagonal strength. This is interesting, as it has been shown in Ref. [23] that vortex removal results in a more significant loss of infrared strength in the Landau-gauge gluon propagator when dynamical fermions are present. This indicates that the residual strength as measured by our norms in MCG does not coincide with enhancement as measured via the Landau-gauge gluon propagator.

These measures indicate that there is a substantial difference in behaviour between the pure-gauge and dynamical ensembles when considering their MCG matrix substructure. Both the trace phases and magnitudes are further from the centre elements and the dynamical ensembles retain more off-diagonal strength.

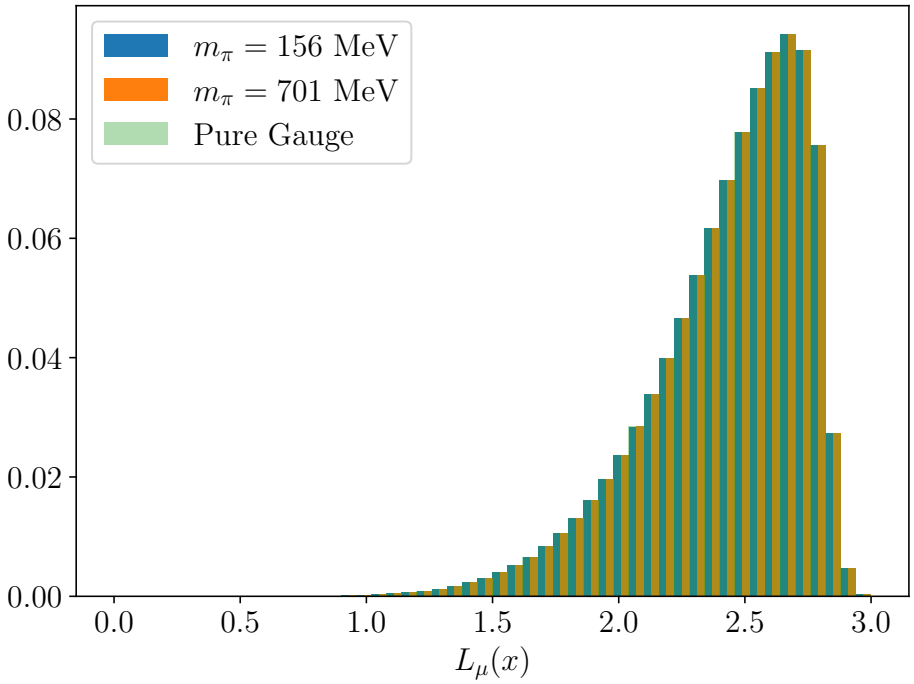

Fig. 7.4 The $L_\mu(x)$ norm calculated prior to fixing to MCG.

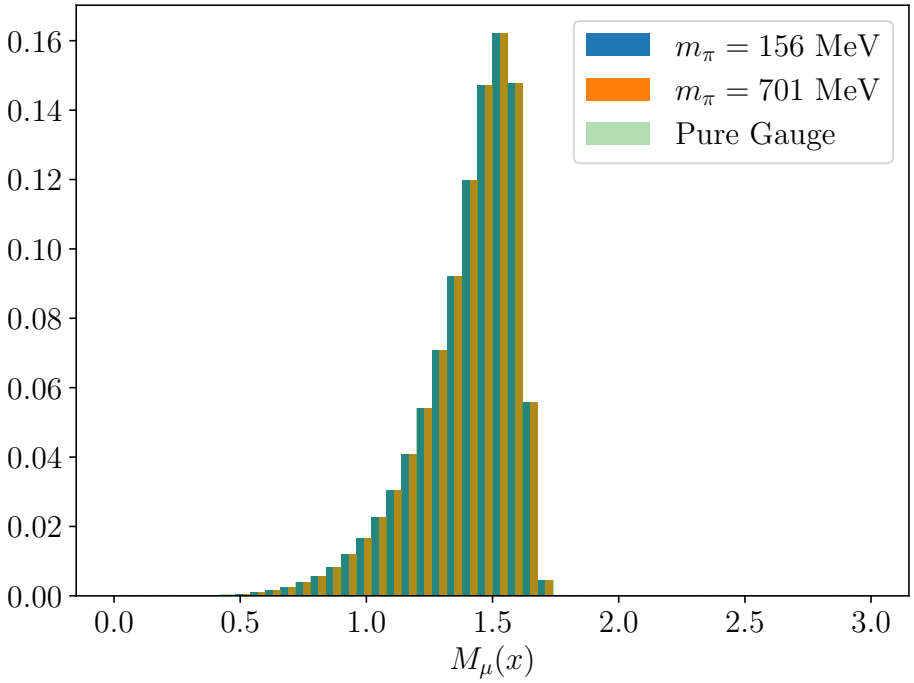

Fig. 7.5 The $M_\mu(x)$ norm calculated prior to fixing to MCG.

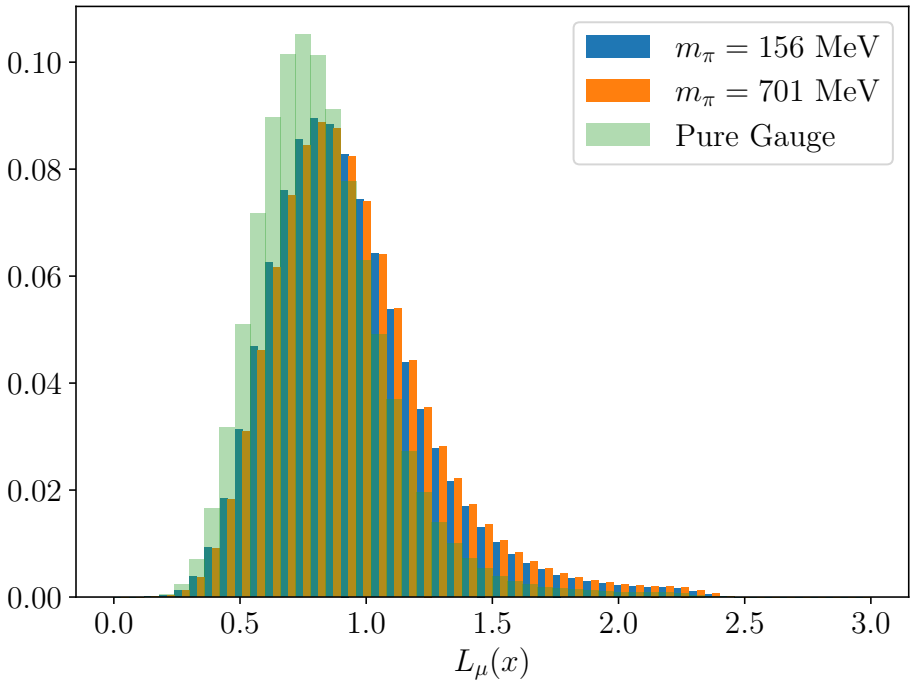

Fig. 7.6 The $L_\mu(x)$ norm calculated on the VR ensembles. Here we see the change in behaviour after the introduction of dynamical fermions.

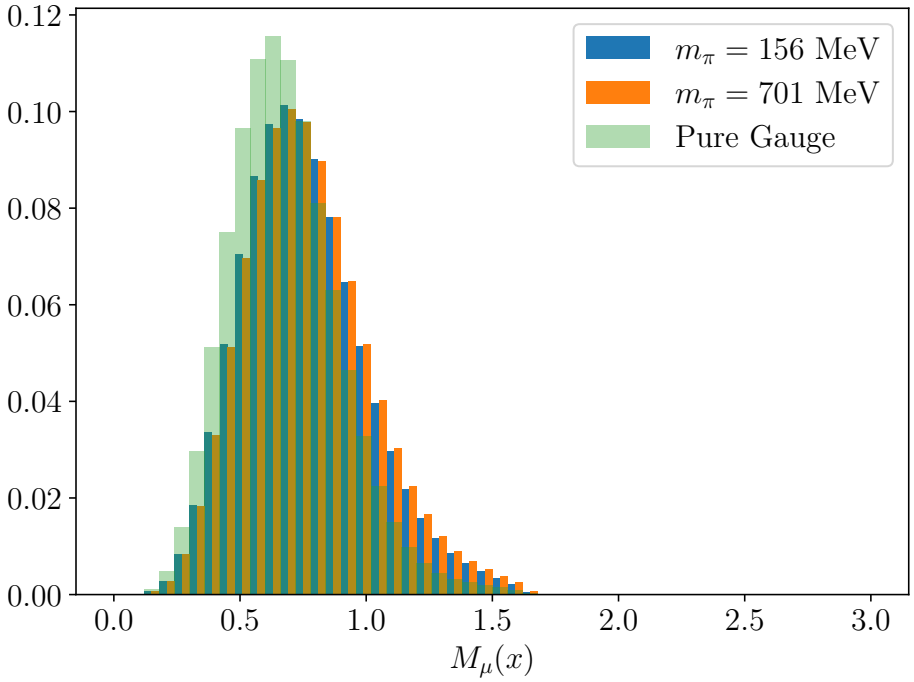

Fig. 7.7 The $M_\mu(x)$ norm calculated on the VR ensembles. A trend similar to that seen in Fig. 7.6 is observed.

7.3 Cluster Identification

It is well known that for $SU(2)$ gauge fields in the confining phase, percolation of centre vortices can be used as an order parameter for the transition from the confined phase to the deconfined phase [8, 63]. At a glance, the visualisations constructed in Chapter 4 support this assessment, with a single large connected vortex cluster clearly visible in each visualisation and only a handful of separate smaller secondary clusters present. Studying the confinement phase transition at the critical temperature will be the subject of future work. However, it is of interest to build the necessary tools to perform such a study. This requires us to quantitatively understand the degree to which a vortex ensemble is dominated by a primary percolating cluster, as opposed to a collection of smaller secondary clusters. To do this, it is necessary to develop an algorithm that can trace these vortex lines and identify disconnected clusters.

Such an analysis is quite straightforward in $SU(2)$, as $SU(2)$ vortices do not permit branching points. This simplifies the algorithm, as each vortex cluster consists of a single line that may be followed until it arrives back at its starting location. In $SU(3)$, vortex branching demands that the algorithm track multiple branching paths, and only terminates when there are no continuations for every path. We describe such an algorithm here.

The starting point for the algorithm is to have all vortices in a 3D slice stored along with their associated tip and base coordinates. With this setup, the algorithm proceeds as follows:

1. Choose an arbitrary vortex to start at. Mark it as visited and record it as belonging to an incomplete line segment.

2. Considering the last vortex in each incomplete line segment, produce a list of all unvisited vortices touching this vortex (both base and tip, accounting for periodicity). Then mark them all as visited

3. Append one of the found vortices to the current segment. For all others, begin a new segment.

4. If there are incomplete segments, repeat from step 2 for each incomplete segment.

5. Once there are no unvisited touching vortices, mark the segment as complete.

6. If all segments are complete, the cluster is complete. Record all vortices in all segments as belonging to this cluster. Return to step 1, selecting an unvisited vortex.

7. If there are no unvisited vortices, all clusters have been identified and the algorithm is complete.

This algorithm can then be applied to each 3D slice to isolate all independent vortex clusters. Employing this algorithm and our visualisation conventions defined in Sec. 4.1, the pure-gauge vortex vacuum on a single slice appears as in top-left panel of Fig. 7.8. As our investigation takes place at zero temperature on a large volume lattice, the choice of slice direction does not impact most intrinsic measurements, and as such we choose to present plots obtained from slicing in the $\hat{x}$ direction. The only notable exception is the size of the percolating cluster as it fills the 3D volume and is therefore smaller for $\hat{t}$ slices. The choice of $\hat{x}$ will be assumed for the remainder of this chapter unless stated otherwise. Numerical values presented in tables will be averaged across all slice dimensions, where applicable.

We observe that indeed the vacuum is dominated by a single primary percolating cluster, with an assortment of small secondary clusters also present. Branching points are readily observed within the visualisation, as can be seen in Fig. 7.9.

The transition to full QCD leads to a marked shift in the behaviour of the centre vortices, as can be seen from the vortex vacuum of the lightest pion mass ensemble shown in the bottom-left panel of Fig. 7.8. The total number of vortices has increased significantly.

The dominance of a single vortex cluster is even more pronounced once it is removed, as shown in the right-hand panels of Fig. 7.8 for the pure-gauge (top) and dynamical-fermion (bottom) slices. Almost all the vortex matter is associated with the percolating cluster. However, if we focus on the dynamical-fermion secondary clusters in the bottom-right panel of Fig. 7.8, we see that the number of secondary clusters has increased substantially when compared to the pure gauge ensemble. Moreover, an increase in the complexity of the secondary structures through branching-point clusters is also evident.

To gauge the relative sizes of the primary and secondary clusters, we calculate the average total number of vortices per slice, N_{slice}, the average number of vortices associated with the primary cluster, N_{primary}, and the average number of vortices associated with a secondary cluster, $N_{\text{secondary}}$. N_{slice}, N_{primary}, and $N_{\text{secondary}}$ for all

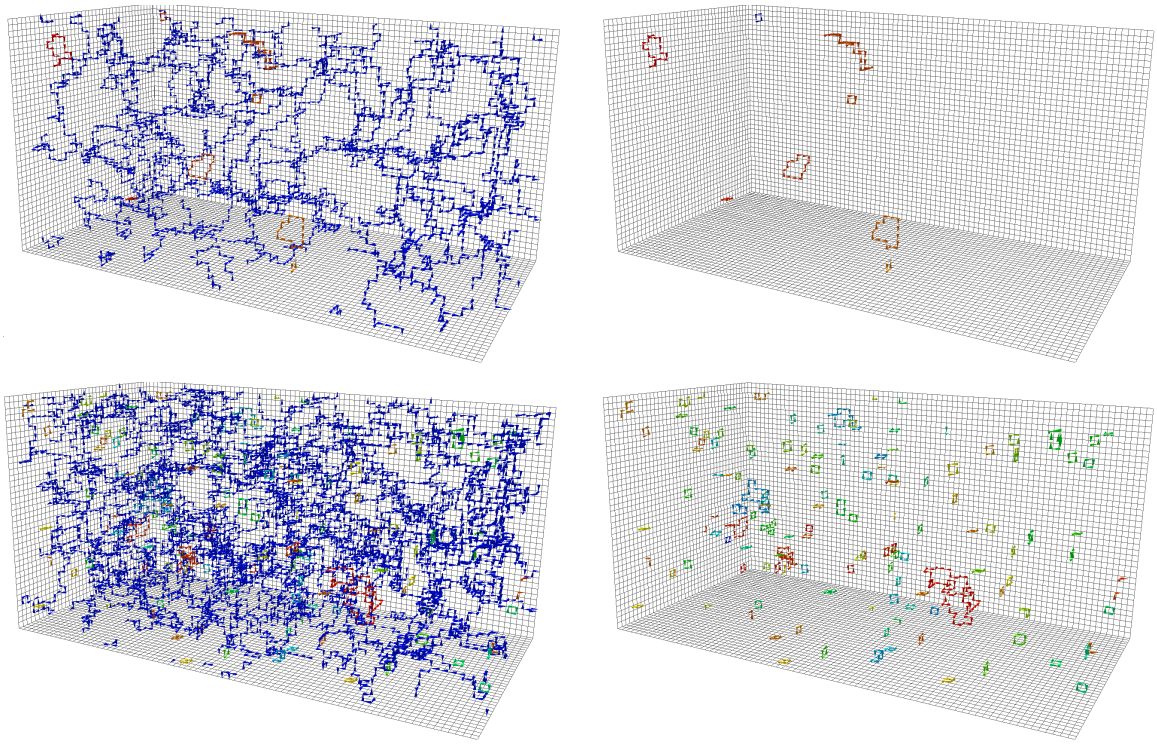

Fig. 7.8 (Top left) The centre vortex structure of a pure-gauge configuration. (Top right) The pure-gauge vortex vacuum as shown in the top left panel with the primary percolating vortex cluster removed. (Bottom left) The centre-vortex structure of a $2+1$ flavour dynamical-fermion configuration from the $m_\pi = 156$ MeV ensemble. (Bottom Right) The dynamical vortex structure in the bottom-left panel with the primary percolating vortex cluster removed. Note the increased abundance of elementary vortex paths and the prevalence of branching points. In each panel, separate vortex clusters are rendered with different colours. These 3D models are generated with AVS scientific visualisation software [152]. (**Interactive**)

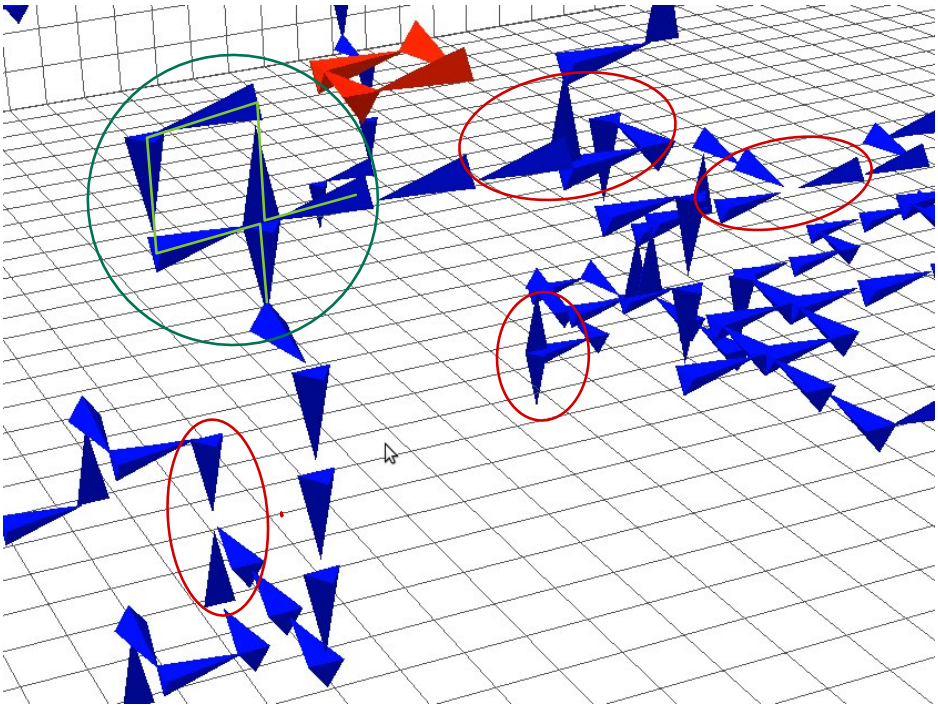

Fig. 7.9 A collection of branching points (red ovals), a touching point (green circle) and a secondary loop (red jets) as they appear in our visualisations. Each jet illustrates the flow of $m = +1$ centre charge.

three ensembles are presented in Table 7.1. Note that the spatial values are obtained by averaging across the three spatial dimensions acting as the slice dimension. When $\hat{t}$ is selected for slicing the four dimensional volume, the spatial volume is half that when a spatial direction is selected. As such, the percolating cluster values in the $\hat{t}$ column are expected to be half those in the spatial slicing column.

Interestingly, we observe that $N_{\text{secondary}}$ decreases in the presence of dynamical fermions, indicating that the secondary clusters are smaller on average. This is due to a proliferation of elementary plaquette vortex paths in dynamical fermion QCD, as illustrated in the bottom-right panel of Fig. 7.8.

We also see that N_{slice} and N_{primary} from the heavier quark-mass ensemble are larger than the values calculated on the light ensemble. This is likely a result of the fact that the heavier pion mass configurations have a slightly larger physical volume. We can determine if this is the case by considering the vortex density, ρ_{vortex}.

The vortex density is calculated by considering the proportion of plaquettes that are pierced by a vortex, P_{vortex}. This is best calculated by first defining an indicator

Table 7.1 The average number of vortices associated with: the total per 3D slice (N_{slice}), the primary cluster (N_{primary}), and a secondary cluster ($N_{\text{secondary}}$), as calculated on the three ensembles. Separate averages are listed for the slicing dimension $\hat{\mu}$ being temporal or spatial.

Measure	$\hat{t}$	$\hat{x}, \hat{y}, \hat{z}$
Pure gauge		
N_{slice}	1673(3)	3347(6)
N_{primary}	1638(3)	3277(6)
$N_{\text{secondary}}$	7.32(5)	7.40(3)
701 MeV		
N_{slice}	3651(4)	7302(8)
N_{primary}	3366(4)	6731(8)
$N_{\text{secondary}}$	5.047(5)	5.057(3)
156 MeV		
N_{slice}	3227(4)	6452(8)
N_{primary}	2964(4)	5926(9)
$N_{\text{secondary}}$	5.011(5)	5.018(3)

function,

$$v_{\mu\nu}(x) = \begin{cases} 1, & P_{\mu\nu}(x) = \exp\left(\frac{\pm 2\,\pi\,i}{3}\right)\, I \\ 0, & P_{\mu\nu}(x) = I\,. \end{cases} \tag{7.5}$$

We then calculate the proportion of pierced plaquettes as,

$$P_{\text{vortex}} = \frac{1}{6\,V} \sum_{\substack{\mu,\,\nu \\ \mu<\nu}} \sum_{x} v_{\mu\nu}(x)\,, \tag{7.6}$$

where the value 6 counts the number of plaquettes associated with site x in four dimensions and $V = N_x\,N_y\,N_z\,N_t$ counts the number of sites in the sum over x. The physical density is then given by,

$$\rho_{\text{vortex}} = \frac{P_{\text{vortex}}}{a^2}\,. \tag{7.7}$$

In the case where the vortex distribution is isotropic, the density derived in four dimensions is equal to the mean of the three-dimensional density when averaged over slices (such as in Fig. 7.8). We can decompose the lattice coordinates into a $1+3$-dimensional notation, $x = (w, \mathbf{x}\,|\,\hat{\mu})$, with w corresponding to the index in the slicing

Table 7.2 The vortex density as calculated on the three ensembles. The proportion of pierced plaquettes, P_{vortex}, the physical vortex density, ρ_{vortex}, the proportion of branching points, P_{branch} and the physical branching point density, ρ_{branch} are presented.

Ensemble	P_{vortex}	ρ_{vortex} (fm^{-2})	P_{branch}	ρ_{branch} (fm^{-3})
Pure gauge	0.017 02(3)	1.702(3)	0.002 49(1)	2.49(1)
701 MeV	0.037 14(4)	3.556(4)	0.008 97(1)	8.41(1)
156 MeV	0.032 82(4)	3.770(5)	0.007 53(1)	9.27(2)

dimension $\hat{\mu}$ and $\mathbf{x}$ specifying the location within the corresponding hyperplane. Then the vortex density for slice w along the dimension $\hat{\mu}$ is

$$P_3(w,\hat{\mu}) = \frac{1}{3\,V_3(\hat{\mu})} \sum_{\substack{i,\,j \\ i<j,\neq\mu}} \sum_{\mathbf{x}} v_{ij}(w,\mathbf{x}\,|\,\hat{\mu})\,, \tag{7.8}$$

where $v_{ij}(w,\mathbf{x}\,|\,\hat{\mu})$ is the restriction of the indicator function in Eq. 7.5 to the relevant slice, $V_3(\hat{\mu})$ is the corresponding 3-volume (e.g. $V_3(\hat{x}) = N_y N_z N_t$), and the division by 3 averages the number of plaquettes associated with each site in three dimensions.

Upon averaging over all w slices in a given dimension and then averaging over the four slice directions, one finds the following for the mean density

$$\bar{P}_3 = \frac{1}{3\,V}\frac{1}{4}\sum_{\mu} \sum_{\substack{i,\,j \\ i<j,\neq\mu}} \sum_{w,\mathbf{x}} v_{ij}(w,\mathbf{x}\,|\,\hat{\mu})\,, \tag{7.9}$$

Noting that each plaquette has been counted twice in the sum over i, j and μ, one recovers P_{vortex} of Eq. (7.6). Of course, in both cases, the physical density is governed by the area of the plaquette as in Eq. (7.7).

The vortex densities from the three ensembles are shown in Table. 7.2. We see that the ρ_{vortex} is indeed larger on the ensemble with the lightest pion mass, indicating a consistent trend of increasing vortex density as the physical pion mass is approached from above.

Another quantity of interest is the branching point density. This is obtained by considering the fraction of elementary cubes within each 3D slice that contain a branching point, P_{branch}. Again, this is best calculated by first considering the indicator function

$$b(x\,|\,\hat{\mu}) = \begin{cases} 1, & n_{\text{cube}}(x\,|\,\hat{\mu}) = 3,5,6 \\ 0, & \text{otherwise}\,. \end{cases} \tag{7.10}$$

The branching point proportion is then given by

$$P_{\text{branch}} = \frac{1}{4\,V} \sum_{\mu} \sum_{x} b(x \,|\, \hat{\mu}) \,, \tag{7.11}$$

where μ sums over all four dimensions. As this density is defined as an average over 3D cubes, the associated physical density is

$$\rho_{\text{branch}} = \frac{P_{\text{branch}}}{a^3} \,. \tag{7.12}$$

The branching point density is shown in Table 7.2. Here we observe that the branching point density follows the same trend as the vortex density, namely that it increases with decreasing dynamical quark mass.

To quantify the change in the behaviour of $N_{\text{secondary}}$ recorded in Table 7.1 we count the number of clusters of a given size and average across slices and the ensemble. These results are shown in Fig. 7.10. There are a number of interesting features present here. Firstly, it is clear that it is not possible to have clusters containing less than four vortices, and that it is also not possible to have five vortices in a cluster. There is an interesting trend that the number of clusters containing an even number of vortices is higher than the number containing an odd number of vortices, especially at small cluster sizes. This results in the alternating comb pattern present in Fig. 7.10. This is a result of the fact that a branching point is necessary for a cluster to contain an odd number of vortices. Hence, this alternating pattern speaks to the presence of a 'cost' associated with a branching point, resulting in clusters containing branching points being less probable than those without. This effect is mitigated as the cluster size increases and the number of vortex arrangements leading to that cluster size increases.

Comparing the different ensembles, we find that the number of clusters at each size on the dynamical ensembles exceed almost all of the pure gauge clusters. However, if we normalise the histogram by the total number of clusters found in the ensemble, as shown in Fig. 7.11, we find that the pure gauge ensembles have a comparable or greater proportion of larger secondary clusters present, perhaps due to the low vortex density. We observe that the dynamical ensembles still retain a larger proportion of the smallest secondary clusters. Interestingly, the alternating even-odd size appears more pronounced in the pure gauge clusters, and persists up to larger cluster sizes. This is suggestive of a lower likelihood of branching in the pure gauge ensembles, which we shall discuss further in Section 7.4.

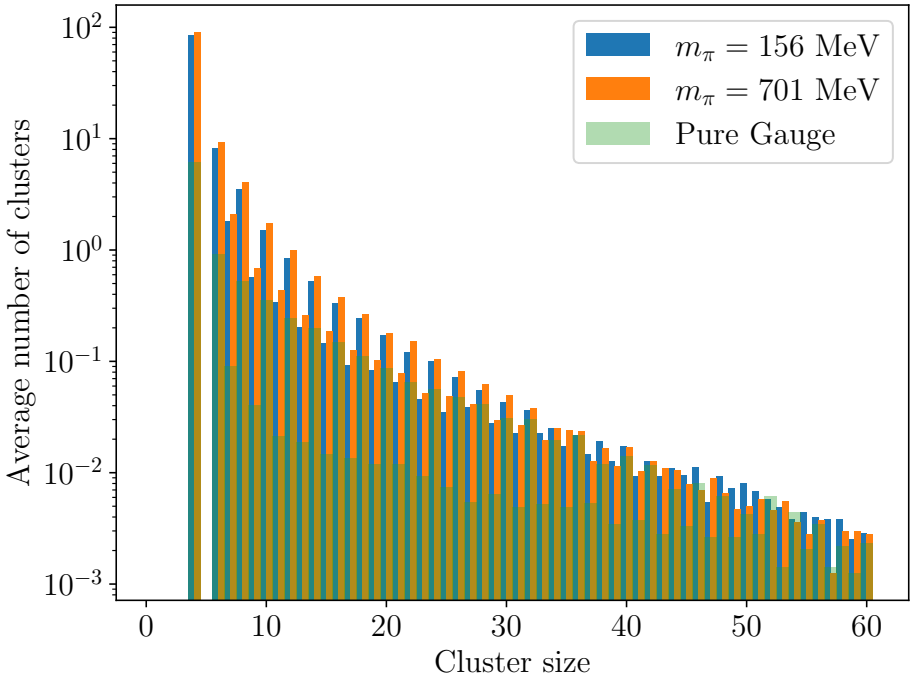

Fig. 7.10 Average number of clusters of a given size per slice, up to a cutoff size of 60.

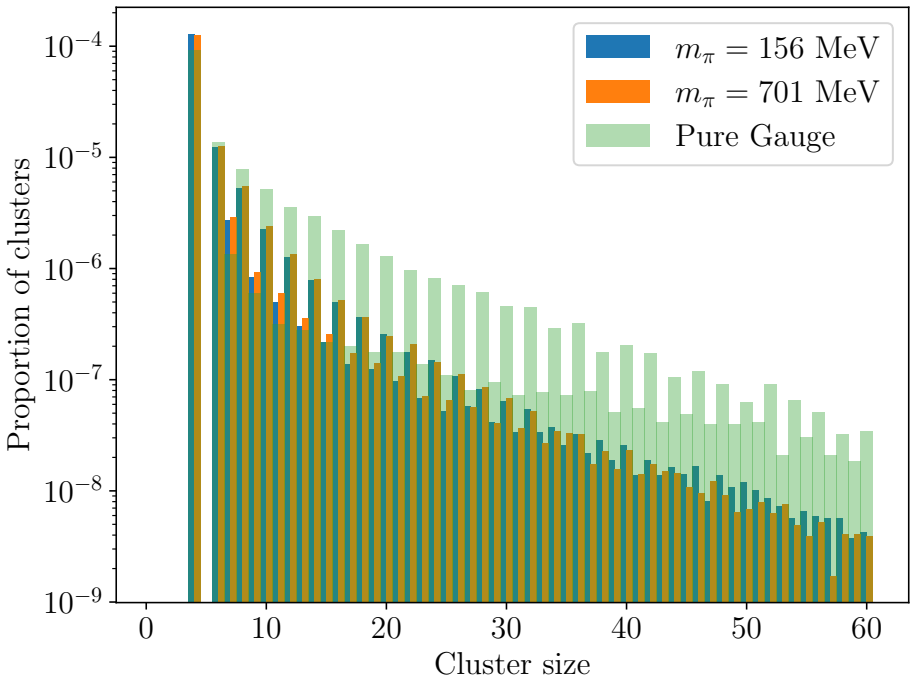

Fig. 7.11 Proportion of clusters of a given size per slice, normalised by the total number of clusters in their respective ensemble.

We can measure the size of a cluster by defining the cluster extent as the largest pairwise distance between vortices belonging to the same cluster, as done in Ref. [63]. The cluster extents are binned, and the content of each bin represents the average number of vortices in the associated cluster, relative to the total number of vortices in the ensemble. The cluster extents are normalised by the greatest distance on a $N_y \times N_z \times N_t$ slice of a periodic lattice,

$$L_{\max} = \sqrt{(N_y/2)^2 + (N_z/2)^2 + (N_t/2)^2}\,. \tag{7.13}$$

The results of this analysis for our three ensembles is shown in Fig. 7.12.

The cluster extents shown in Fig. 7.12 clearly demonstrate that at zero temperature the $SU(3)$ vortex vacuum is dominated by a single percolating vortex cluster, with only a minority of vortices comprising smaller secondary loops. It is expected that this situation will change as the temperature exceeds the critical temperature, as has been observed in $SU(2)$ gauge theory [63]. We also observe that the pure gauge secondary clusters tend to be larger than their dynamical counterparts.

We find that the vortex and branching point density significantly increases upon the introduction of dynamical fermions. However, relative to the total number of vortices present, the pure gauge sector contains a greater proportion of larger secondary clusters than the dynamical case. Aside from the primary vortex cluster, the dynamical vortex vacuum is dominated by an excess of very small secondary clusters. The visualisations reveal significant branching-point complexity in the large secondary clusters of the dynamical-fermion vortex vacuum.

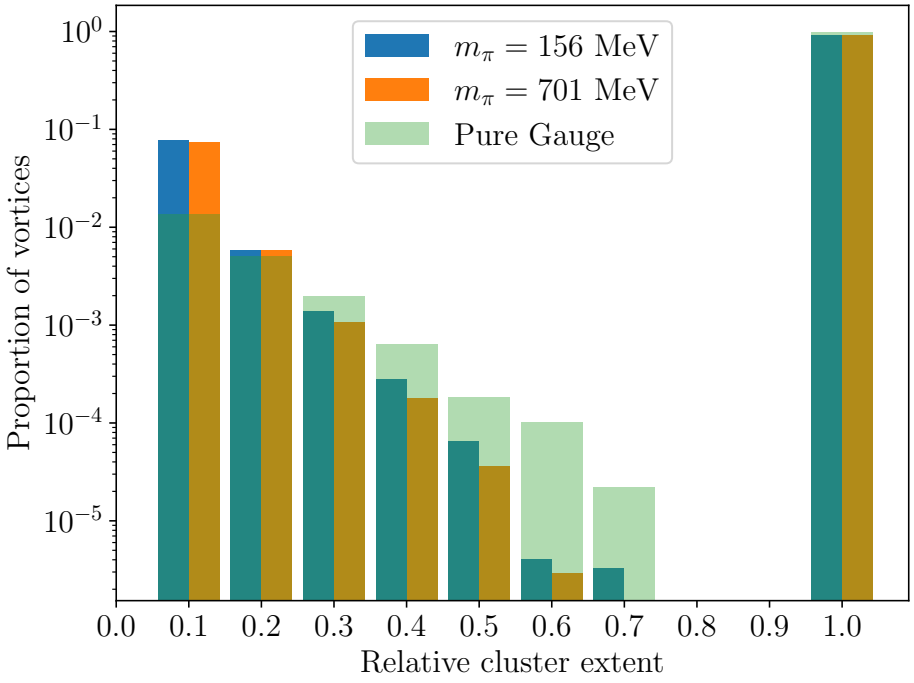

Fig. 7.12 Histogram of the cluster extents relative to $L_{\max}$ for all three ensembles, as described in the text. It is clear that the vortex vacuum at zero temperature is dominated by a single percolating cluster, as can be seen by the dominance of the bin containing the clusters of maximal extent. Bin widths are 0.1 and are centred at the tick marks of the x-axis.

7.4 Branching Point Graphs

The cluster analysis presented in Sec. 7.3 enables us to gain insight into the size of the primary and secondary vortex clusters. It is also of interest to study the relationship between branching points, as these structures are absent in $SU(2)$ where much of the analysis of vortex structure has previously been performed.

Recall that branching points are examined by considering the number of vortices entering and exiting a 3D cube, such that one can define

$$n_{\text{cube}}(x \,|\, \hat{\mu}) = \begin{cases} 0 & \text{No vortex} \\ 2 & \text{regular vortex line} \\ 3, 5, 6 & \text{branching point} \\ 4 & \text{touching point} \end{cases} \tag{7.14}$$

We have already examined the distribution of the possible values of $n_{\text{cube}}(x \,|\, \hat{\mu})$ in Fig. 4.6, and here we repeat this calculation for the three ensembles under consideration. The normalised distribution of values of n_{cube} across the three ensembles is shown in Fig. 7.13. We observe that the distribution of the higher genus values decreases monotonically for all ensembles. The dynamical ensembles feature a greater probability of high-multiplicity branching points. This is consistent with the greater vortex density for these ensembles relative to the pure gauge case, as was determined in the previous section.

To continue our investigation into the structure of centre vortices, it is helpful to abstract the vortex clusters such that we need not be concerned with their precise 3D coordinates. To that end, we seek to represent vortex clusters as a directed graph, with branching points acting as vertices and the edges being given by vortex lines, with each edge weighted by the number of vortices in the line.

The algorithm to perform this graph construction starts with an identified vortex cluster as defined in Sec. 7.3. First, for each vortex we evaluate whether it touches a point with $n_{\text{cube}}(x \,|\, \hat{\mu}) \geq 3$ at its tip, base, both or neither. Each branching or touching point should also have a unique ID. The algorithm proceeds as follows:

1. Find an untraversed vortex with a branching/touching point at its base. If no untraversed vortex can be found, then we are done. Otherwise, set the found vortex to be the current vortex and mark it as traversed. Set the current inter-

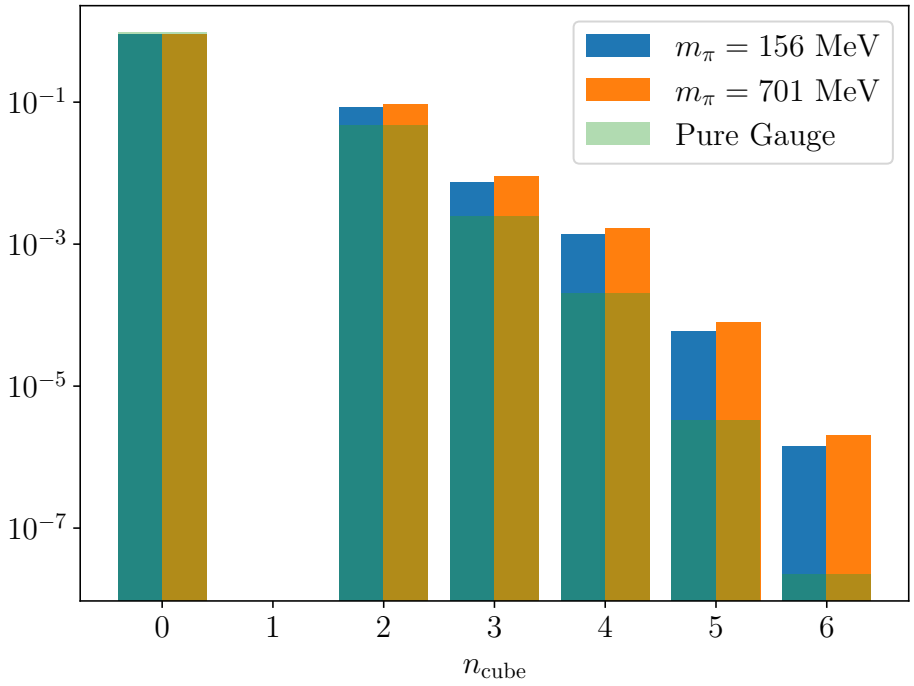

Fig. 7.13 The distribution of branching point genera as defined in Eq. (7.14).

branching point distance to 1 and record the ID of the branching/touching point at the base.

2. Check if the current vortex has a branching/touching point at its tip. If it does, create an edge between the saved branching/touching point ID and the ID of the branching/touching point at the tip with weight equal to the current inter-branching point distance. Return to step 1.

3. Otherwise, find the vortex with its base touching the tip of the current vortex and mark it as traversed. Set the new vortex to be the current vortex and add 1 to the inter-branching point distance. Return to step 2.

The resulting graph encodes the separations between all branching and touching points within a cluster without reference to the specific cluster geometry.

Applying this algorithm to the primary clusters shown in Fig. 7.8 for pure gauge and dynamical vacuum fields, we produce the graphs shown in Figs. 7.14 and 7.15 respectively. These visualisations clearly demonstrate the significant increase in vortices and branching points present on the dynamical configurations.

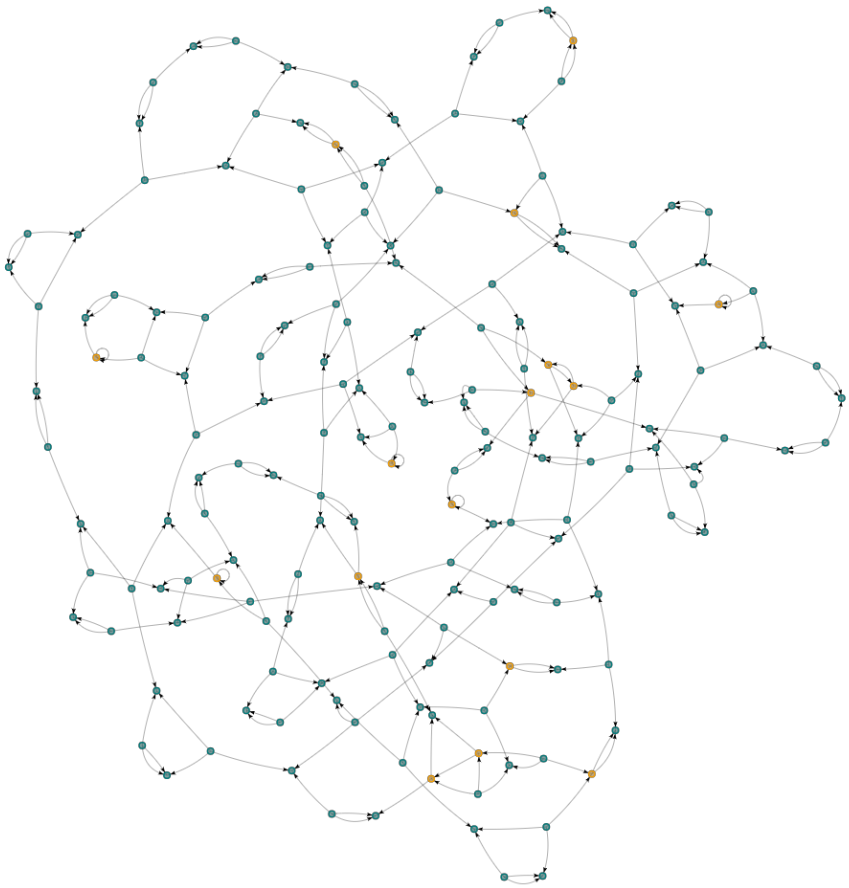

Fig. 7.14 The pure-gauge primary vortex cluster from the slice shown in the top-left panel of Fig. 7.8 rendered as a graph. Branching/touching points are the vertices and connecting vortex lines are the edges. Blue vertices indicate three-way branching points and orange vertices indicate four-way touching points. Visualisations were generated with the Pyvis visualisation package [153].

Table 7.3 The average distance between branching points, d, the same distance in physical units, Δ, the average number of edges per graph, n_{edges}, and the average number of edges per node, $n_{\text{edges}}/n_{\text{nodes}}$.

Ensemble	d	Δ (fm)	n_{edges}	ρ_{edges} (fm^{-3})	$n_{\text{edges}}/n_{\text{nodes}}$
Pure gauge	13.55(2)	1.355(2)	238(1)	4.14(1)	1.538 49(8)
701 MeV	7.691(4)	0.7860(4)	970(1)	15.84(2)	1.586 67(6)
156 MeV	8.082(5)	0.7541(5)	807(1)	17.32(3)	1.583 32(7)

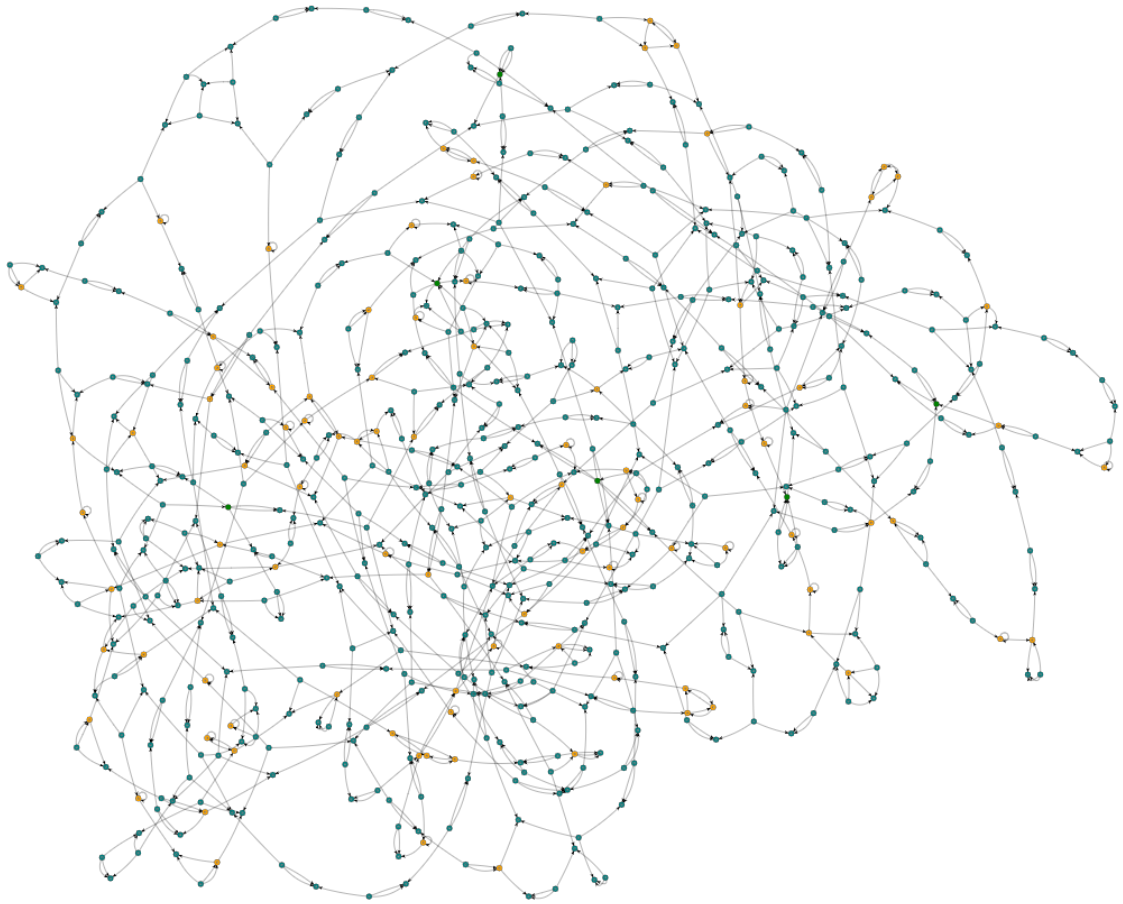

Fig. 7.15 The $m_\pi = 156$ MeV primary vortex cluster from the slice shown in the bottom-left panel of Fig. 7.8 rendered as a graph. Plotting conventions are as described in Fig. 7.14

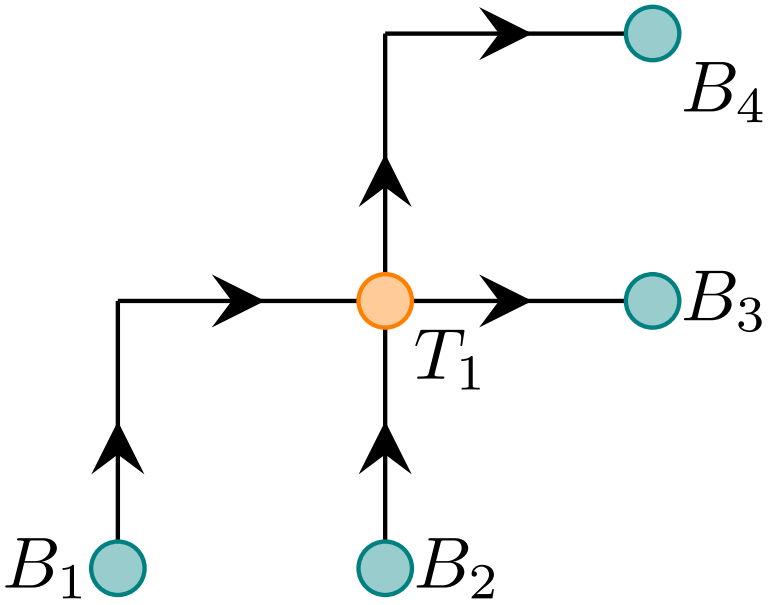

Fig. 7.16 An example of how the touching point T_1 introduces ambiguity into the distance between branching points, B_i. B_1 can connect to either B_3 or B_4, with B_2 then connecting to B_4 or B_3 respectively. This would result in either distances of 4, 2 or 3, 3 being recorded by our algorithm, depending on the order of traversal.

Utilising this new construction, we wish to determine a measure of the separation between connected branching points. A pair of branching points may be connected via multiple vortex lines, and these lines may also pass through touching points that we wish to exclude from the calculation. The presence of these touching points makes it impossible to devise a unique distance between two branching points, as this distance will depend on the manner in which the touching point is traversed, as shown in Fig. 7.16. Instead, we devise an algorithm for calculating the inter-branching point distance that enables a random selection of directions with which to traverse these touching point vertices. The algorithm proceeds as follows.

1. Randomly choose a branching point vertex with untraversed outgoing edges. Record the vertex as the first in a path. Set the current path length to 0. If there is no vertex with an untraversed outgoing edge then we are done.

2. Randomly choose an untraversed outgoing edge to follow to a new vertex. Mark the chosen edge as traversed, add the new vertex to the current path and add its length to the path length.

3. If this edge arrives at a branching point, store the path and the current path length and return to step 1.

4. If the edge arrives at a touching point, repeat from step 2 with the new vertex as the starting vertex.

The end result of this algorithm is a list of paths between branching points that permit the ability to pass through touching points. However, not all edges will be traversed by this method, as the presence of touching points allows for cycles to emerge from these paths. Fortunately, due to conservation of vortex flux, any cycle emerging from a given path will return to that same path. Hence to rectify the algorithm, we simply need to traverse all cycles on a given path and add their length to the existing length. This is done by performing a modified depth-first search on each vertex to traverse any cycles that were omitted from the above method. Pseudocode for this search on a single vertex is as follows:

```
function dfs(this_vertex, path):
  for edge in this_vertex.edges:
    if (edge is not traversed
        and edge is outgoing):
      path.length += edge.length
      edge.traversed = True
      next_vertex = edge.end
      if next_vertex is not this_vertex:
        dfs(next_vertex, path)
```

The path lengths now accurately represent the distance between branching points. This concludes our determination of the branching point separations. Note that because of the inherent ambiguities in the branching point graphs, the solution is not unique. We determine whether the impact of this randomness is significant in the ensemble average choosing a single calculation of the distances as a reference, then repeating the distance calculation nine further times with different random seeds. We then use the Kolmogorov-Smirnov test [154] to determine the equality of the different distributions. We find that the test statistic for all ensembles is of order 10^{-5}, with corresponding p-values consistent with 1. Thus we are satisfied that the variance in this distance measure is negligible in the ensemble average, and we are therefore justified in considering it a useful measure of branching point separation.

The average separation, d, for each ensemble is presented in Table 7.3. The physical separation $\Delta = a\,d$ is also determined. Here we see that there is a consistent trend of decreasing average separation with decreasing pion mass. This coincides with our determination of the branching point and vortex densities, as a higher density suggests a smaller separation between points.

We also present the average number of edges in the graphs, n_{edges}, and the average number of edges per node, $n_{\text{edges}}/n_{\text{nodes}}$ in Table 7.3 as measures of the complexity and structure of the graphs. We observe that, as expected, the number of edges substantially increases upon the introduction of dynamical fermions. The number of edges per node is close to 1.5 for all ensembles, as the majority of edges emerge from a three-way branching point and terminate at another three-way branching point. However, the number of edges per node is larger on the dynamical ensembles, likely due to the increase in vortex density resulting in a higher number of vortex intersections.

The distribution of branching point separations is shown in Fig. 7.17. The results are normalised by the total number of vortex paths considered, such that the histogram has unit area. Apart from an enhancement of the smallest branching point separations, the distances are exponentially distributed. This distribution is consistent with a constant branching probability, *i.e.* the probability of branching at the next link of a vortex chain is independent of the length of the vortex chain.

This supports a previous conjecture for the interpretation of vortex branching [13, 67]: that a vortex can be considered to have some fixed rate of branching as it propagates through space-time. This interpretation allows for vortex branching on the lattice to be considered as a binomial random variable X with some probability of branching, q. Thus, the probability of branching after k lattice plaquettes is given by the geometric distribution

$$P_k = q\,(1-q)^{k-1}\,. \tag{7.15}$$

Typically, one estimates the rate of a binomial random variable by evaluating $q = 1/\bar{X}$, where $\bar{X} = \sum_k k\,P_k$. However, due to the deviations from linearity found at small separations in the log-distributions shown in Fig. 7.17, this measure fails to capture the true rate of branching. To account for this, we instead fit a linear function,

$$f(k) = \alpha - \beta\,k\,, \tag{7.16}$$

to the log of the distribution of branching point separations for $k > 3$. The result of this fit for each ensemble is plotted in Fig. 7.17.

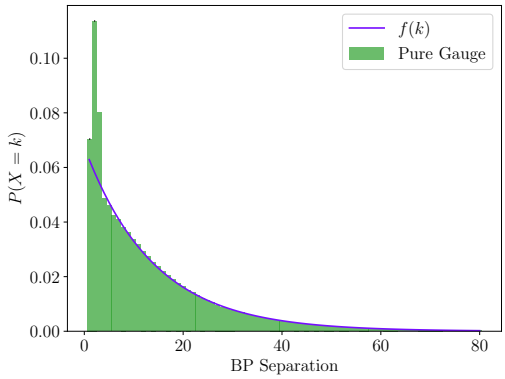

(a) Pure gauge.

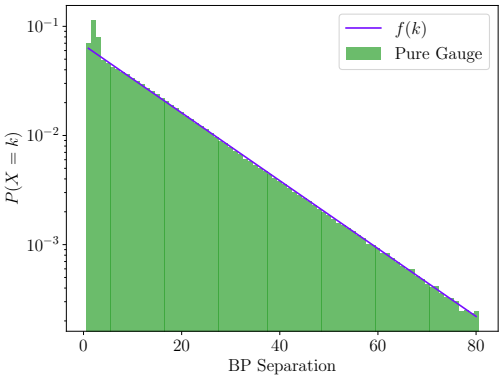

(b) Pure gauge, log scale.

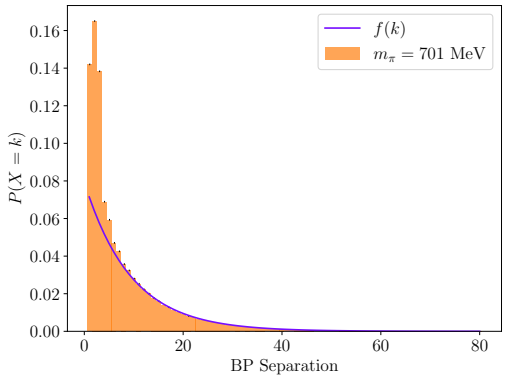

(c) $m_\pi = 701$ MeV.

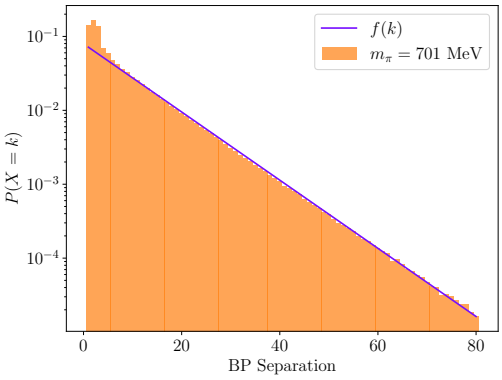

(d) $m_\pi = 701$ MeV, log scale.

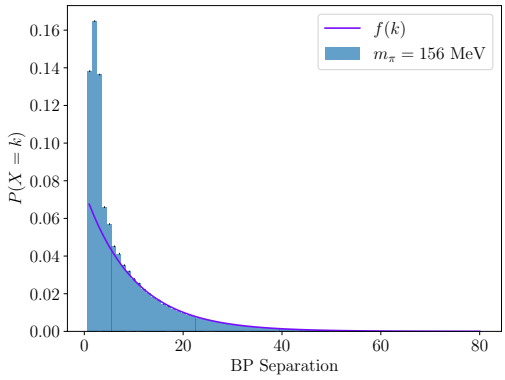

(e) $m_\pi = 156$ MeV.

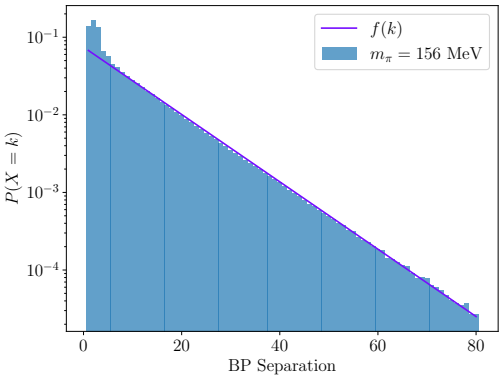

(f) $m_\pi = 156$ MeV, log scale.

Fig. 7.17 Normalised branching point (BP) separations from all ensembles, along with the corresponding fit to $f(k)$ given in Eq. (7.16).

Of course, for a normalised distribution, α is constrained by β. However, the significant non-exponential behaviour for $k \leq 3$ spoils the exponential normalisation constraint. Thus α is introduced to accommodate for this, and we refer to β describing the k dependence to determine the branching probability q.

The parameters of this fit are related to the log of the binomial rate

$$\log(P_k) = \log(q) - \log(1-q) + \log(1-q)\, k = \alpha - \beta\, k\,. \tag{7.17}$$

Equating the coefficients of the terms linear in k, we resolve the branching rate

$$q = 1 - e^{-\beta}\,. \tag{7.18}$$

Note, for small β, $q = \beta$. This rate can be converted to a physical quantity by then considering the rate per unit length, $\lambda = q/a$. All fitted parameters are calculated on 200 bootstrap ensembles, with errors determined via the bootstrap variance.

The rate described above can then be compared to the naive rate, q_{naive}, calculated by considering the number of cubes containing branching points divided by the number of cubes pierced by two or more vortices. Defining

$$c(x \,|\, \hat{\mu}) = \begin{cases} 1, & n_{\text{cube}}(x \,|\, \hat{\mu}) \neq 0 \\ 0, & \text{otherwise}\,, \end{cases} \tag{7.19}$$

and recalling the branching point indicator defined in Eq. (7.10), we define the naive rate to be,

$$q_{\text{naive}} = \frac{\sum_\mu \sum_x b(x \,|\, \hat{\mu})}{\sum_\mu \sum_x c(x \,|\, \hat{\mu})}\,. \tag{7.20}$$

The associated physical quantity is the rate per unit length, $\lambda_{\text{naive}} = q_{\text{naive}}/a$. The calculated rate parameters from both methods are shown in Table 7.4. We observe that with both measures the physical branching rate increases as the physical pion mass is approached. We emphasise, only q contains the detailed information on the path geometry.

The difference between the fitted and naive rates is an interesting finding. The naive rate will include the short-range non-exponential behaviour, inconsistent with a constant branching rate. At larger separations, vortex branching follows a constant rate. However, there are clearly short-range effects that result in clustering of branching points, which in turn necessitates the more sophisticated approach detailed above for

Table 7.4 The naive and fitted branching rates, q_{naive} and q, and their physical counterparts λ_{naive} and λ obtained through the methods described in the text. The fit parameter β is also presented. Only q and λ are associated with a constant branching probability.

Ensemble	q_{naive}	λ_{naive} (fm^{-1})	q	λ (fm^{-1})	β
Pure gauge	0.050 10(6)	0.5010(6)	0.0690(2)	0.690(2)	0.0715(2)
701 MeV	0.085 26(5)	0.8342(5)	0.1005(3)	0.984(3)	0.1059(3)
156 MeV	0.080 62(6)	0.8641(7)	0.0952(2)	1.020(3)	0.1000(3)

q. These clustering effects appear to be amplified upon introduction of dynamical fermions. Whether this clustering radius is a physical effect or the result of finite lattice-spacing effects is an interesting avenue for future study.

It should be noted that whilst the distributions shown in Fig. 7.17 take into account all primary and secondary clusters, the results are minimally affected if the secondary clusters are removed due to the vast majority of branching points belonging to the primary cluster.

An interesting correlation we observe is that the ratio between the pure gauge and dynamical branching rates is similar to the corresponding ratio of the vortex-only string tensions calculated in Chapter 5. The vortex density is naturally correlated with the branching rate. In SU(2) at least, it has been shown through simple combinatoric arguments that the Wilson loop area law and hence the string tension can be related to the density of percolating random vortices [86]. It seems reasonable to infer then that the correlation we observe between the branching rate and string tension ratios is not simply a coincidence but a reflection of the differing structure of the vortex fields in the pure gauge and dynamical sectors.

7.5 Conclusion

In this chapter we have explored of the impact of dynamical fermions on the centre-vortex structure of the vacuum ground-state fields.

Examining the bulk properties of the original gauge fields, we find that dynamical fermions lead to greater off-diagonal strength in the MCG lattice gauge links. The presence of dynamical fermions gives rise to an increased abundance of centre vortices

and branching points, as reflected by the increasing vortex and branching point densities as the physical pion mass is approached.

We construct cluster identification algorithms to identify independent vortex clusters and use this identification to construct visualisations of the vortex vacuum. These reveal that the vacuum is dominated by a single percolating cluster. Our results show that dynamical fermions lead to an abundance of smaller clusters as compared to their pure-gauge counterparts.

We employ a novel method of reducing vortex clusters to directed graphs, with vertices defined by touching points, branching points and the edges connecting them weighted by the number of vortex links. Using this construction, we render the graphs to illustrate the radical change in the number of vortices and branching points after the introduction of dynamical fermions. We define a measure of branching point separation, and observe that the distribution of separations follows an approximate geometric distribution. We estimate the rate of this distribution and find that there is a tendency for branching points to cluster at small separations. For moderate separations, we find the probability of vortex branching increases by approximately 40% upon the introduction of dynamical fermions.

Understanding the role of dynamical quarks in the QCD vacuum continues to be an interesting area of study. The effect of matter fields on the vacuum phase structure has been explored elsewhere within the gauge-Higgs model [134–137]. The extension of these ideas to QCD may shed further light on the nature of confinement. In particular, investigations that further our understanding of string breaking in terms of QCD vacuum structure is desirable.

The findings of this chapter illustrate the substantial impact dynamical fermions have on the geometry and structure of the centre vortex vacuum. This, in conjunction with the results of previous chapters, reinforces the significance of dynamical fermions in developing a complete understanding of the centre vortex picture of QCD.

Chapter 8

Conclusion

The centre vortex model has consistently proven itself capable of capturing the qualitative properties of the non-perturbative regime of QCD. For the first time, we have examined the impact of dynamical fermions on the behaviour of centre vortices, and in doing so discovered an unexpected and remarkable result. The presence of dynamical fermions greatly alters the centre vortex structure and results in not just qualitative, but quantitative agreement between a variety of gluonic observables calculated on the lattice.

In Chapter 4 we constructed novel 3D visualisations of the pure-gauge centre vortex vaccuum. These allowed for an examination of the structure of vortex lines in 3D, as well as visualisations of how vortex lines shift as they propagate through Euclidean time. We also observe that at zero temperature, the vortex vacuum appears to be dominated by a single percolating cluster. We then proceeded to examine the correlation between vortices, branching points and signular points with topological charge density. We determined that there is a positive correlation between regions of high topological charge density and vortex structures. We also observed that smoothing has the effect of removing centre vortices from the lattice, however this process does not increase the correlation with topological charge density. These visualisations also provide the basis for further exploration of centre vortex geometry, as was performed later in this work.

We then transitioned to an entirely new domain of centre vortex exploration in Chapter 5; the impact of dynamical fermions on centre vortices, explored in the context of the static quark potential. Using a variational analysis and newly developed smoothing procedures, we were able to calculate the static quark potential on untouched, vortex-removed, and vortex-only configurations obtained from two dynamical and one

pure gauge ensemble. The pure gauge ensemble replicated the well-established result that centre vortices only capture approximately 62% of the original string tension. However, the presence of dynamical fermions, even at an unphysically large quark mass, leads to a complete shift in the centre-vortex potential. We find that it is possible to fully reproduce the original static quark potential from vortex-only ensembles. We also observe that centre vortices are sensitive to screening, observed as an overall suppression in the string tension as the quark mass decreases.

Motivated by the difficulty of fitting a Coulomb function to the vortex-removed potential, we also explore two modified ansätze that attempt to model the long-range suppression that emerges from vortex removal. These two functions model a screened and anti-screened potential, each with their own physical ramifications. Both are able to model the vortex-removed potential to a greater degree of accuracy than the Coulomb potential. We then use the results of these fits to model the untouched potential's short-range behaviour. In doing this, we find that we obtain excellent agreement between the untouched and vortex-only string tension. These results for the first time reconcile the differences between the vortex-only and untouched static quark potential, and strongly motivate a further exploration of the impact of dynamical fermions on centre vortices.

This investigation is continued in Chapter 6, where we consider the impact of dynamical fermions on the gluon propagator from a centre vortex perspective. We find that centre vortices capture the infrared behaviour of the propagator in both the pure-gauge and dynamical case. Vortex removal shows the biggest shift, with the dynamical vortex-removed propagator showing a complete lack of infrared strength, contrasting the substantial residual strength found in the pure gauge propagator. However, reconstruction of the original propagator from its vortex-modified components is less accurate on the dynamical ensembles, although this may be in part due to the renormalisation ambiguity in the vortex-only propagator.

Positivity violation is also explored by calculating the Euclidean correlator. We find that vortex-only ensembles exhibit positivity violation, which is a clear indicator of confinement. The vortex-removed correlator in the pure-gauge sector shows some violation of positivity at large Euclidean times, however this vanishes upon the introduction of dynamical fermions. This supports the notion that the vortex-removed fields describe free particles, and coincides with the suppression of infrared enhancement of the vortex-removed gluon propagator in full QCD.

Finally, in Chapter 7 we revisit our visualisations in the context of full QCD, with the intention of determining the shift in centre vortex geometry upon the introduction of dynamical fermions. We first examine the bulk structure of the gauge fields through a number of metrics, and determine that the dynamical ensembles retain a greater proportion of their off-diagonal strength after vortex-removal.

To examine the centre vortex structure, we develop new algorithms to identify independent vortex clusters. This is used to verify that the vacuum is indeed dominated by a single percolating cluster. We find that the number of secondary clusters is greatly enhanced upon the introduction of dynamical fermions, although these secondary clusters tend to be smaller than their pure-gauge counterparts. We also determine that both the vortex density and the branching point density increase substantially upon introduction of dynamical fermions, and continues to increase as the pion mass decreases.

We then explore a novel view of centre vortex clusters as a directed graph connecting touching and branching points. An algorithm is developed to facilitate the construction of these graphs, and the resulting structure is shown. We utilise this new perspective to examine the separation of branching points and explore the rate at which centre vortices branch. We find that whilst branching occurs at an approximately constant rate over medium to large separations, at short distances there is a tendency for branching points to cluster. This clustering is enhanced in the presence of dynamical fermions.

The significance of this work is twofold. Firstly, we have developed new analytical and visualisation techniques that allow for a detailed exploration of the geometry of $SU(3)$ centre vortices. Secondly, we have consistently shown that the presence of dynamical fermions radically alters the behaviour of vortex-modified ensembles. This is reflected in the significant improvement in the ability of centre vortices to capture the salient confinement properties of QCD, and the corresponding loss of these properties upon vortex removal. These results reinforce the fact that centre vortices underpin the complicated non-perturbative behaviour of QCD, and open exciting new avenues for research into the interplay between centre vortices and dynamical fermions.

References

[1] R. L. Workman et al. "Review of Particle Physics". In: *PTEP* 2022 (2022), p. 083C01. DOI: 10.1093/ptep/ptac097.

[2] Gerard 't Hooft. "On the Phase Transition Towards Permanent Quark Confinement". In: *Nucl. Phys. B* 138 (1978), pp. 1–25. DOI: 10.1016/0550-3213(78)90153-0.

[3] Gerard 't Hooft. "A Property of Electric and Magnetic Flux in Nonabelian Gauge Theories". In: *Nucl. Phys. B* 153 (1979), pp. 141–160. DOI: 10.1016/0550-3213(79)90595-9.

[4] Holger Bech Nielsen and P. Olesen. "A Quantum Liquid Model for the QCD Vacuum: Gauge and Rotational Invariance of Domained and Quantized Homogeneous Color Fields". In: *Nucl. Phys. B* 160 (1979), pp. 380–396. DOI: 10.1016/0550-3213(79)90065-8.

[5] L. Del Debbio et al. "Center dominance and Z(2) vortices in SU(2) lattice gauge theory". In: *Phys. Rev. D* 55 (1997), pp. 2298–2306. DOI: 10.1103/PhysRevD.55.2298. arXiv: hep-lat/9610005.

[6] Manfried Faber, J. Greensite, and Š. Olejnik. "Casimir scaling from center vortices: Towards an understanding of the adjoint string tension". In: *Phys. Rev. D* 57 (1998), pp. 2603–2609. DOI: 10.1103/PhysRevD.57.2603. arXiv: hep-lat/9710039.

[7] L. Del Debbio et al. "Detection of center vortices in the lattice Yang-Mills vacuum". In: *Phys. Rev. D* 58 (1998), p. 094501. DOI: 10.1103/PhysRevD.58.094501. arXiv: hep-lat/9801027.

[8] R. Bertle et al. "The Structure of projected center vortices in lattice gauge theory". In: *JHEP* 03 (1999), p. 019. DOI: 10.1088/1126-6708/1999/03/019. arXiv: hep-lat/9903023.

[9] Manfried Faber et al. "The Vortex finding property of maximal center (and other) gauges". In: *JHEP* 12 (1999), p. 012. DOI: 10.1088/1126-6708/1999/12/012. arXiv: hep-lat/9910033.

[10] M. Engelhardt and H. Reinhardt. "Center projection vortices in continuum Yang-Mills theory". In: *Nucl. Phys. B* 567 (2000), p. 249. DOI: 10.1016/S0550-3213(99)00727-0. arXiv: hep-th/9907139.

[11] Roman Bertle et al. "P vortices, gauge copies, and lattice size". In: *JHEP* 10 (2000), p. 007. DOI: 10.1088/1126-6708/2000/10/007. arXiv: hep-lat/0007043.

[12] M. Engelhardt, M. Quandt, and H. Reinhardt. "Center vortex model for the infrared sector of SU(3) Yang-Mills theory: Confinement and deconfinement". In: *Nucl. Phys. B* 685 (2004), pp. 227–248. DOI: 10.1016/j.nuclphysb.2004.02.036. arXiv: hep-lat/0311029.

[13] Kurt Langfeld. "Vortex structures in pure SU(3) lattice gauge theory". In: *Phys. Rev. D* 69 (2004), p. 014503. DOI: 10.1103/PhysRevD.69.014503. arXiv: hep-lat/0307030.

[14] Patrick O. Bowman et al. "Role of center vortices in chiral symmetry breaking in SU(3) gauge theory". In: *Phys. Rev. D* 84 (2011), p. 034501. DOI: 10.1103/PhysRevD.84.034501. arXiv: 1010.4624 [hep-lat].

[15] James C. Biddle, Waseem Kamleh, and Derek B. Leinweber. "Gluon propagator on a center-vortex background". In: *Phys. Rev. D* 98.9 (2018), p. 094504. DOI: 10.1103/PhysRevD.98.094504. arXiv: 1806.04305 [hep-lat].

[16] Alan O'Cais et al. "Preconditioning Maximal Center Gauge with Stout Link Smearing in SU(3)". In: *Phys. Rev. D* 82 (2010), p. 114512. DOI: 10.1103/PhysRevD.82.114512. arXiv: 0807.0264 [hep-lat].

[17] Amalie Trewartha, Waseem Kamleh, and Derek Leinweber. "Connection between center vortices and instantons through gauge-field smoothing". In: *Phys. Rev. D* 92.7 (2015), p. 074507. DOI: 10.1103/PhysRevD.92.074507. arXiv: 1509.05518 [hep-lat].

[18] Amalie Trewartha, Waseem Kamleh, and Derek Leinweber. "Evidence that centre vortices underpin dynamical chiral symmetry breaking in SU(3) gauge theory". In: *Phys. Lett. B* 747 (2015), pp. 373–377. DOI: 10.1016/j.physletb.2015.06.025. arXiv: 1502.06753 [hep-lat].

[19] Elyse-Ann O'Malley et al. "SU(3) centre vortices underpin confinement and dynamical chiral symmetry breaking". In: *Phys. Rev. D* 86 (2012), p. 054503. DOI: 10.1103/PhysRevD.86.054503. arXiv: 1112.2490 [hep-lat].

[20] Amalie Trewartha, Waseem Kamleh, and Derek B. Leinweber. "Centre vortex removal restores chiral symmetry". In: *J. Phys. G* 44.12 (2017), p. 125002. DOI: 10.1088/1361-6471/aa9443. arXiv: 1708.06789 [hep-lat].

[21] James C. Biddle, Waseem Kamleh, and Derek B. Leinweber. "Visualization of center vortex structure". In: *Phys. Rev. D* 102.3 (2020), p. 034504. DOI: 10.1103/PhysRevD.102.034504. arXiv: 1912.09531 [hep-lat].

[22] James C. Biddle, Waseem Kamleh, and Derek B. Leinweber. "Static quark potential from center vortices in the presence of dynamical fermions". In: *Phys. Rev. D* 106.5 (2022), p. 054505. DOI: 10.1103/PhysRevD.106.054505. arXiv: 2206.00844 [hep-lat].

[23] James C. Biddle, Waseem Kamleh, and Derek B. Leinweber. "Impact of dynamical fermions on the center vortex gluon propagator". In: *Phys. Rev. D* 106.1 (2022), p. 014506. DOI: 10.1103/PhysRevD.106.014506. arXiv: 2206.02320 [hep-lat].

[24] James C. Biddle, Waseem Kamleh, and Derek B. Leinweber. "Center vortex structure in the presence of dynamical fermions". In: *Phys. Rev. D* 107.9 (2023), p. 094507. DOI: 10.1103/PhysRevD.107.094507. arXiv: 2302.05897 [hep-lat].

[25] B. Sheikholeslami and R. Wohlert. "Improved Continuum Limit Lattice Action for QCD with Wilson Fermions". In: *Nucl. Phys. B* 259 (1985), p. 572. DOI: 10.1016/0550-3213(85)90002-1.

[26] John B. Kogut and Leonard Susskind. "Hamiltonian Formulation of Wilson's Lattice Gauge Theories". In: *Phys. Rev. D* 11 (1975), pp. 395–408. DOI: 10.1103/PhysRevD.11.395.

[27] Paul H. Ginsparg and Kenneth G. Wilson. "A Remnant of Chiral Symmetry on the Lattice". In: *Phys. Rev. D* 25 (1982), p. 2649. DOI: 10.1103/PhysRevD.25.2649.

[28] David B. Kaplan. "A Method for simulating chiral fermions on the lattice". In: *Phys. Lett. B* 288 (1992), pp. 342–347. DOI: 10.1016/0370-2693(92)91112-M. arXiv: hep-lat/9206013.

[29] K. Symanzik. "Continuum Limit and Improved Action in Lattice Theories. 1. Principles and phi**4 Theory". In: *Nucl. Phys. B* 226 (1983), pp. 187–204. DOI: 10.1016/0550-3213(83)90468-6.

[30] K. Symanzik. "Continuum Limit and Improved Action in Lattice Theories. 2. O(N) Nonlinear Sigma Model in Perturbation Theory". In: *Nucl. Phys. B* 226 (1983), pp. 205–227. DOI: 10.1016/0550-3213(83)90469-8.

[31] Mark G. Alford et al. "Lattice QCD on small computers". In: *Phys. Lett. B* 361 (1995), pp. 87–94. DOI: 10.1016/0370-2693(95)01131-9. arXiv: hep-lat/9507010.

[32] S. Aoki et al. “Nonperturbative O(a) improvement of the Wilson quark action with the RG-improved gauge action using the Schrödinger functional method”. In: *Phys. Rev. D* 73 (2006), p. 034501. DOI: 10.1103/PhysRevD.73.034501. arXiv: hep-lat/0508031.

[33] M. Lüscher and P. Weisz. “On-Shell Improved Lattice Gauge Theories”. In: *Commun. Math. Phys.* 97 (1985). [Erratum: Commun. Math. Phys.98,433(1985)], p. 59. DOI: 10.1007/BF01206178.

[34] G. Peter Lepage and Paul B. Mackenzie. “On the viability of lattice perturbation theory”. In: *Phys. Rev. D* 48 (1993), pp. 2250–2264. DOI: 10.1103/PhysRevD.48.2250. arXiv: hep-lat/9209022.

[35] Y. Iwasaki. “Renormalization Group Analysis of Lattice Theories and Improved Lattice Action: Two-Dimensional Nonlinear O(N) Sigma Model”. In: *Nucl. Phys. B* 258 (1985), pp. 141–156. DOI: 10.1016/0550-3213(85)90606-6.

[36] N. Cabibbo and E. Marinari. “A New Method for Updating SU(N) Matrices in Computer Simulations of Gauge Theories”. In: *Phys. Lett. B* 119 (1982), pp. 387–390. DOI: 10.1016/0370-2693(82)90696-7.

[37] Christof Gattringer and Christian B Lang. *Quantum Chromodynamics on the Lattice: An Introductory Presentation*. Vol. 788. Lecture Notes in Physics. Berlin, Heidelberg: Springer Berlin Heidelberg, 2010. ISBN: 3642018491.

[38] S. Aoki et al. “2+1 Flavor Lattice QCD toward the Physical Point”. In: *Phys. Rev. D* 79 (2009), p. 034503. DOI: 10.1103/PhysRevD.79.034503. arXiv: 0807.1661 [hep-lat].

[39] Martin Lüscher. “Solution of the Dirac equation in lattice QCD using a domain decomposition method”. In: *Comput. Phys. Commun.* 156 (2004), pp. 209–220. DOI: 10.1016/S0010-4655(03)00486-7. arXiv: hep-lat/0310048.

[40] Gerard ’t Hooft. “Topology of the Gauge Condition and New Confinement Phases in Nonabelian Gauge Theories”. In: *Nucl. Phys. B* 190 (1981), pp. 455–478. DOI: 10.1016/0550-3213(81)90442-9.

[41] Jan Smit and Arjan van der Sijs. “Monopoles and Confinement”. In: *Nucl. Phys. B* 355 (1991), pp. 603–648. DOI: 10.1016/0550-3213(91)90489-K.

[42] Yoshimi Matsubara, Shinji Ejiri, and Tsuneoo Suzuki. “The (dual) Meissner effect in SU(2) and SU(3) QCD”. In: *Nucl. Phys. Proc. Suppl.* 34 (1994), pp. 176–178. DOI: 10.1016/0920-5632(94)90337-9. arXiv: hep-lat/9311061.

[43] Tsuneo Suzuki and Ichiro Yotsuyanagi. “A possible evidence for Abelian dominance in quark confinement”. In: *Phys. Rev. D* 42 (1990), pp. 4257–4260. DOI: 10.1103/PhysRevD.42.4257.

[44] S. Mandelstam. "Vortices and Quark Confinement in Nonabelian Gauge Theories". In: *Phys. Rept.* 23 (1976), pp. 245–249. DOI: 10.1016/0370-1573(76)90043-0.

[45] Andreas S. Kronfeld et al. "Monopole Condensation and Color Confinement". In: *Phys. Lett.B* 198 (1987), pp. 516–520. DOI: 10.1016/0370-2693(87)90910-5.

[46] T. L. Ivanenko, A. V. Pochinsky, and M. I. Polikarpov. "Extended Abelian monopoles and confinement in the SU(2) lattice gauge theory". In: *Phys. Lett. B* 252 (1990), pp. 631–635. DOI: 10.1016/0370-2693(90)90497-T.

[47] M. N. Chernodub and F. V. Gubarev. "Instantons and monopoles in maximal Abelian projection of SU(2) gluodynamics". In: *JETP Lett.* 62 (1995), pp. 100–104. arXiv: hep-th/9506026.

[48] Adriano Di Giacomo, Michele Maggiore, and Štefan Olejnik. "Confinement and Chromoelectric Flux Tubes in Lattice QCD". In: *Nucl. Phys. B* 347 (1990), pp. 441–460. DOI: 10.1016/0550-3213(90)90567-W.

[49] A. A. Belavin et al. "Pseudoparticle Solutions of the Yang-Mills Equations". In: *Phys. Lett. B* 59 (1975), pp. 85–87. DOI: 10.1016/0370-2693(75)90163-X.

[50] Edward Witten. "Instantons, the Quark Model, and the 1/n Expansion". In: *Nucl. Phys. B* 149 (1979), pp. 285–320. DOI: 10.1016/0550-3213(79)90243-8.

[51] Curtis G. Callan Jr., Roger F. Dashen, and David J. Gross. "Toward a Theory of the Strong Interactions". In: *Phys. Rev. D* 17 (1978), p. 2717. DOI: 10.1103/PhysRevD.17.2717.

[52] Thomas Schäfer and Edward V. Shuryak. "Instantons in QCD". In: *Rev. Mod. Phys.* 70 (1998), pp. 323–426. DOI: 10.1103/RevModPhys.70.323. arXiv: hep-ph/9610451.

[53] Amalie Trewartha et al. "Quark Propagation in the Instantons of Lattice QCD". In: *Phys. Rev. D* 88 (2013), p. 034501. DOI: 10.1103/PhysRevD.88.034501. arXiv: 1306.3283 [hep-lat].

[54] Y. Aharonov, A. Casher, and S. Yankielowicz. "Instantons and Confinement". In: *Nucl. Phys. B* 146 (1978), pp. 256–272. DOI: 10.1016/0550-3213(78)90442-X.

[55] V. P. Nair and Robert D. Pisarski. "Fractional topological charge in $SU(N)$ gauge theories without dynamical quarks". In: (June 2022). arXiv: 2206.11284 [hep-th].

[56] Robert D. Pisarski and Fabian Rennecke. "Multi-instanton contributions to anomalous quark interactions". In: *Phys. Rev. D* 101.11 (2020), p. 114019. DOI: 10.1103/PhysRevD.101.114019. arXiv: 1910.14052 [hep-ph].

[57] Yizhuang Liu, Edward Shuryak, and Ismail Zahed. "Confining dyon-antidyon Coulomb liquid model. I." In: *Phys. Rev. D* 92.8 (2015), p. 085006. DOI: 10.1103/PhysRevD.92.085006. arXiv: 1503.03058 [hep-ph].

[58] Rasmus Larsen and Edward Shuryak. "Instanton-dyon Ensemble with two Dynamical Quarks: the Chiral Symmetry Breaking". In: *Phys. Rev. D* 93.5 (2016), p. 054029. DOI: 10.1103/PhysRevD.93.054029. arXiv: 1511.02237 [hep-ph].

[59] Dallas DeMartini and Edward Shuryak. "Deconfinement phase transition in the SU(3) instanton-dyon ensemble". In: *Phys. Rev. D* 104.5 (2021), p. 054010. DOI: 10.1103/PhysRevD.104.054010. arXiv: 2102.11321 [hep-ph].

[60] Dallas DeMartini and Edward Shuryak. "Chiral symmetry breaking and confinement from an interacting ensemble of instanton dyons in two-flavor massless QCD". In: *Phys. Rev. D* 104.9 (2021), p. 094031. DOI: 10.1103/PhysRevD.104.094031. arXiv: 2108.06353 [hep-ph].

[61] Jeff Greensite. "Confinement from Center Vortices: A review of old and new results". In: *EPJ Web Conf.* 137 (2017), p. 01009. DOI: 10.1051/epjconf/201713701009. arXiv: 1610.06221 [hep-lat].

[62] Falk Bruckmann and Michael Engelhardt. "Writhe of center vortices and topological charge: An Explicit example". In: *Phys. Rev. D* 68 (2003), p. 105011. DOI: 10.1103/PhysRevD.68.105011. arXiv: hep-th/0307219.

[63] M. Engelhardt et al. "Deconfinement in SU(2) Yang-Mills theory as a center vortex percolation transition". In: *Phys. Rev. D* 61 (2000), p. 054504. DOI: 10.1103/PhysRevD.61.054504. arXiv: hep-lat/9904004.

[64] Ernst-Michael Ilgenfritz et al. "Localization of overlap modes and topological charge, vortices and monopoles in SU(3) LGT". In: *PoS* LATTICE2007 (2007). Ed. by Gunnar Bali et al., p. 311. DOI: 10.22323/1.042.0311. arXiv: 0710.2607 [hep-lat].

[65] J. Greensite. "The Confinement problem in lattice gauge theory". In: *Prog. Part. Nucl. Phys.* 51 (2003), p. 1. DOI: 10.1016/S0146-6410(03)90012-3. arXiv: hep-lat/0301023.

[66] Michael Engelhardt. "Center vortex model for the infrared sector of Yang-Mills theory: Topological susceptibility". In: *Nucl. Phys. B* 585 (2000), p. 614. DOI: 10.1016/S0550-3213(00)00350-3. arXiv: hep-lat/0004013.

[67] Felix Spengler, Markus Quandt, and Hugo Reinhardt. "Branching of Center Vortices in SU(3) Lattice Gauge Theory". In: *Phys. Rev. D* 98.9 (2018), p. 094508. DOI: 10.1103/PhysRevD.98.094508. arXiv: 1810.04072 [hep-th].

[68] K. Langfeld, H. Reinhardt, and J. Gattnar. "Gluon propagators and quark confinement". In: *Nucl. Phys. B* 621 (2002), pp. 131–156. DOI: 10.1016/S0550-3213(01)00574-0. arXiv: hep-ph/0107141.

[69] Michael Engelhardt. "Center vortex model for the infrared sector of SU(3) Yang-Mills theory: Topological susceptibility". In: *Phys. Rev. D* 83 (2011), p. 025015. DOI: 10.1103/PhysRevD.83.025015. arXiv: 1008.4953 [hep-lat].

[70] Richard P. Feynman. "The Qualitative Behavior of Yang-Mills Theory in (2+1)-Dimensions". In: *Nucl. Phys. B* 188 (1981), pp. 479–512. DOI: 10.1016/0550-3213(81)90005-5.

[71] John M. Cornwall. "Quark Confinement and Vortices in Massive Gauge Invariant QCD". In: *Nucl. Phys.* 157 (1979), pp. 392–412. DOI: 10.1016/0550-3213(79)90111-1.

[72] P. Yu. Boyko et al. "Once more on the interrelation between Abelian monopoles and P-vortices in SU(2) LGT". In: *Nucl. Phys. B* 756 (2006), pp. 71–85. DOI: 10.1016/j.nuclphysb.2006.08.025. arXiv: hep-lat/0607003.

[73] G. Mack and V. B. Petkova. "Comparison of Lattice Gauge Theories with Gauge Groups Z(2) and SU(2)". In: *Annals Phys.* 123 (1979), p. 442. DOI: 10.1016/0003-4916(79)90346-4.

[74] V. G. Bornyakov et al. "Interrelation between monopoles, vortices, topological charge and chiral symmetry breaking: Analysis using overlap fermions for SU(2)". In: *Phys. Rev. D* 77 (2008), p. 074507. DOI: 10.1103/PhysRevD.77.074507. arXiv: 0708.3335 [hep-lat].

[75] Michael R. Douglas and Stephen H. Shenker. "Dynamics of SU(N) supersymmetric gauge theory". In: *Nucl. Phys. B* 447 (1995), pp. 271–296. DOI: 10.1016/0550-3213(95)00258-T. arXiv: hep-th/9503163.

[76] Jan Ambjørn, J. Giedt, and J. Greensite. "Vortex structure versus monopole dominance in Abelian projected gauge theory". In: *JHEP* 02 (2000), p. 033. DOI: 10.1088/1126-6708/2000/02/033. arXiv: hep-lat/9907021.

[77] Tom Banks and A. Casher. "Chiral Symmetry Breaking in Confining Theories". In: *Nucl. Phys. B* 169 (1980), pp. 103–125. DOI: 10.1016/0550-3213(80)90255-2.

[78] Jan Ambjørn and P. Olesen. "A Color Magnetic Vortex Condensate in QCD". In: *Nucl. Phys. B* 170 (1980), pp. 265–282. DOI: 10.1016/0550-3213(80)90150-9.

[79] Jan Ambjørn and P. Olesen. "On the Formation of a Random Color Magnetic Quantum Liquid in QCD". In: *Nucl. Phys. B* 170 (1980), pp. 60–78. DOI: 10.1016/0550-3213(80)90476-9.

[80] Roman Bertle et al. “Center vortices and color confinement in lattice QCD”. In: *4th International Conference on Quark Confinement and the Hadron Spectrum*. July 2000, pp. 138–149. arXiv: hep-lat/0009017.

[81] Hans Gunter Dosch and Yu. A. Simonov. “The Area Law of the Wilson Loop and Vacuum Field Correlators”. In: *Phys. Lett. B* 205 (1988), pp. 339–344. DOI: 10.1016/0370-2693(88)91675-9.

[82] Alvaro Montero. “Study of SU(3) vortex - like configurations with a new maximal center gauge fixing method”. In: *Phys. Lett. B* 467 (1999), pp. 106–111. DOI: 10.1016/S0370-2693(99)01113-2. arXiv: hep-lat/9906010.

[83] Alan O’Cais et al. “Preconditioning Maximal Center Gauge with Stout Link Smearing in SU(3)”. In: *Phys. Rev. D* 82 (2010), p. 114512. DOI: 10.1103/PhysRevD.82.114512. arXiv: 0807.0264 [hep-lat].

[84] Philippe de Forcrand and Massimo D’Elia. “On the relevance of center vortices to QCD”. In: *Phys. Rev. Lett.* 82 (1999), pp. 4582–4585. DOI: 10.1103/PhysRevLett.82.4582. arXiv: hep-lat/9901020.

[85] Kurt Langfeld, Hugo Reinhardt, and Oliver Tennert. “Confinement and scaling of the vortex vacuum of SU(2) lattice gauge theory”. In: *Phys. Lett. B* 419 (1998), pp. 317–321. DOI: 10.1016/S0370-2693(97)01435-4. arXiv: hep-lat/9710068.

[86] M. Engelhardt et al. “Interaction of confining vortices in SU(2) lattice gauge theory”. In: *Phys. Lett. B* 431 (1998), pp. 141–146. DOI: 10.1016/S0370-2693(98)00583-8. arXiv: hep-lat/9801030.

[87] Patrick O. Bowman et al. “Center vortices and the quark propagator in SU(2) gauge theory”. In: *Phys. Rev. D* 78 (2008), p. 054509. DOI: 10.1103/PhysRevD.78.054509. arXiv: 0806.4219 [hep-lat].

[88] Frederic D. R. Bonnet et al. “Calibration of smearing and cooling algorithms in SU(3): Color gauge theory”. In: *Phys. Rev. D* 62 (2000), p. 094509. DOI: 10.1103/PhysRevD.62.094509. arXiv: hep-lat/0001018.

[89] Adam Virgili, Waseem Kamleh, and Derek Leinweber. “Smoothing algorithms for projected center-vortex gauge fields”. In: *Phys. Rev. D* 106.1 (2022), p. 014505. DOI: 10.1103/PhysRevD.106.014505. arXiv: 2203.09764 [hep-lat].

[90] Sundance O. Bilson-Thompson, Derek B. Leinweber, and Anthony G. Williams. “Highly improved lattice field strength tensor”. In: *Annals Phys.* 304 (2003), pp. 1–21. DOI: 10.1016/S0003-4916(03)00009-5. arXiv: hep-lat/0203008.

[91] M. Albanese et al. “Glueball Masses and String Tension in Lattice QCD”. In: *Phys. Lett. B* 192 (1987), pp. 163–169. DOI: 10.1016/0370-2693(87)91160-9.

[92] M. Falcioni et al. “Again on SU(3) Glueball Mass”. In: *Nucl. Phys. B* 251 (1985), pp. 624–632. DOI: 10.1016/0550-3213(85)90280-9.

[93] Waseem Kamleh, Derek B. Leinweber, and Anthony G. Williams. “Hybrid Monte Carlo with fat link fermion actions”. In: *Phys. Rev. D* 70 (2004), p. 014502. DOI: 10.1103/PhysRevD.70.014502. arXiv: hep-lat/0403019.

[94] Colin Morningstar and Mike J. Peardon. “Analytic smearing of SU(3) link variables in lattice QCD”. In: *Phys. Rev. D* 69 (2004), p. 054501. DOI: 10.1103/PhysRevD.69.054501. arXiv: hep-lat/0311018.

[95] Peter J. Moran and Derek B. Leinweber. “Over-improved stout-link smearing”. In: *Phys. Rev. D* 77 (2008), p. 094501. DOI: 10.1103/PhysRevD.77.094501. arXiv: 0801.1165 [hep-lat].

[96] James C. Biddle, Waseem Kamleh, and Derek B. Leinweber. “Visualizations of Centre Vortex Structure in Lattice Simulations”. In: *PoS* LATTICE2018 (2018), p. 256. DOI: 10.22323/1.334.0256. arXiv: 1903.07767 [hep-lat].

[97] James Biddle et al. “Publicizing Lattice Field Theory through Visualization”. In: *PoS* LATTICE2018 (2019), p. 325. DOI: 10.22323/1.334.0325. arXiv: 1903.08308 [hep-lat].

[98] Constantia Alexandrou et al. “Comparison of topological charge definitions in Lattice QCD”. In: *Eur. Phys. J. C* 80.5 (2020), p. 424. DOI: 10.1140/epjc/s10052-020-7984-9. arXiv: 1708.00696 [hep-lat].

[99] Sundance O. Bilson-Thompson et al. “Cooling for instantons and the wrath of Nahm”. In: *Nucl. Phys. B Proc. Suppl.* 109 (2002). Ed. by A. C. Kalloniatis et al., pp. 116–120. DOI: 10.1016/S0920-5632(02)01399-3. arXiv: hep-lat/0112034.

[100] Sundance O. Bilson-Thompson et al. “Comparison of $|Q| = 1$ and $|Q| = 2$ gauge-field configurations on the lattice four-torus”. In: *Annals Phys.* 311 (2004), pp. 267–287. DOI: 10.1016/j.aop.2003.12.011. arXiv: hep-lat/0306010.

[101] M. Lüscher and P. Weisz. “Definition and General Properties of the Transfer Matrix in Continuum Limit Improved Lattice Gauge Theories”. In: *Nucl. Phys. B* 240 (1984), pp. 349–361. DOI: 10.1016/0550-3213(84)90270-0.

[102] Derek B. Leinweber, R. M. Woloshyn, and Terrence Draper. “Electromagnetic structure of octet baryons”. In: *Phys. Rev. D* 43 (1991), pp. 1659–1678. DOI: 10.1103/PhysRevD.43.1659.

[103] M. S. Mahbub et al. “Isolating Excited States of the Nucleon in Lattice QCD”. In: *Phys. Rev. D* 80 (2009), p. 054507. DOI: 10.1103/PhysRevD.80.054507. arXiv: 0905.3616 [hep-lat].

[104] Gunnar S. Bali et al. "Observation of string breaking in QCD". In: *Phys. Rev. D* 71 (2005), p. 114513. DOI: 10.1103/PhysRevD.71.114513. arXiv: hep-lat/0505012.

[105] John Bulava et al. "String breaking by light and strange quarks in QCD". In: *Phys. Lett. B* 793 (2019), pp. 493–498. DOI: 10.1016/j.physletb.2019.05.018. arXiv: 1902.04006 [hep-lat].

[106] S. Aoki et al. "Comparative study of full QCD hadron spectrum and static quark potential with improved actions". In: *Phys. Rev. D* 60 (1999), p. 114508. DOI: 10.1103/PhysRevD.60.114508. arXiv: hep-lat/9902018.

[107] Christopher Michael. "The Running coupling from lattice gauge theory". In: *Phys. Lett. B* 283 (1992), pp. 103–106. DOI: 10.1016/0370-2693(92)91435-C. arXiv: hep-lat/9205010.

[108] R. G. Edwards, Urs M. Heller, and T. R. Klassen. "Accurate scale determinations for the Wilson gauge action". In: *Nucl. Phys. B* 517 (1998), pp. 377–392. DOI: 10.1016/S0550-3213(98)80003-5. arXiv: hep-lat/9711003.

[109] R. Sommer. "A New way to set the energy scale in lattice gauge theories and its applications to the static force and alpha-s in SU(2) Yang-Mills theory". In: *Nucl. Phys. B* 411 (1994), pp. 839–854. DOI: 10.1016/0550-3213(94)90473-1. arXiv: hep-lat/9310022.

[110] Timothy R. Klassen. "The (Lattice) QCD potential and coupling: How to accurately interpolate between multiloop QCD and the string picture". In: *Phys. Rev. D* 51 (1995), pp. 5130–5152. DOI: 10.1103/PhysRevD.51.5130. arXiv: hep-lat/9408016.

[111] Alexandre Deur, Stanley J. Brodsky, and Guy F. de Teramond. "The QCD Running Coupling". In: *Nucl. Phys.* 90 (2016), p. 1. DOI: 10.1016/j.ppnp.2016.04.003. arXiv: 1604.08082 [hep-ph].

[112] S. P. Booth et al. "The Running coupling from SU(3) lattice gauge theory". In: *Phys. Lett. B* 294 (1992), pp. 385–390. DOI: 10.1016/0370-2693(92)91538-K. arXiv: hep-lat/9209008.

[113] Gunnar S. Bali and Klaus Schilling. "Running coupling and the Lambda parameter from SU(3) lattice simulations". In: *Phys. Rev. D* 47 (1993), pp. 661–672. DOI: 10.1103/PhysRevD.47.661. arXiv: hep-lat/9208028.

[114] Martin Lüscher et al. "A Precise determination of the running coupling in the SU(3) Yang-Mills theory". In: *Nucl. Phys. B* 413 (1994), pp. 481–502. DOI: 10.1016/0550-3213(94)90629-7. arXiv: hep-lat/9309005.

[115] T. Blum et al. "The beta function and equation of state for QCD with two flavors of quarks". In: *Phys. Rev. D* 51 (1995), pp. 5153–5164. DOI: 10.1103/PhysRevD.51.5153. arXiv: hep-lat/9410014.

[116] K. Hornbostel, G. P. Lepage, and C. Morningstar. "Scale setting for alpha(s) beyond leading order". In: *Phys. Rev. D* 67 (2003), p. 034023. DOI: 10.1103/PhysRevD.67.034023. arXiv: hep-ph/0208224.

[117] Alexei Bazavov et al. "Determination of α_s from the QCD static energy: An update". In: *Phys. Rev. D* 90.7 (2014). [Erratum: Phys.Rev.D 101, 119902 (2020)], p. 074038. DOI: 10.1103/PhysRevD.90.074038. arXiv: 1407.8437 [hep-ph].

[118] J. E. Mandula and M. Ogilvie. "The Gluon Is Massive: A Lattice Calculation of the Gluon Propagator in the Landau Gauge". In: *Phys. Lett. B* 185 (1987), pp. 127–132. DOI: 10.1016/0370-2693(87)91541-3.

[119] I. L. Bogolubsky et al. "The Landau gauge gluon and ghost propagators in 4D SU(3) gluodynamics in large lattice volumes". In: *PoS* LATTICE2007 (2007). Ed. by Gunnar Bali et al., p. 290. DOI: 10.22323/1.042.0290. arXiv: 0710.1968 [hep-lat].

[120] I. L. Bogolubsky et al. "Lattice gluodynamics computation of Landau gauge Green's functions in the deep infrared". In: *Phys. Lett. B* 676 (2009), pp. 69–73. DOI: 10.1016/j.physletb.2009.04.076. arXiv: 0901.0736 [hep-lat].

[121] Shirley Weishi Li et al. "The generalised infrared structure of the gluon propagator". In: *Phys. Lett. B* 803 (2020), p. 135329. DOI: 10.1016/j.physletb.2020.135329. arXiv: 1907.10073 [hep-th].

[122] Jan Horak et al. "Gluon condensates and effective gluon mass". In: *SciPost Phys.* 13.2 (2022), p. 042. DOI: 10.21468/SciPostPhys.13.2.042. arXiv: 2201.09747 [hep-ph].

[123] John M. Cornwall and George Tiktopoulos. "Infrared Behavior of Nonabelian Gauge Theories". In: *Phys. Rev. D* 13 (1976), p. 3370. DOI: 10.1103/PhysRevD.13.3370.

[124] M. Lüscher. "Symmetry Breaking Aspects of the Roughening Transition in Gauge Theories". In: *Nucl. Phys. B* 180 (1981), pp. 317–329. DOI: 10.1016/0550-3213(81)90423-5.

[125] Gunnar S. Bali et al. "Static potentials and glueball masses from QCD simulations with Wilson sea quarks". In: *Phys. Rev. D* 62 (2000), p. 054503. DOI: 10.1103/PhysRevD.62.054503. arXiv: hep-lat/0003012.

[126] Tamas G. Kovacs and E. T. Tomboulis. "On P vortices and the Gribov problem". In: *Phys. Lett. B* 463 (1999), pp. 104–108. DOI: 10.1016/S0370-2693(99)00944-2. arXiv: hep-lat/9905029.

[127] Manfried Faber, Jeff Greensite, and Štefan Olejnik. "Remarks on the Gribov problem in direct maximal center gauge". In: *Phys. Rev. D* 64 (2001), p. 034511. DOI: 10.1103/PhysRevD.64.034511. arXiv: hep-lat/0103030.

[128] Jeroen C. Vink and Uwe-Jens Wiese. "Gauge fixing on the lattice without ambiguity". In: *Phys. Lett. B* 289 (1992), pp. 122–126. DOI: 10.1016/0370-2693(92)91372-G. arXiv: hep-lat/9206006.

[129] C. Alexandrou, Massimo D'Elia, and P. de Forcrand. "The Relevance of center vortices". In: *Nucl. Phys. B Proc. Suppl.* 83 (2000). Ed. by M. Campostrini et al., pp. 437–439. DOI: 10.1016/S0920-5632(00)91698-0. arXiv: hep-lat/9907028.

[130] P. de Forcrand and M. Pepe. "Center vortices and monopoles without lattice Gribov copies". In: *Nucl. Phys. B* 598 (2001), pp. 557–577. DOI: 10.1016/S0550-3213(01)00009-8. arXiv: hep-lat/0008016.

[131] Manfried Faber, Jeff Greensite, and Štefan Olejnik. "Center dominance recovered: Direct Laplacian center gauge". In: *Nucl. Phys. B Proc. Suppl.* 106 (2002). Ed. by M. Müller-Preussker et al., pp. 652–654. DOI: 10.1016/S0920-5632(01)01805-9. arXiv: hep-lat/0109032.

[132] Manfried Faber, Jeff Greensite, and Štefan Olejnik. "Direct Laplacian center gauge". In: *JHEP* 11 (2001), p. 053. DOI: 10.1088/1126-6708/2001/11/053. arXiv: hep-lat/0106017.

[133] K. Langfeld, H. Reinhardt, and A. Schafke. "Center vortex properties in the Laplace center gauge of SU(2) Yang-Mills theory". In: *Phys. Lett. B* 504 (2001), pp. 338–344. DOI: 10.1016/S0370-2693(01)00318-5. arXiv: hep-lat/0101010.

[134] Jeff Greensite and Kazue Matsuyama. "Confinement criterion for gauge theories with matter fields". In: *Phys. Rev. D* 96.9 (2017), p. 094510. DOI: 10.1103/PhysRevD.96.094510. arXiv: 1708.08979 [hep-lat].

[135] Jeff Greensite and Kazue Matsuyama. "What symmetry is actually broken in the Higgs phase of a gauge-Higgs theory?" In: *Phys. Rev. D* 98.7 (2018), p. 074504. DOI: 10.1103/PhysRevD.98.074504. arXiv: 1805.00985 [hep-th].

[136] Jeff Greensite and Kazue Matsuyama. "Higgs phase as a spin glass and the transition between varieties of confinement". In: *Phys. Rev. D* 101.5 (2020), p. 054508. DOI: 10.1103/PhysRevD.101.054508. arXiv: 2001.03068 [hep-th].

[137] Jeff Greensite and Kazue Matsuyama. "Symmetry, Confinement, and the Higgs Phase". In: *Symmetry* 14.1 (2022), p. 177. DOI: 10.3390/sym14010177. arXiv: 2112.06421 [hep-lat].

[138] Patrick O. Bowman et al. "Scaling behavior and positivity violation of the gluon propagator in full QCD". In: *Phys. Rev. D* 76 (2007), p. 094505. DOI: 10.1103/PhysRevD.76.094505. arXiv: hep-lat/0703022.

[139] C. D. Roberts et al. "Aspects of hadron physics". In: *Eur. Phys. J. ST* 140 (2007). Ed. by R. Alkofer, A. Krassnigg, and W. Schweiger, pp. 53–116. DOI: 10.1140/epjst/e2007-00003-5. arXiv: 0802.0217 [nucl-th].

[140] B. Alles et al. "α_s from the nonperturbatively renormalised lattice three gluon vertex". In: *Nucl. Phys. B* 502 (1997), pp. 325–342. DOI: 10.1016/S0550-3213(97)00483-5. arXiv: hep-lat/9605033.

[141] Y. Iwasaki. "Renormalization Group Analysis of Lattice Theories and Improved Lattice Action. II. Four-dimensional non-Abelian SU(N) gauge model". In: (Dec. 1983). arXiv: 1111.7054 [hep-lat].

[142] P. Weisz and R. Wohlert. "Continuum Limit Improved Lattice Action for Pure Yang-Mills Theory. 2." In: *Nucl. Phys. B* 236 (1984). [Erratum: Nucl.Phys.B 247, 544 (1984)], p. 397. DOI: 10.1016/0550-3213(84)90563-7.

[143] P. Weisz. "Continuum Limit Improved Lattice Action for Pure Yang-Mills Theory. 1." In: *Nucl. Phys. B* 212 (1983), pp. 1–17. DOI: 10.1016/0550-3213(83)90595-3.

[144] Frederic D. R. Bonnet et al. "Infinite volume and continuum limits of the Landau gauge gluon propagator". In: *Phys. Rev. D* 64 (2001), p. 034501. DOI: 10.1103/PhysRevD.64.034501. arXiv: hep-lat/0101013.

[145] Derek B. Leinweber et al. "Asymptotic scaling and infrared behavior of the gluon propagator". In: *Phys. Rev. D* 60 (1999). [Erratum: Phys.Rev.D 61, 079901 (2000)], p. 094507. DOI: 10.1103/PhysRevD.60.094507. arXiv: hep-lat/9811027.

[146] Patrick O. Bowman et al. "Unquenched gluon propagator in Landau gauge". In: *Phys. Rev. D* 70 (2004), p. 034509. DOI: 10.1103/PhysRevD.70.034509. arXiv: hep-lat/0402032.

[147] Derek B. Leinweber et al. "Gluon propagator in the infrared region". In: *Phys. Rev. D* 58 (1998), p. 031501. DOI: 10.1103/PhysRevD.58.031501. arXiv: hep-lat/9803015.

[148] Patrick O. Bowman et al. "Gluon propagator on coarse lattices in Laplacian gauges". In: *Phys. Rev. D* 66 (2002), p. 074505. DOI: 10.1103/PhysRevD.66.074505. arXiv: hep-lat/0206010.

[149] A. S. Wightman. "Quantum Field Theory in Terms of Vacuum Expectation Values". In: *Phys. Rev.* 101 (1956), pp. 860–866. DOI: 10.1103/PhysRev.101.860.

[150] Konrad Osterwalder and Robert Schrader. "Axioms for Euclidean Green's Functions". In: *Commun. Math. Phys.* 31 (1973), pp. 83–112. DOI: 10.1007/BF01645738.

[151] V. G. Bornyakov, D. A. Komarov, and M. I. Polikarpov. "P vortices and drama of Gribov copies". In: *Phys. Lett. B* 497 (2001), pp. 151–158. DOI: 10.1016/S0370-2693(00)01309-5. arXiv: hep-lat/0009035.

[152] Advanced Visual Systems, Inc. *AVS Express*. https://www.avs.com/avs-express/. 2020.

[153] West Health Institute. *Pyvis*. https://github.com/WestHealth/pyvis. 2018.

[154] John L Hodges. "The significance probability of the Smirnov two-sample test". In: *Arkiv för Matematik* 3.5 (1958), pp. 469–486.

[155] Michael E Peskin. *An introduction to quantum field theory*. CRC Press, 2018.

Appendix A

Supplementary Material

A.1 Matrix Definitions

The standard form of the 2×2 Pauli matrices is

$$\sigma_1 = \begin{pmatrix} 0 & 1 \\ 1 & 0 \end{pmatrix}, \quad \sigma_2 = \begin{pmatrix} 0 & -i \\ i & 0 \end{pmatrix}, \quad \sigma_3 = \begin{pmatrix} 1 & 0 \\ 0 & -1 \end{pmatrix}. \tag{A.1}$$

The 4×4 gamma matrices in the Dirac representation in Minkowski space are given by

$$\gamma_0^M = \begin{pmatrix} I & 0 \\ 0 & -I \end{pmatrix}, \quad \gamma_i^M = \begin{pmatrix} 0 & \sigma_i \\ -\sigma_i & 0 \end{pmatrix}. \tag{A.2}$$

In Euclidean space, the gamma matrices are defined in terms of their Minkowski counterparts as

$$\gamma_i = -i\gamma_i^M, \quad \gamma_4 = \gamma_0^M. \tag{A.3}$$

The Euclidean gamma matrices satisfy the anti-commutation relationship

$$\{\gamma_\mu\,,\,\gamma_\mu\} = 2\,\delta_{\mu\nu}\,. \tag{A.4}$$

We also define the commutator of the gamma matrices to be

$$\sigma_{\mu\nu} = \frac{1}{2}[\gamma_\mu,\,\gamma_\nu]\,. \tag{A.5}$$

The Gell-Mann matrices λ_a are related to the generators of $SU(3)$, t_a, by [155]

$$t_a = \frac{\lambda_a}{2}\,. \tag{A.6}$$

The matrices are given by

$$\lambda_1 = \begin{pmatrix} 0 & 1 & 0 \\ 1 & 0 & 0 \\ 0 & 0 & 0 \end{pmatrix} \quad \lambda_2 = \begin{pmatrix} 0 & -i & 0 \\ i & 0 & 0 \\ 0 & 0 & 0 \end{pmatrix} \quad \lambda_3 = \begin{pmatrix} 1 & 0 & 0 \\ 0 & -1 & 0 \\ 0 & 0 & 0 \end{pmatrix}$$
$$\lambda_4 = \begin{pmatrix} 0 & 0 & 1 \\ 0 & 0 & 0 \\ 1 & 0 & 0 \end{pmatrix} \quad \lambda_5 = \begin{pmatrix} 0 & 0 & -i \\ 0 & 0 & 0 \\ i & 0 & 0 \end{pmatrix}$$
$$\lambda_6 = \begin{pmatrix} 0 & 0 & 0 \\ 0 & 0 & 1 \\ 0 & 1 & 0 \end{pmatrix} \quad \lambda_7 = \begin{pmatrix} 0 & 0 & 0 \\ 0 & 0 & -i \\ 0 & i & 0 \end{pmatrix} \quad \lambda_8 = \frac{1}{\sqrt{3}} \begin{pmatrix} 1 & 0 & 0 \\ 0 & 1 & 0 \\ 0 & 0 & -2 \end{pmatrix}. \tag{A.7}$$

Linear combinations of the Gell-Mann matrices form the Lie algebra of $SU(3)$, denoted $\mathfrak{su}(3)$.

A.2 Appearance of the Fermion Determinant

We wish to derive how the fermion determinant appears in integrals over Grassmann numbers. To do this, we consider how the Grassmann measure changes under a linear change of variables, defined by

$$\eta_i' = M_{ij}\eta_j\,. \tag{A.8}$$

For any integral the choice of variables clearly must not change the solution, so we have

$$\int d^N\eta\, f(\eta_1, \ldots, \eta_N) = \int d^N\eta'\, f(\eta_1', \ldots, \eta_N') \tag{A.9}$$

Recall that Grassmann integrals must also satisfy the normalisation equation,

$$\int d^N\eta\, \eta_1\, \eta_2\, \ldots\, \eta_N = 1 \tag{A.10}$$

To satisfy both Eq. (A.9) and Eq. (A.10), consider applying the change of variables specified in Eq. (A.8) to Eq. (A.10),

$$\int d^N\eta'\,\eta'_1\,\eta'_2\,\ldots\,\eta'_N = \int d^N\eta' \sum_{i_1,\ldots,i_N} M_{1i_1}\ldots M_{Ni_N}\,\eta_{i_1}\ldots\eta_{i_N} \tag{A.11}$$

$$= \int d^N\eta' \sum_{i_1,\ldots,i_N} M_{1i_1}\ldots M_{Ni_N}\,\epsilon_{i_1 i_2\ldots i_N}\,\eta_1\ldots\eta_N \tag{A.12}$$

The introduction of the antisymmetric epsilon tensor arises from the reordering of the Grassmann numbers. The term $\sum_{i_1,\ldots,i_N} M_{1i_1}\ldots M_{Ni_N}\,\epsilon_{i_1 i_2\ldots i_N}$ is precisely the determinant of M, and so we find that

$$\int d^N\eta\,\eta_1\,\eta_2\,\ldots\,\eta_N = \det[M]\int d^N\eta'\,\eta_1\,\eta_2\,\ldots\,\eta_N \tag{A.13}$$

This expression allows us to read off the change in the integration measure,

$$d^N\eta = \det[M]\,d^N\eta' \tag{A.14}$$

This relationship is responsible for the introduction of the fermion determinant in Eq. (2.51).